BRNO UNIVERSITY OF TECHNOLOGY
VYSOKÉ UČENÍ TECHNICKÉ V BRNĚ

FACULTY OF MECHANICAL ENGINEERING
FAKULTA STROJNÍHO INŽENÝRSTVÍ

INSTITUTE OF PHYSICAL ENGINEERING
ÚSTAV FYZIKÁLNÍHO INŽENÝRSTVÍ

MAGNETIC PROPERTIES OF SELF-ASSEMBLED FERH NANOMAGNETS
MAGNETICKÉ VLASTNOSTI SAMOUSPOŘÁDANÝCH NANOMAGNETŮ FERH

MASTER'S THESIS
DIPLOMOVÁ PRÁCE

AUTHOR
AUTOR PRÁCE
Bc. Lucie Motyčková

SUPERVISOR
VEDOUCÍ PRÁCE
M.Sc. Jon Ander Arregi Uribeetxebarria

BRNO 2020

BRNO UNIVERSITY OF TECHNOLOGY
FACULTY OF MECHANICAL ENGINEERING

Specification Master's Thesis

Department:	Institute of Physical Engineering
Student:	**Bc. Lucie Motyčková**
Study programme:	Applied Sciences in Engineering
Study field:	Physical Engineering and Nanotechnology
Supervisor:	**M.Sc. Jon Ander Arregi Uribeetxebarria**
Academic year:	2019/20

Pursuant to Act no. 111/1998 concerning universities and the BUT study and examination rules, you have been assigned the following topic by the institute director Master's Thesis:

Magnetic properties of self–assembled FeRh nanomagnets

Concise characteristic of the task:

Solid–state dewetting is a ubiquitous phenomenon in nature, in which a thin film of a substance (e.g. liquids, polymers, metals or semiconductors) undergoes a spontaneous agglomeration and assembles into 3D islands, as a result of capillary instabilities driven by surface tension and mass transport. Over the last few decades, this phenomenon has been exploited as a way to fabricate large–area arrays of nanostructures with interesting chemical, optical, magnetic or semiconductor functionalities. The diploma thesis will focus on utilizing this approach for the fabrication of epitaxial nanoisland arrays of FeRh, which features a first–order phase transition between antiferromagnetic and ferromagnetic states just above room temperature. The fabrication process for obtaining nanoisland with different sizes and shapes while conserving the phase transition will be optimized on different substrates. The magnetic properties and phase transition of the fabricated nanoislands can be studied and imaged using several microscopy platforms, such as magneto–optical Kerr effect microscopy, electron microscopy and magnetic force microscopy. Finally, an attempt will be made to etch the nanoislands away from the substrate and study their magnetic behavior in a liquid environment. This could have interesting implications, for instance, in the fields of energy harvesting or targeted therapy applications.

Goals Master's Thesis:

1. Fabrication of self–assembled FeRh nanoislands in different substrate systems via solid–state dewetting, using magnetron sputtering.
2. Magnetic characterization and imaging of the antiferromagnetic–to–ferromagnetic phase transition using different microscopy techniques.
3. Attempt to release the nanoislands from the substrates and study of the magnetic behavior of nanoparticles in a liquid environment.

Recommended bibliography:

THOMPSON, C. V. Solid-State Dewetting of Thin Films. Annual Review of Materials Research. 2012, 42(1)

LEROY, F., Ł. BOROWIK, F. CHEYNIS, Y. ALMADORI, S. CURIOTTO, M. TRAUTMANN, J.C. BARBÉ a P. MÜLLER. How to control solid state dewetting: A short review. Surface Science Reports. 2016, 71(2), 391-409.

UHLÍŘ, V., J. A. ARREGI a E. E. FULLERTON. Colossal magnetic phase transition asymmetry in mesoscale FeRh stripes. Nature Communications. 2016, 7(1).

LIU, M., P. BENZO, H. TANG, et al. Magnetism and morphology in faceted B2-ordered FeRh nanoparticles. EPL (Europhysics Letters). 2016, 116(2).

Deadline for submission Master's Thesis is given by the Schedule of the Academic year 2019/20

In Brno,

L. S.

prof. RNDr. Tomáš Šikola, CSc. Director of the Institute	doc. Ing. Jaroslav Katolický, Ph.D. FME dean

Abstract
Magnetic nanoparticles and nanostructured materials are of great promise in many domains, including biomedicine, environmental remediation, or energy harvesting. Therefore, there is an ever-growing interest in their unique nanoscale functionalities as well as in the development of viable fabrication routes. This thesis investigates a self-assembly route, specifically solid-state dewetting of thin films, to produce epitaxial nanoisland arrays of the FeRh alloy on different single-crystal substrates. It is shown that using this fabrication route, the metamagnetic phase transition is preserved in nanoscale confined geometries. The morphology and magnetic properties of the self-assembled FeRh nanomagnets are characterized by a combination of experimental techniques and modeling, finding that their equilibrium shapes and magnetic order are closely interconnected. Furthermore, a route for obtaining free-standing nanoparticles is devised, which could potentially allow using metamagnetic nano-objects in cell cultures and biomedicine in general. To do so, the supported FeRh nanomagnets are released from the substrate via chemical wet etching. The behavior of the nanoparticles and their response to temperature cycling and magnetic field is subsequently studied in a liquid environment. The metamagnetic properties of separated nanoparticles are characterized using vibrating sample magnetometry.

Keywords
self-assembly, solid-state dewetting, FeRh, metamagnetism, supercooling, nanoislands, nanoparticles, remote actuation

Abstrakt
Magnetické nanočástice a nanostrukturované materiály jsou velkým příslibem v mnoha oblastech, včetně biomedicíny, sanace životního prostředí nebo získávání energie. Proto neustále roste zájem o výzkum jejich jedinečných vlastností a vývoj uskutečnitelných výrobních postupů. Tato práce se zabývá metodou samouspořádávání, spočívající v povrchové precipitaci tenkých vrstev, za účelem výroby epitaxních polí nanoostrůvků ze slitiny FeRh na různých monokrystalických substrátech. Při tomto výrobním postupu zůstává zachována metamagnetická fázová přeměna nanoostrůvků. Morfologie a magnetické vlastnosti samouspořádaných nanomagnetů z FeRh jsou charakterizovány kombinací experimentálních technik a modelování, přičemž bylo zjištěno, že jejich rovnovážné tvary a magnetické uspořádání jsou navzájem propojeny. Kromě toho je navržena cesta pro získání volných nanočástic, která by mohla potenciálně umožnit využití metamagnetických nanostruktur v buněčných kulturách a biomedicíně obecně. Za tímto účelem jsou nanoostrůvky FeRh uvolňovány ze substrátu chemickým leptáním. Chování nanočástic a jejich reakce na teplotu a magnetické pole jsou studovány v kapalném prostředí. Metamagnetické vlastnosti separovaných nanočástic jsou charakterizovány pomocí vibrační magnetometrie.

Klíčová slova
samouspořádávání, povrchová precipitace, FeRh, metamagnetismus, přechlazení, nanoostrůvky, nanočástice, dálkové ovládání

MOTYČKOVÁ, Lucie. *Magnetic properties of self-assembled FeRh nanomagnets.* Brno, 2020. 90 p. Master's thesis. Brno University of Technology. Faculty of Mechanical Engineering. Supervisor M.Sc. Jon Ander Arregi Uribeetxebarria.

I declare that I have written my master's thesis on the theme of *Magnetic properties of self-assembled FeRh nanomagnets* independently, under the guidance of the supervisor M.Sc. Jon Ander Arregi Uribeetxebarria, and using the sources quoted in the list of literature at the end of the thesis.

Bc. Lucie Motyčková

Acknowledgements

I wish to express my sincere gratitude to my supervisor M.Sc. Jon Ander Arregi for his patient mentoring, tireless assistance and corrections, intriguing discussions, as well as for making all my worries and difficulties more bearable by incessantly introducing humor. I am grateful for his kind understanding which he showed when listening to my problems both in the lab and in life.

My deep appreciation goes to the whole group of *Nanomagnetism and spintronics* at CEITEC. Specifically, I would like to thank Dr. Vojtěch Uhlíř for always coming with new ideas, for his support and encouragement in my research efforts, as well as for valuable comments on this thesis. I gratefully acknowledge Dr. Michal Staňo for his assistance in measurements made mainly with the scanning electron microscope with energy dispersive x-ray spectroscopy. I would also like to recognize the help I received from M.Sc. Milad Takhsha Ghahfarokhi with the fabrication of lithographically patterned structures. I thank Ing. Michal Horký for his willingness to help when encountering any kind of problem in the lab.

I also address my acknowledgement to doc. Klára Částková for her valuable advice concerning chemical wet etching. I would like to recognize the assistance of Mgr. Tereza Sojková with dynamic light scattering measurements and the help of Ing. Jana Dorazilová with dopamine coating.

I would like to extend my appreciation to all my lab mates from the group of *Micro et Nano-Magnétisme* at Institut Néel in Grenoble for the best Erasmus internship one can wish for. I will be always grateful to them for teaching me to make fun when doing science, to prepare and to drink coffee on a regular basis as a great daily get-together, for many inspiring conversations, as well as for putting their trust in me. Namely, I would like to thank Dott. Erika Fontana for her encouragement despite a distance of many hundreds of kilometers.

I am grateful to M.Sc. Nikola Fischer for his effort in reading this manuscript, for believing in me, for supporting me in my dreams and for all the joyful as well as difficult moments in our lives that we could share.

I am deeply indebted to my parents thanks to whom I could study and on whom I could rely throughout my whole life. I am thankful to my brothers for distracting me when it was much needed. I owe special thanks to my grandfather for being unconditionally proud of me.

Bc. Lucie Motyčková

Financial support from the Thermo Fisher Scientific is gratefully acknowledged.

Part of the work was carried out with the support of CzechNanoLab Research Infrastructure (ID LM2018110, MEYS CR, 2020–2022), CEITEC Brno University of Technology.

Contents

Introduction

Research and engineering of matter on the ultra-small scale continues to bring enormous changes to our world. In particular, magnetic nanoparticles and nanostructured materials constitute a unique platform for numerous sophisticated applications ranging from magnetic memories to free-standing particles offering remote control via applied magnetic fields in the domains of biomedicine or environmental remediation. However, a common major challenge of nanotechnology still consists in the control of the fabrication process aiming for high-quality nanostructures with the desired size, morphology, composition and crystal structure of the material of interest.

In the present study, the fabrication and characterization of self-assembled metamagnetic FeRh nanomagnets is presented. This is a novel material platform with interesting functionalities, that would in principle allow remote control not only by magnetic fields but also via other external agents such as temperature, hydrostatic pressure or optical pulses. We demonstrate that large-area arrays of FeRh nanomagnets can be produced through a cost-effective bottom-up fabrication route termed as solid-state dewetting. Furthermore, the unique properties of the material, such as the first-order phase transition from antiferromagnetic to ferromagnetic order slightly above room temperature, are maintained in nanomagnets formed via this self-assembly route.

Initially, the thesis focuses on the growth of self-assembled FeRh islands, thoroughly examinating the parameters and aspects that control the final island morphology. Besides, the island shapes on different substrates are discussed in terms of their equilibrium predictions based on the argument of surface energy. Next, the metamagnetic behavior of FeRh nanoisland arrays as well as of individual nanoislands is characterized in detail, finding a clear correlation between morphological features and metamagnetism.

In addition, we explore the possibility of releasing the supported FeRh nanomagnets from the substrate via chemical etching in order to obtain free-standing particles with exceptional properties. For the purpose of enabling potential applications in biomedicine or environmental remediation, we subsequently attempt to separate the particles from the etching solution in order to examine if their metamagnetic behavior is preserved even after detachment from the substrate, or if in turn is modified.

Therefore, this thesis can be essentially divided into three parts:

(i) An overview of the relevant applications and fabrication techniques of nano-objects is offered (Chapter 1). Furthermore, the basic concepts of solid-state dewetting as well as thermodynamics of thin film nucleation and growth are reviewed. Besides, the motivation for fabrication of self-assembled FeRh nanomagnets is presented.

(ii) The morphology (Chapter 2) and magnetic properties (Chapter 3) of FeRh islands supported on different substrates are characterized using a combination of experimental techniques and thermodynamic theoretical arguments.

(iii) Self-assembled FeRh nanomagnets are released from substrates by chemical etching (Chapter 4) and separated from the etching solution (Chapter 5) in order to obtain free-standing FeRh nanoparticles. Finally, we briefly attempt to characterize their metamagnetic properties as well as to observe their behavior in a liquid environment (Chapter 6).

1 Nanoparticles and nanostructured materials

Nanoscience has revolutionized modern research and technology by manipulating matter on atomic, molecular and supramolecular scales and will continue to impact our lives with innovations in a wide range of applications. This chapter starts with an overview of the properties, applications and preparation methods of nano-objects. Next, the solid-state dewetting process of thin films, which constitutes the principal fabrication approach in this thesis, as well as the physics of nanocrystal shapes on surfaces are summarized. Finally, the metamagnetic phase transition in FeRh and the potential of FeRh nanoparticles as a system of interest are introduced.

1.1 General properties and fabrication of nano-objects

Nanostructured materials and nanoparticles (NPs) as ultrafine objects with characteristic sizes from the nanometer to the micrometer range constitute a novel tool to conquer challenges in numerous research and technological fields (see Figure 1.1), thus being construed as one of the most significant development frontiers in modern science. Due to their reduced dimensions and enhanced surface area to volume ratio, nanostructures as well as NPs possess unique features in terms of reactivity. In the same way, morphological, electronic, optical, thermal, mechanical and magnetic properties of these material platforms are often significantly modified when compared to the corresponding bulk counterpart [1].

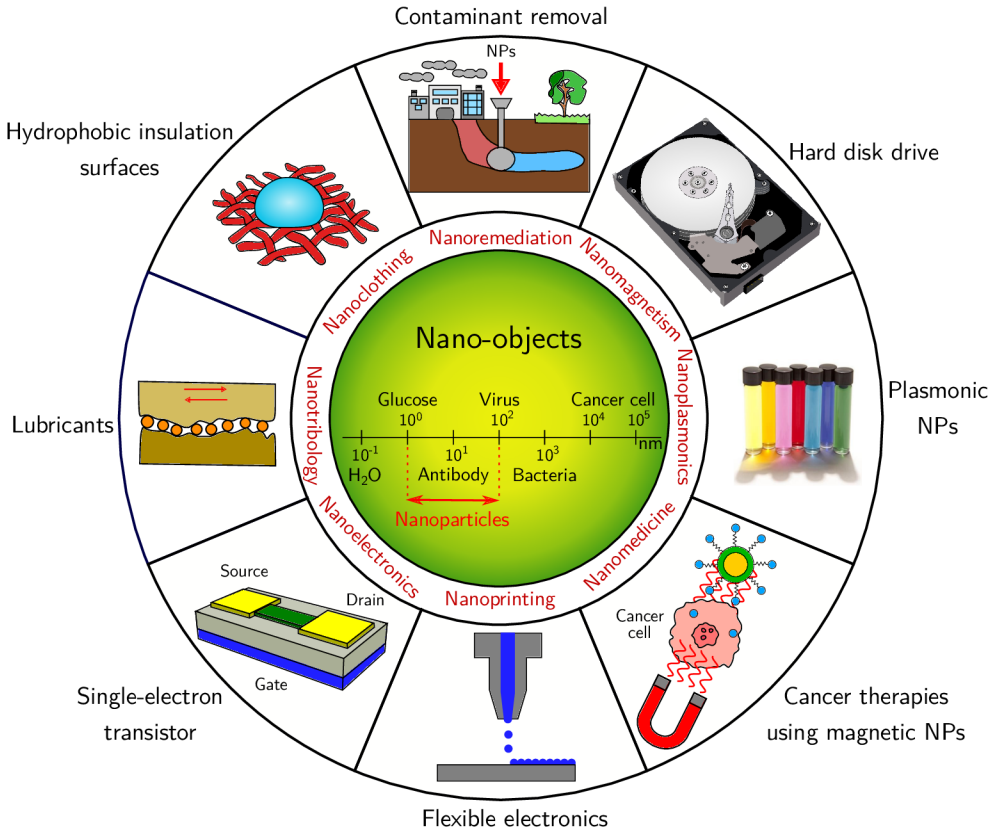

Figure 1.1: Applications of nanostructures and NPs.

The size itself of nano-objects often represents a key attribute for applications. For example, fine NPs can pass through certain biological barriers within the human body. In particular, passive targeted nanocarriers are designed to cross the tumor vascular barrier through gaps between adjacent endothelial cells (100–500 nm in size) and are retained in the tumor due to poor lymphatic drainage, a process termed as enhanced permeability and retention (EPR) [2]. In the field of electronics, the use of metallic nanostructures is promising for fabrication of smaller, single-electron transistors and consequently fit more transistors on a computer chip, resulting in higher processing speed and memory capacity [3]. Furthermore, the large specific area of NPs improves chemical reactivity as more material is exposed to interact with the surroundings. Consequently, NPs are widely used as catalysts, including in the automotive industry where nanoengineered systems clean the exhaust particles, thus helping to reduce the toxicity of engine fumes [4]. Besides, the enhanced surface area makes NPs suitable candidates for functionalization (adding components for specific purposes) for applications ranging from drug delivery to clothing insulation. In the environmental context, the minute size of the NPs allows easy transport under pressure to contaminated zones, while the increased surface area and thus high reactivity is advantageous for the removal of many hazardous compounds such as non-aqueous phase liquids and heavy metals [5].

The **electronic and optical properties** are coupled in nano-objects as well [6]. Metallic NPs with sizes smaller than the incident wavelength absorb light at very specific regions of the visible spectrum due to interactions between the incident light and surface electrons in the conduction band [7]. This interaction produces collective oscillations of electrons, a phenomenon known as localized surface plasma resonance (LSPR), with a maximum light absorption frequency depending on the size, geometry, composition, dielectric environment and interparticle spacing of NPs. The unique plasmon absorbance features of the noble metal NPs hold promising prospects for a wide variety of applications including chemical sensors and biosensors [8]. The LSPR also induces a strong local electromagnetic field near the surface of NPs which can favorably enhance processes such as Raman scattering, fluorescence or solar energy conversion [9]. Another subset of nanostructures with exceptional electronic and optical properties are quantum dots (QDs), semiconductor nanocrystals confining the motion of electrons and holes in all three spatial directions [10]. Due to the ultrafine dimensions of QDs, addition or subtraction of a single electron can significantly affect the intrinsic bandgap of the material. As more energy states are lost due to quantum confinement, the energy bandgap increases, which provides tuning of the optical absorption and emission of QDs. The unique properties of QDs make them suitable candidates for fluorescent labeling for *in vitro* and *in vivo* imaging. Other prominent applications include their utilization as single-electron transistors, efficient light-emitting devices (LED) and building blocks for quantum computing [11].

As for **thermal properties**, applications make use of high conductivity of metals by suspending solid NPs into fluids in order to enhance the thermal conductivity of conventional heat transfer fluids [12]. Here, NPs are more favorably used than microparticles due to the high specific surface area, allowing increased heat transfer as well as high dispersion stability with predominant Brownian motion of particles [13]. Moreover, the melting point of a particle scales with its dimensions [14]. NPs contain a large number of surface atoms which are removed more easily than bulk atoms, therefore the total energy required to overcome intermolecular forces is lowered leading to NP melting temperature decrease. The most successful applications include nanojoining for electronic assemblies, inkjet-printing for flexible electronics or sintering of ceramic materials [15].

Concerning the **mechanical properties**, special parameters in terms of hardness, elastic modulus, adhesion or friction can be achieved [16]. Specifically, as for lubricated systems with NPs as additives, where the main focus is to overcome problems such as friction and wear, the advantageous mechanical attributes of NPs differ for various materials and accordingly also their effect on the tribological properties [17]. Besides, abrasive NPs can be employed in nanomanufacturing to physically crush and chemically remove microscopic structural features on a sample in order to obtain a flat surface. Furthermore, various NPs can be included within a metal or polymer matrix to produce reinforced composite coatings. By tuning the NP and matrix attributes, properties such as hardness, self-lubrication, wear-resistance and energy-absorbing can be tuned as desired.

In the context of **magnetic properties**, nanostructures and NPs display a very rich variety of emergent phenomena and can be notably controlled via externally applied magnetic fields. An extraordinary feature of small enough magnetic NPs (MNPs) is their superparamagnetic (SPM) response. This occurs when energy minimization results in the formation of single-domains and the magnetic anisotropy energy is reduced as a result of the small volume of the particle, making it comparable to the thermal activation energy $k_{\mathrm{B}}T$ [18]. In such a case, the resultant magnetic moment of single particles preferably oriented along a particular easy axis direction can be spontaneously reversed by thermal agitation which results into a magnetization behavior similar to paramagnetic materials. SPM-NPs are thus remarkable due to their negligible agglomeration tendency which makes them suitable for many diverse applications in nanomedicine. These include magnetic carriers for targeted drug delivery, enhancement agents for magnetic resonance imaging (MRI) or heat generators for a specific cancer treatment termed as magnetic hyperthermia [19]. In addition, applications of SPM-NPs have recently expanded also into the field of environmental science, serving as adsorbents or catalysts in removing contaminants from groundwater, soil and air [20]. Besides medical and remediation applications, MNPs and nanoscale granular magnetic materials are of great interest in information technology with its ever growing requirements for higher storage densities and low-power operation [21]. However, as data storage at ambient temperature over a time scale of typically a decade is not at all compatible with superparamagnetism, current technology uses sophisticated approaches and systems engaging materials with high magnetocrystalline anisotropy [22, 23], thus mitigating the negative effects of thermally induced magnetization fluctuations in the stability of the recorded information.

Nano-object fabrication methods can principally pursue two main different strategies: the so called top-down or bottom-up approaches (see Figure 1.2) [24]. Top-down techniques are subtractive processes in which parts of a material are removed to create controlled shapes and sizes. These are based on cleaving a large piece of a bulk material using an externally delivered significant amount of mechanical, thermal or chemical energy to transform the material into nanoscale elements. In contrast, bottom-up synthesis methods are additive processes, consisting in the self-assembly of fine components of atomic or molecular dimensions to larger complex architectures through supramolecular interactions or external electrical, chemical, thermal or photon stimuli.

Top-down methods are often used to fabricate a large volume of very precise nanostructures, thus representing a suitable route for mass manufacturing in today's industry [24, 25]. The most advanced approaches involve various lithographic and etching techniques providing, in addition to the material removal, nanostructure patterning with the goal to obtain specific shapes and sizes (see Figure 1.3a). In a first stage of the

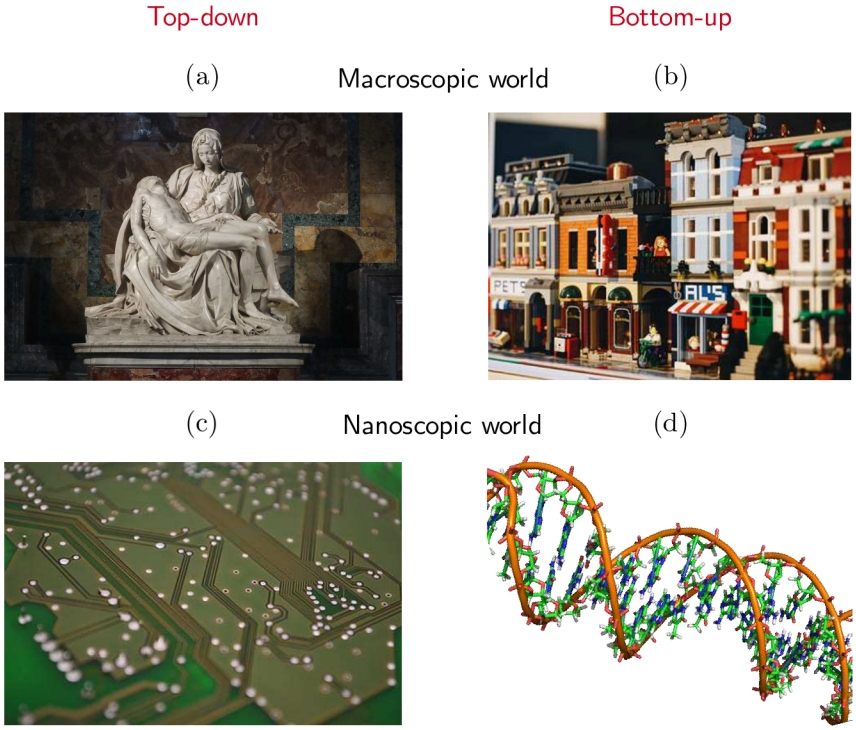

Figure 1.2: Examples of top-down and bottom-up fabrication approaches: (a) Michelangelo's Pietà carved from a single slab of marble (top-down fabrication at the macroscale); (b) town built from LEGO bricks (bottom-up construction at the macroscale); (c) nanocircuits made into a single computer chip (top-down fabrication at the nanoscale); (d) DNA double helix composed of nucleotides joined together by covalent bonds (bottom-up synthesis at the nanoscale). All images are from public domain.

lithographic process, a mask is usually patterned on top of a thin film or a substrate. The processes employed at this stage include photolithography (reaching state-of-the-art dimensions just below 100 nm using current short-wavelength optical sources), electron beam lithography (EBL, providing patterns feature sizes below 10 nm by sweeping a finely focused electron beam across the surface), or nanoimprint lithography (NIL, based on mechanical printing via master stamp with a resolution below 10 nm). In a second stage, a thin film is deposited on top of the patterned mask. Alternatively, etching techniques can also remove the film portions that are left exposed by the mask. This etching routes include, for example, reactive ion etching (RIE, combining both physical and chemical etching processes by employing electrically charged etchant molecules accelerated toward the substrate) and deep reactive ion etching (DRIE, an extension of RIE enabling higher rates and larger etch depths) [26, 27]. Less precise methods consist in material fracturing by mechanical energy, harsh chemicals or high amount of heat (see Figure 1.3b). Top-down methods offer possible mass production due to the significant advances in automated lithographic processes and very precise light/electron beam focus and positioning. Other advantages include the good reproducibility and precision in the location. However, they often suffer from a worse controllability in terms of uniform shapes and sizes at the nanoscale if compared to bottom-up techniques, given the high energy or chemical input involved in the processing. A fundamental constraint of top-down approaches is their resolution limit, as this is directly dependent on the existing cutting tool technology.

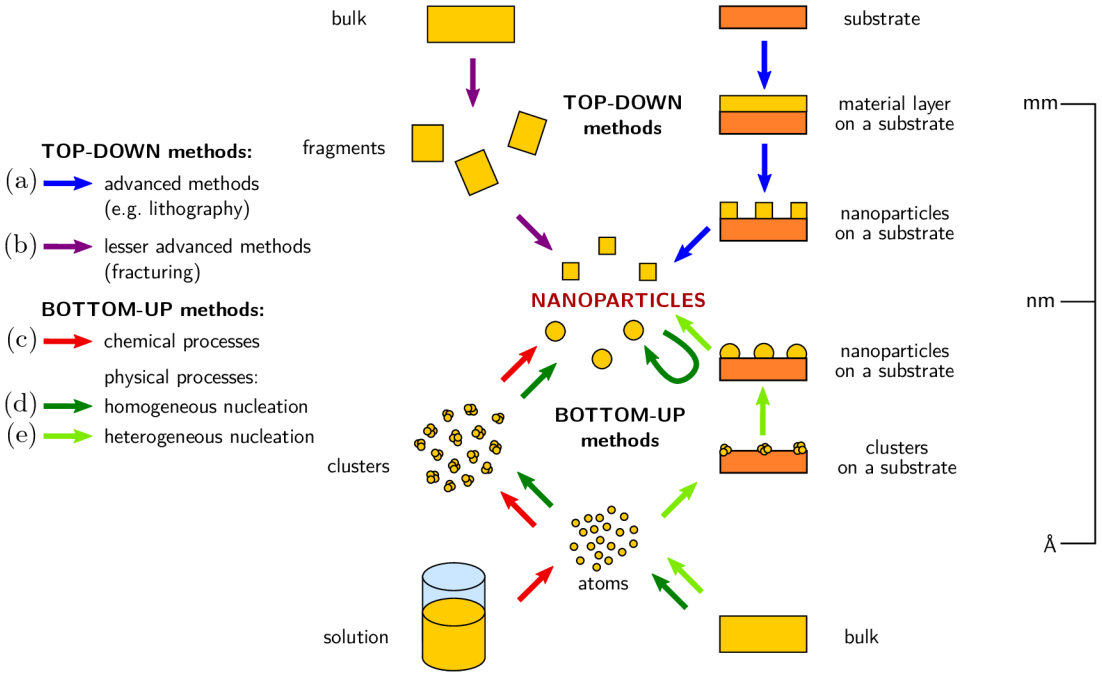

Figure 1.3: Top-down and bottom-up fabrication methods of NPs: (a) advanced techniques starting from a layer deposition followed by patterning and possible detachment; (b) less precise approaches based on material fracturing; (c) chemical processes taking place in a solution; (d) physical homogeneous nucleation in a chamber, subsequent collection on a substrate and possible reverse detachment; (e) physical heterogeneous nucleation on a substrate and possible detachment.

Bottom-up methods generally consist of nano-object synthesis through the nucleation and subsequent assembly of nanoscale building blocks (e.g. atoms, molecules). This process provides high-quality control over the particle size at the nanometer scale [28]. The resolution limit can be as low as at the atomic level and the process is not being limited in its up-scaling, as very large number of entities can jointly participate in the synthesis. Besides, self-assembly offers a simple, fast, and low-cost approach as well as the ultimate limit of miniaturization compared to lithographic techniques [24]. However, the mastery of self-assembly is currently limited to fairly simple nanostructured materials, not being able, for instance, to create integrated devices. The bottom-up fabrication route can be roughly divided into chemical and physical processes. The chemical approach involves preparation of NPs from a solution under controlled temperature and pressure (see Figure 1.3c), including strategies such as colloidal methods (profiting from solution of different ions producing insoluble precipitates), microemulsion (based on formation of droplets resulting from stirring of two immiscible liquids), hydrothermal synthesis (engaging appropriate chemical precursors dissolved in water under high temperatures and pressures) or electrodeposition (employing conducting substrates) [29]. Conversely, physical processes comprise reactions involving solidification from a liquid or gas phase with the purpose of obtaining nanostructures or NPs. While the atomization method based on cooling of a molten metal into droplets generally results in the formation of micron or slightly sub-micron particles, the gas condensation approach can be tuned to produce particles of various sizes in the nanoscale range. Here, initial materials undergo vaporization via thermal evaporation sources usually under an inert gas atmosphere leading to the formation of metallic clusters by homogeneous nucleation in the gas phase and subsequent

NP growth under a thermal plasma process. The NPs synthesized during this process are easily collected using a filter or deposited on a substrate (see Figure 1.3d). Besides, the material vapor can be directly deposited on a substrate in order to induce heterogeneous nucleation followed by film growth (see Figure 1.3e).

In addition to the top-down and bottom-up fabrication methods listed above, novel approaches favorably combine both routes using top-down control to guide bottom-up processes [30]. A major benefit consists in the possibility of using top-down patterning to readily address the complementary length scales to those that are well controlled by bottom-up assembly.

1.2 Solid-state dewetting of thin films

A promising bottom-up approach aiming to nanostructure fabrication is based on the solid-state dewetting of thin films. In this phenomenon, a metastable thin film in the as-deposited state spontaneously agglomerates into three-dimensional (3D) islands to reach a closer to equilibrium configuration [31]. In order to promote thermodynamically driven processes leading to a stable state of the deposited material, energy in the form of heat must be supplied to the system. As temperatures well below the melting point of the film are usually sufficient to induce mass transport, dewetting occurs while the film remains in the solid state. However, in contrast to dewetting of liquid layers on solid substrates (i.e. the agglomeration of a liquid film into 3D liquid droplets), the dewetting of solid films on solid substrates has not yet reached the same level of understanding since the first observations of Au island formation on fused silica by Jiran and Thompson in 1990 [32]. The dewetting effect is often considered as a drawback that complicates the fabrication of integrated circuits and other microelectronic devices based on thin films and limits the reliability of microsystems operated under high temperatures. Conversely, solid-state dewetting also presents an innovative low-cost route for controlled mass production of island arrays commonly used in areas such as catalysis, electronics, and plasmonics [33]. In addition, the subsequent detachment from the substrate could provide the possibility to obtain free-standing NPs for various applications.

The phenomenon of solid-state dewetting only occurs for structures in non-equilibrium configuration [31]. This is usually the case of vapor deposition techniques which often limit the mobility of deposited atoms through kinetically driven growth of metastable continuous layers. The thermodynamic equilibrium state of the deposit on the substrate may be approached by heating the system to higher temperatures, therefore providing energy to enhance the mobility of constituent atoms leading to more energetically favorable shapes. The dewetting process thus constitutes a bottom-up nanoisland fabrication route through vapor deposition which is an alternative to the bottom-up island nucleation achieved by thermodynamic growth via vapor deposition techniques at higher temperatures.

Solid-state dewetting is driven by the minimization of surface free energy, when the interfacial area between the film and its substrate is reduced by agglomeration of the film into 3D islands. The condition for dewetting can be written as

$$\gamma_F + \gamma_{FS} - \gamma_S > 0, \tag{1.1}$$

where γ_F and γ_S are the surface energies of the film and substrate materials, respectively, and γ_{FS} is the film/substrate interfacial energy [34]. The mass transport process of solid-

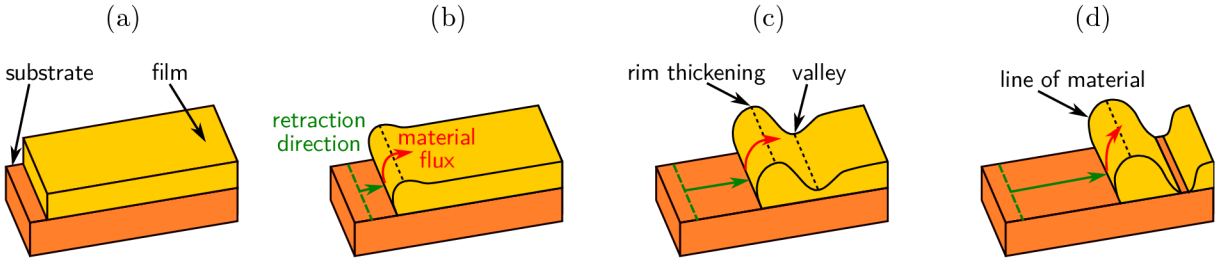

Figure 1.4: Edge retraction: (a) initially deposited film; (b) the rim formation and the first edge receding; (c) rim thickening and the valley formation and deepening; (d) line formed from the now-isolated rim.

state dewetting proceeds via capillary-driven surface diffusion. For isotropic materials, this can be expressed by an atomic flux

$$\mathbf{J} = -B\nabla_{\mathrm{s}}\kappa \quad \text{with} \quad B = \frac{D_{\mathrm{s}}\gamma_{\mathrm{F}}\Omega^2 n}{k_{\mathrm{B}}T}, \tag{1.2}$$

where $\nabla_{\mathrm{s}}\kappa$ is the surface gradient of the film curvature κ, D_{s} is the surface diffusion constant, n is the number of diffusing adatoms per unit area, Ω is the atomic volume, k_{B} is the Boltzman constant and T is the absolute temperature [34]. In case of Si on SiO_2, the kinetic coefficient is $B \approx 1 \cdot 10^{-5}\,\mu\mathrm{m}^4\mathrm{s}^{-1}$.

Dewetting can start at film edges through mechanisms such as edge retraction and fingering instabilities [31]. Alternatively, it can also result from spontaneous heterogeneous nucleation of voids, occurring at randomly distributed defects such as vacancies and contaminants. Regarding polycrystalline films, holes are usually initiated at grain boundaries, especially at grain boundary triple junctions, in order to minimize the interfacial energy associated with the grain boundaries and surfaces.

Edge retraction rises as the film tends to reduce its curvature at the edge (see Figure 1.4a) and thus minimize surface energy [31]. However, since the curvature at the edge of the layer will be always higher compared to the flat surface of the film in the surroundings, material will continue to flow from the triple line (where the film, ambient and substrate are in contact) into the flat area of the film. Consequently, simultaneously with the edge retraction, material accumulates along the edge resulting in the development of an elevated rim (see Figure 1.4b). Further edge retraction causes rim thickening accompanied by the formation and deepening of a valley behind the rim (see Figure 1.4c). When the bottom of the valley contacts the underlying substrate, a line of material is left at the surface as the last step of the process termed as edge pinch-off (see Figure 1.4d). Then, the new edge continues to retract. Dewetting by edge retraction occurs only for stable fronts [34]. As for anisotropic materials, a stable front is formed by atomically flat crystallographic facets with a common zone axis in the direction of the triple line. Obviously, the standard concept based on curvature-driven surface diffusion cannot be directly applied and more sophisticated models would have to be used to describe the edge retraction for faceted materials [35].

On the contrary, for the case of unstable front, soon after the material has started to accumulate along the receding edge (see Figure 1.5a), a perturbation develops in the rim (see Figure 1.5b) [31]. At this place, the film becomes thinner and therefore the edge retraction rate locally increases (see Figure 1.5c). Consequently, the front proceeds with the formation of elongated structures termed as fingers (see Figure 1.5d). Generally, instabilities occur on a large scale resulting in a periodic structure which develops into an array

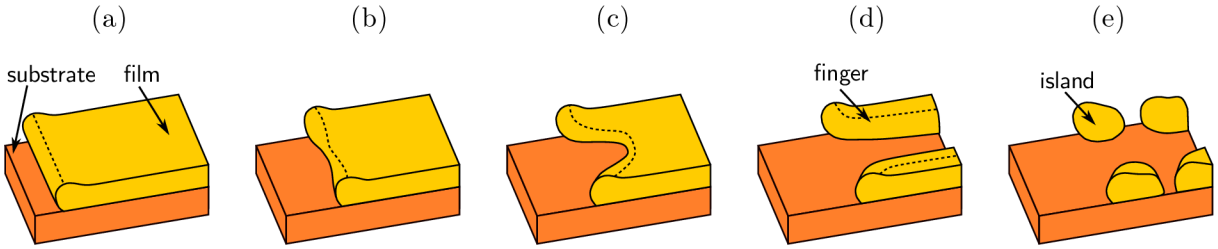

Figure 1.5: Fingering instabilities: (a) rim formation; (b) perturbation development; (c) locally increased edge retraction; (d) finger formation; (e) subsequent island formation due to a Rayleigh-Plateau instability.

of fingers. Eventually, the fingers can break down into 3D nanoislands through a beading mechanism similar to a Rayleigh-Plateau transition (see Figure 1.5e) [34]. Concerning faceted materials, unstable fronts undergoing fingering instabilities have a common zone axis oriented differently than the front direction.

Far from film edges, the most frequent mechanism of dewetting generally consists in the heterogeneous nucleation of voids [35]. Due to crystalline anisotropy, circular holes rarely emerge and thus the disruption of the film is initiated in the form of crystallographically oriented voids instead, usually at grain boundaries and principally at grain boundary junctions. Once the voids above a critical size with stably oriented sides nucleate heterogeneously in the film and expose the substrate (see the square void nucleation revealing the orange substrate in Figure 1.6a), they continue spontaneously growing by relocating the film material to the surrounding rim (see the sketched green circles around voids in Figure 1.6a–b, not shown in Figure 1.6c–d for the purpose of clarity). The rim around the opening voids does not thicken uniformly but the material accumulates mainly around the center of the edges, thus creating sharp corners which can recede faster (see Figure 1.6b). Subsequently, the void edges undergo a shape instability leading to the finger formation (see Figure 1.6c–d). Here, the void corners act as finger precursors resulting in a destabilization of the stable edges. Alternatively, the straight fingers can break apart into 3D nanoislands.

Furthermore, for strongly anisotropic films, the void sides are rather unstable and dendritic structures are formed [35]. The dewetting process initiates by the quick development of long branches which are later ramified by the nucleation of secondary branches perpendicular to the principal ones. According to the dendrite branch density, one obtains a pattern with long nanowires or nanoislands. Finally, ultrathin films can be sensitive to local fluctuations which completely penetrate the film and dewet in a fractal geometry.

In order to control and tune the morphology of the final dewetted state, as well as to avoid dewetting when it turns detrimental for the fabrication of microelectronic devices based on thin films, it is necessary to obtain a good understanding of the influence of various parameters on dewetting.

(i) For instance, numerous research studies have shown a significant impact of the original **film thickness** on the island dimensions and distribution. Specifically, it is observed that the island size varies linearly with the film thickness, whereas the island density is inversely proportional to the second power of the thickness [34]. Besides, the driving force for dewetting and thus the dewetting velocity decreases with the thickness, resulting in a temperature reduction at which dewetting occurs for thinner films [31].

(ii) The **processing temperature** itself is another crucial parameter influencing the final state. As a temperature increment induces more local defects, the dewetting

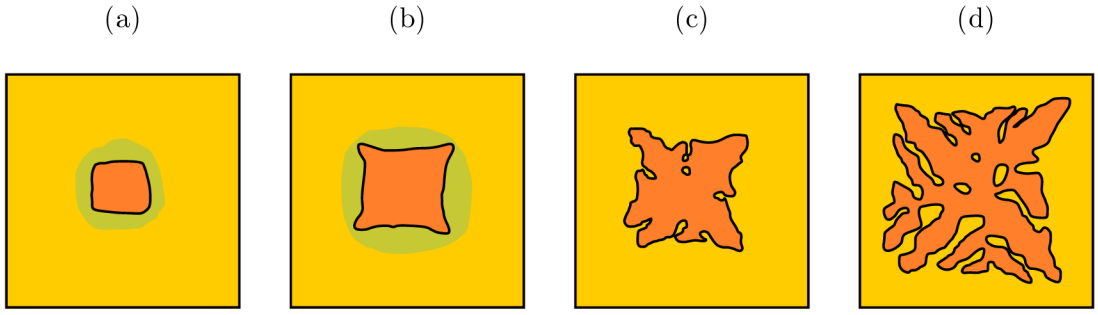

Figure 1.6: Void opening (yellow - film, orange - substrate, green - accumulated rim): (a) the heterogeneous nucleation of a crystallographically oriented void; (b) rim thickening at the center of the edges and the development of sharp corners; (c) shape instabilities leading to (d) the formation of fingers breaking down into 3D islands.

rate increases and therefore islands of higher density and smaller sizes emerge [34]. However, higher temperatures also bring negative effects on the regularity of island ordering.

(iii) Another way to impact dewetting is to vary the **strain state** in the film. After the hole formation, the strain in the film around the hole can partially relax which makes hole formation more likely [31]. The islands formed by dewetting of strained films are thus smaller and their density is higher [34]. Furthermore, one can observe elongation due to an anisotropic strain relaxation in one direction. On the contrary, films subjected to compressive strain can exhibit grain thinning. This phenomenon consists in the hillock formation upon heating as a way to relax the strain. However, during subsequent cooling the tensile strain develops instead and stress relief in this case causes grain thinning and hole formation. When heated again, these holes can contribute to dewetting.

(iv) The dimensions and the surface density of dewetted agglomerates can be also controlled by **contamination of a foreign deposit** such as carbon, by using ionic bombardment to create structural defects before annealing or by alternatively pre-patterning the substrates to induce large-scale topographic control [34].

(v) For anisotropic materials, an important parameter includes the **crystallographic orientation** of the dewetting front and the crystallographic orientation of the elongated fingers which may be formed.

Technological interest of self-assembled nanostructures

For a long time, solid-state dewetting has presented a crucial problem in microelectronics processing by limiting further size reduction of electronic devices and thus much effort has been performed to find ways of avoiding it. In parallel, several research studies have started to purposely induce dewetting in order to produce large-area nanostructure arrays remaining beyond the reach of conventional lithographic techniques, usually restricted to the development of nanoscale patterns on Si wafers. Accordingly, solid-state dewetting has been studied on various systems of films and substrates and proposed for diverse technological applications.

Among the first, metallic films have been the subject of both theoretical and experimental studies. Metallic films dewetted into beads have been already beneficially used as catalysts for the growth of semiconductor nanowires and carbon nanotubes, which is of

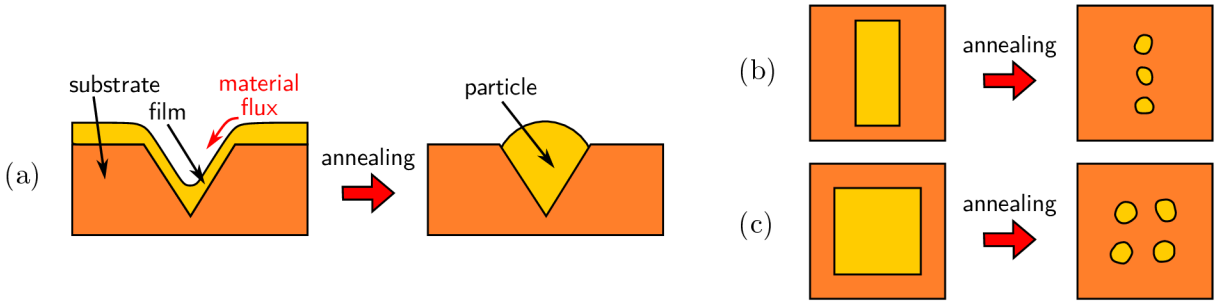

Figure 1.7: Topography-mediated dewetting: (a) film deposited onto pit-like topographic features made into the Si substrate resulting in particles of near-uniform size; (b) top view of patterned lines or (c) rectangles leading to arrays of particles.

interest for applications like electrical interconnects or biosensors [36, 37]. Dewetting of a thin film on a flat surface generally results into islands with weakly controlled distribution of sizes and spacing, making them inappropriate for advanced devices in microelectronics and photonics. In this sense, Thompson's research group at Massachusetts Institute of Technology (MIT) [38] has introduced the use of Si substrates with periodic regular pit-like topographic features made via lithographic techniques as a way to produce well-ordered arrays of near mono-disperse gold particles (see Figure 1.7a). A similar concept based on periodic gratings with inverted pyramid patterns has been implemented using nanoimprint lithography on a solgel silica layer. The posterior dewetting of a Ag film on top of this pre-patterned surface leads to NP arrays that could act as a novel platform for advanced optical devices in plasmonics [39]. This topography-mediated dewetting is not the only route to obtain self-assembled metal particles of nearly uniform size in a patterned array. An alternative approach consists in patterning Au films through a lift-off process into narrow lines or rectangles (see Figure 1.7b–c) which subsequently dewet to form arrays of particles at smaller length scales than the original pattern [36]. Follow-up research has shown even more complex dewetted structures produced in a controlled and designed way. For instance, one can take advantage of the strong influence of the initial sizes and in-plane crystallographic alignments of the patches patterned from epitaxial Ni films on MgO substrates on the final shapes of the dewetted pattern [40].

There is also a large interest to translate these concepts to semiconductor films for the fabrication of electronic devices. Solid-state dewetting of crystalline Si films on insulator (SOI) underlayers has also been thoroughly investigated from the theoretical and experimental point of view. In analogy with metallic films, good control over dewetting of pre-patterned SOI patches has been achieved despite the much smaller typical thickness of the initial layers and the use of amorphous (SiO_2) instead of crystalline (MgO) substrates. The amorphous character of the surface naturally introduces intrinsic disorder and consequently brings uncontrolled dewetting behaviors over large scales [41, 42].

Nevertheless, solid-state dewetting of thin Si films represents a viable method for the fabrication of quantum dots or optical meta-surfaces with Si or SiGe particles working as dielectric Mie resonant antennas to manipulate light-matter interactions, thus providing alternatives to plasmonic NPs [43]. Besides, the possibility of tuning the size as well as the shape of the islands and wire-like connected structures offers to implement such dewetted structures into semiconducting circuits for solid-state memories. Other recent advances consist of utilizing dewetted Si-based patterns as nanoimprint lithography masters for transferring the obtained complex nanoarchitectures to compounds of interest that do not usually undergo dewetting (such as metal oxide xerogels) [42]. Another class of

thin layers exhibiting self-assembly during annealing includes optical glasses [37]. The increasing versatility of nano-object fabrication via solid-state dewetting is promising for applications in electrically isolated nanocircuits, microfluidic devices, biomedical sensing, photonic circuits, energy harvesting or stretchable optics.

A different direction of development is directed towards solid-state dewetting and self-assembly of alloy materials. While the majority of studies deal with dewetting of elemental materials, dewetting of bi- or multicomponent thin films constitute recently a phenomenon of a great interest as actual thin film devices are usually composed of a combination of different materials in order to provide superior properties as compared to their elemental constituents [44, 45]. Bicomponent systems have been studied mainly by introducing bi- or multilayer thin films exposed to heat treatment to induce dewetting or alternatively to intermix the layers. Compositional influence on final morphology and properties have been examined by changing the thickness ratio of bi- or multilayers. Concerning miscible systems characterized by complete solid solubility, the dewetting characteristics have appeared to be independent of the stacking sequences. Furthermore, miscible alloys such as CoPd have shown to undergo similar stages of dewetting as elemental materials with the surface diffusivity lying in between the diffusivities of the constituents [45]. As for weakly miscible or immiscible systems, the thickness of individual layers (similarly to miscible alloys) as well as the stacking order act as intrinsic parameters responsible for different film morphologies observed after annealing. For example, two layers of immiscible systems such as CoAu are assumed to dewet separately [45]. If the underlayer (in this case Au) dewets earlier, the topography will behave as an additional driving force for the top film (Co) to dewet. Therefore, CoAu systems with Au underlayers exhibit faster dewetting than that with Co underlayer. A similar conclusion was reached when investigating NiAu films on SiO_2 [44].

In summary, solid-state dewetting represents a promising platform for a vast number of applications and has thus been the subject of many material studies engaging broad range of films including metals, semiconductors and glasses. Many works focus on topography-mediated dewetting, termed as templated dewetting, others investigate dewetting of multicomponent systems by depositing multilayers. However, dewetting of bicomponent metallic films obtained through deposition from a target of a specific binary alloy has been rarely reported. It is also worth noting that self-assembly of magnetic materials on surfaces has been investigated in detail [46, 47], but only few examples in literature focus on solid-state dewetting [33].

1.3 Equilibrium shapes of crystals on surfaces

Under thermodynamically driven growth, energy in the form of heat is sufficient to promote equilibrium configuration of the deposit already during deposition. Similar to the case of a water droplet on a solid surface, which adopts the form of a truncated sphere in order to minimize the surface tension in the system, the growth of solid compounds can be expressed in the first approximation by Young's equation

$$\gamma_{SG} = \gamma_{NS} + \gamma_{NG} \cos\theta, \tag{1.3}$$

where θ is the contact angle and γ_{SG}, γ_{NS} and γ_{NG} are the surface energies of the substrate/gas, nucleus/substrate and nucleus/gas interfaces, respectively (see Figure 1.8) [48].

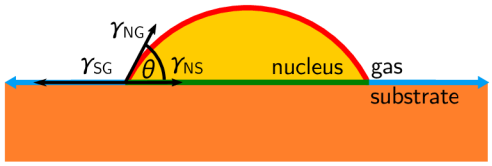

Figure 1.8: Water droplet model for a nucleus of a deposited material on a substrate.

The degree of wetting depends on the specific values of surface energies during growth and is characterized by the contact angle θ. Accordingly, one can distinguish three principal growth modes.

(i) The layer-by-layer, or Frank–van der Merwe, growth mode during which the deposited material grows in the form of continuous layers.

(ii) The island, or Volmer–Weber, growth mode which corresponds to the situation when the deposit forms clusters of atoms.

(iii) The layer-plus-island, or Stranski–Krastanov, growth mode represents the case when the deposit forms one or more layers in the early stages of growth and follows by subsequent island-like growth as the consequence of the altered balance of surface tensions.

Wulff and Winterbottom constructions

The Wulff and Winterbottom constructions are methods to determine the equilibrium shape of nanostructures with spatially anisotropic surface energy profiles, given that the too simplistic water droplet model cannot explain the formation of crystal facets [31]. Both constructions are based on the Wulff plot, which represents the orientation dependence of the surface energy. In this polar plot, each lattice plane is identified by a normal vector (h,k,l) and possesses an associated surface energy $\gamma_{(h,k,l)}$ where h, k, l are Miller indices forming a notation system (see the Wulff plot in two dimensions in Figure 1.9a). In order to minimize the total free surface energy, crystal facets are formed at the crystallographic orientations of local minimum surface energy. Therefore, in order to find the equilibrium shape from the Wulff plot, one must draw a tangent to each cusp and find the inner envelope of such tangents (see Figure 1.9b).

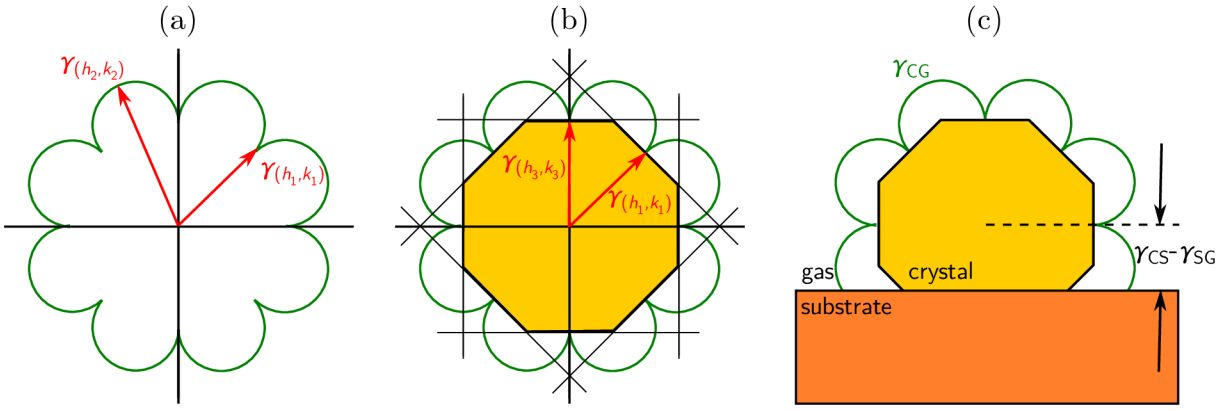

Figure 1.9: (a) The Wulff plot showing the magnitude of the surface energy of a crystal plotted for all possible directions of the surface normal in two dimensions (2D); (b) the equilibrium shape of a crystal identified from the Wulff plot; (c) the equilibrium shape of a crystal on a substrate identified by Winterbottom construction.

While such Wulff construction determines the equilibrium shape of a nanocrystal itself, the Winterbottom construction provides the equilibrium shape of a nanostructure supported on a substrate. Additionally to the angular dependence of the crystal/gas interfacial energy γ_{CG}, one must provide the difference between the surface energies γ_{CS} and γ_{SG} of the crystal/substrate and substrate/gas interfaces, respectively, which influences the height at which the crystallite is cut (see Figure 1.9c).

In order to predict the Winterbottom construction of a given nanocrystal, we use a *Python* package called *WulffPack* (run in *Python 3.6.9*) [49, 50]. For the purpose of obtaining the equilibrium shape of a nanostructure, a number of input parameters such as the crystallographic structure, the value of the lattice parameter, as well as the values of surface energy for particular facets and the interface with the substrate are defined.

1.4 Towards metamagnetic nanoparticles of FeRh

In this work, we aim towards obtaining NPs with a metamagnetic functionality via solid-state dewetting, which could represent a new class of promising NPs. The exceptional behavior of metamagnetic systems consists in their phase transition from the antiferromagnetic (AF) ground state, associated with zero net magnetization, to the ferromagnetic (FM) state, possessing a certain value of magnetization. Specifically, the chemically ordered (CsCl-type) iron-rhodium (FeRh) alloy close to equiatomic composition undergoes a first-order AF-to-FM transition upon heating slightly above room temperature ($\sim 370\,\mathrm{K}$) [51]. The AF-to-FM transition is easily controllable via various external agents such as temperature, magnetic fields, hydrostatic pressure, electric current, strain or optical pulses.

The typical magnetization vs temperature curve of an FeRh film is shown in Figure 1.10) [51–53]. In the low temperature phase, the Fe sublattice exhibits antiparallel alignment of adjacent magnetic moments with $\pm 3.3\,\mu_B$ per atom, while Rh atoms possess a zero magnetic moment. In the high temperature phase, the magnetic moments of Fe and Rh atoms are FM coupled, amounting to $3.2\,\mu_B$ and $0.9\,\mu_B$ per atom, respectively (see

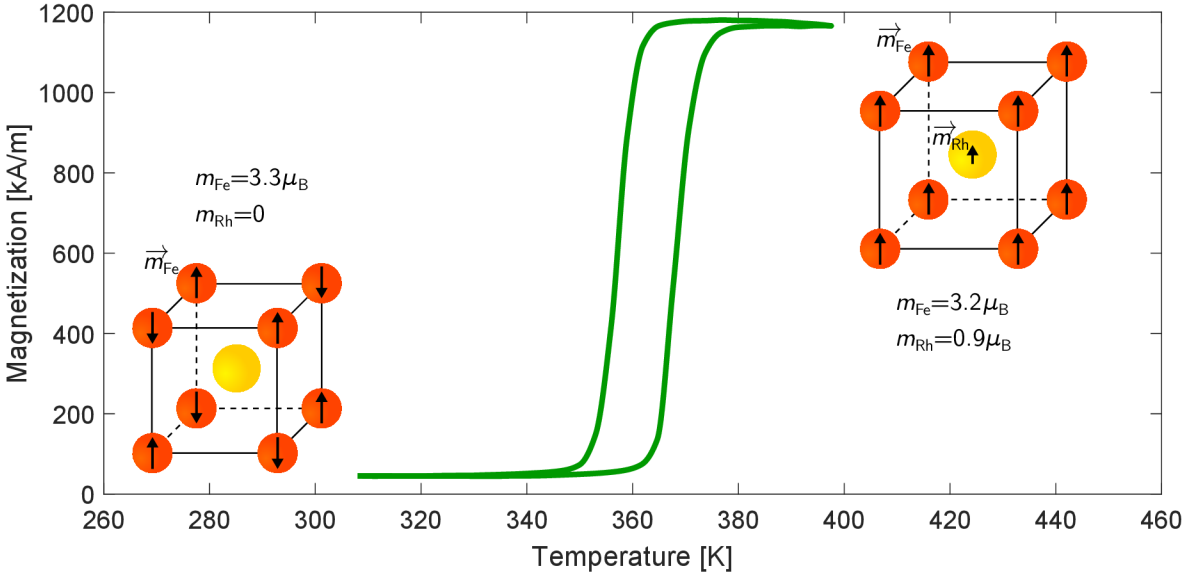

Figure 1.10: Magnetization vs temperature curve of a 120-nm-thick FeRh film grown onto a MgO(001) substrate with the low temperature AF structure of FeRh and the high temperature FM structure of FeRh.

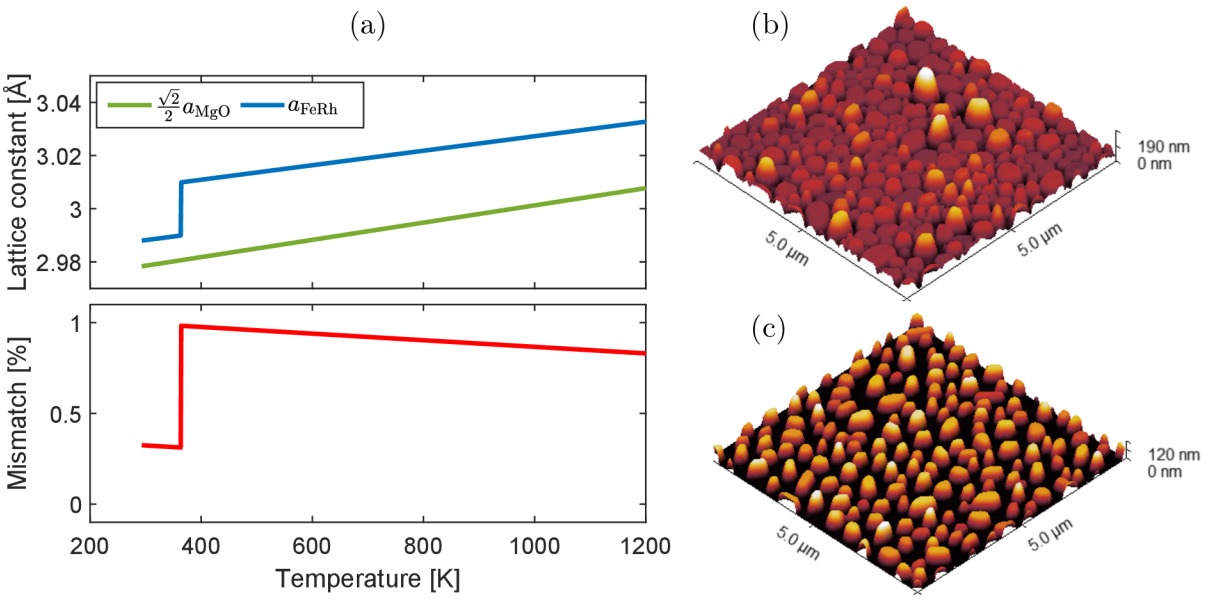

Figure 1.11: Growth of thin FeRh films on MgO substrates: (a) the temperature dependence of the misfit strain between MgO and FeRh (bottom plot) calculated from constituent lattice parameters $\frac{\sqrt{2}}{2}a_{\mathrm{MgO}}$ and a_{FeRh} (top plot) acquired via x-ray diffraction (XRD) technique by J. A. Arregi; (b) an FeRh FM island array on a MgO(001) substrate formed through the Volmer–Weber growth phenomenon; (c) an FeRh metamagnetic island array on a MgO(001) substrate self-assembled during solid-state dewetting.[1]

Figure 1.10). This AF-to-FM transition exhibits temperature hysteresis between heating and cooling cycles and thus an extraordinary amount of latent heat is released across the transition in the cooling direction. In addition, the transition is accompanied by an isotropic lattice expansion ($\sim 0.6\%$), a reduction in resistivity ($\sim 50\%$) and a large change in entropy. The versatility to trigger and control the transition, as well as the associated magnetization and magnetoresistance changes provide promising basis for novel metallic memory cells [54], magnetic recording [55] or magnetic refrigeration [56]. Besides, it has been recently found that the sensitivity of the phase transition to the environmental physical parameters (stress, temperature, magnetic fields) is dramatically enhanced when confining the material to sub-micron nanostructures [57].

Despite the extraordinary characteristics of FeRh, attempts to scale FeRh down to NPs on a large area (such as the entire area of a substrate) while maintaining the quality of the metamagnetic transition have rarely succeeded thus far. Instead, a number of works have reported that depositions of ultrathin FeRh films on MgO at elevated temperatures generally lead to direct nucleation of sub-100 nm nanoislands via the Volmer–Weber growth phenomenon. Islands grown via this route seem to be FM stabilized, with no or little fraction of the islands undergoing the metamagnetic phase transition and thus resulting in an almost complete suppression of the AF ordering [58–61]. Besides, Liu *et al.* [59] simultaneously supported the observation of FM stabilized FeRh islands through first-principles calculations considering the balance among the surface energies. Conversely, Barton and coworkers [62] suggest that a large majority of Volmer–Weber grown islands undergo the transition, but the behavior of individual nanoislands was not investigated.

[1] 3D images in Figure 1.11c–d correspond to the atomic force microscopy (AFM) micrographs represented in the program *Gwyddion 2.50*.

In the previous work by the author, it was confirmed that self-assembled FeRh islands grown via the Volmer–Weber mechanism at high temperatures (see Figure 1.11b) are indeed FM stabilized [63]. Following Young's equation (1.3), island-like formation of FeRh on top of oxide substrates is promoted by the balance of surface energies. Here, the surface energy $\gamma_{\mathrm{FeRh,\,MgO}}$ of the FeRh/MgO interface is an influential parameter and depends besides the natural difference of the phases and thus the strength of the chemical bonds also on the lattice misfit and on the intermixing of the constituent phases [64]. As the FeRh/MgO interface was found to be fully coherent for FeRh films [54], the major contribution to the surface energy $\gamma_{\mathrm{FeRh,\,MgO}}$ is given by the misfit strain between the MgO and FeRh lattices (a quadratic dependence), plotted vs temperature in Figure 1.11a. Within the shown temperature range (296–1200 K), the lattice of equiatomic FeRh epitaxially grown on MgO is always exerted to compressive in-plane strain. In this sense, the ever present strain in the whole temperature range helps promoting island-like growth as well, as a way to avoid epitaxial stress that would accumulate upon continuous film growth.

Opposite to this, it was also found that arrays with a majority fraction of metamagnetic islands are formed through a dewetting mechanism (see Figure 1.11c) [63] which has been already observed for many metals on oxide substrates. In this case, depositions of FeRh thin films are performed at lower temperatures (compared to those enabling Volmer–Weber growth) and self-assembled islands emerge via post-growth annealing which promotes hole formation ensued by a dewetting process in as-deposited metastable films. It was shown that the dewetting mechanism preserves epitaxy between FeRh and the substrate providing the desired B2-ordered (bcc-like) structure which is essential for the metamagnetic phase transition. Besides, we have observed that the shapes of the islands obtained via solid-state dewetting are qualitatively very different to those obtained via Volmer–Weber growth (see Figure 1.11b–c).

This thesis thoroughly examines the morphology and magnetic properties of FeRh self-assembled nanoisland arrays on a variety of substrates as a result of solid-state dewetting. Along with the expected AF-to-FM transition upon heating and FM-to-AF transition upon cooling, the phenomenon of supercooling is investigated via different experimental techniques. Besides, we discuss the implications of the FeRh island morphology in their magnetic behavior on different substrates. Subsequently, the oxide substrates with nanoisland assemblies are subjected to an etching process in order to release the nanoislands into a liquid environment. An attempt is made to separate the detached FeRh islands from the solution and to characterize their magnetic behavior across the transition.

Free-standing metamagnetic NPs could freely interact and control diverse entities at the nanoscale and can be thus of immense interest for a number of applications in biomedicine. Currently, the vast majority of MNPs in this direction are based on FM compounds profiting from the SPM limit upon size reduction, therefore avoiding undesired particle agglomeration. Employment of NPs presenting metamagnetism promises not only a negligible agglomeration tendency at human body temperature but also specific remote control of biological entities in terms of therapeutics, diagnostics or sensing while submitted to various driving forces. Additionally, the remarkable latent heat production could be applied to destroy cancer cells similarly to magnetic hyperthermia. Besides biomedicine, magnetic sensors and magnetic switches based on metamagnetic NPs can enrich domains such as environmental science or electronics. The easily controllable transition and its associated changes in magnetization, magnetoresistance and entropy can be favourably utilized to develop innovative magnetic recording and spintronic devices, or other applications in energy harvesting.

2 Self-assembly of FeRh islands on different substrates

This chapter describes the sample fabrication process and investigates the influence of different substrates on the final FeRh film or island morphology. The discussion of the equilibrium nanoisland shapes is based on surface energy and crystal structure arguments.

2.1 Fabrication process and methodology

All FeRh samples presented in this work were deposited using an ultra-high vacuum magnetron sputtering system (Bestec) from a single equiatomic FeRh target. The base pressure in the chamber was lower than $5 \cdot 10^{-8}$ mbar. Magnetron sputtering constitutes a physical vapor deposition (PVD) technique for fabrication of various thin films and coating types featuring exceptional adhesion of deposited material on a substrate.[1] Here, different single crystalline substrates including MgO(001), MgO(011), Al_2O_3(0001) and Si(001) were initially firmly mounted by molybdenum clamps to a sample holder made of stainless steel[2] (see Figure 2.1a). The size of the employed substrates was 5×5 mm^2 or 10×10 mm^2. The thermal treatment during the whole deposition process is described by the temperature profile shown in Figure 2.2. Prior to sputtering, the substrates were preheated to approximately 460 °C for 30 min. FeRh growth was performed at the same temperature using a power of 50 W and an Ar pressure of $2.7 \cdot 10^{-3}$ mbar. The typical deposition rate for FeRh under these conditions was around 0.33 Å/s, or 2 nm/min. The deposition time presented a variable parameter adjusted in order to fabricate samples with

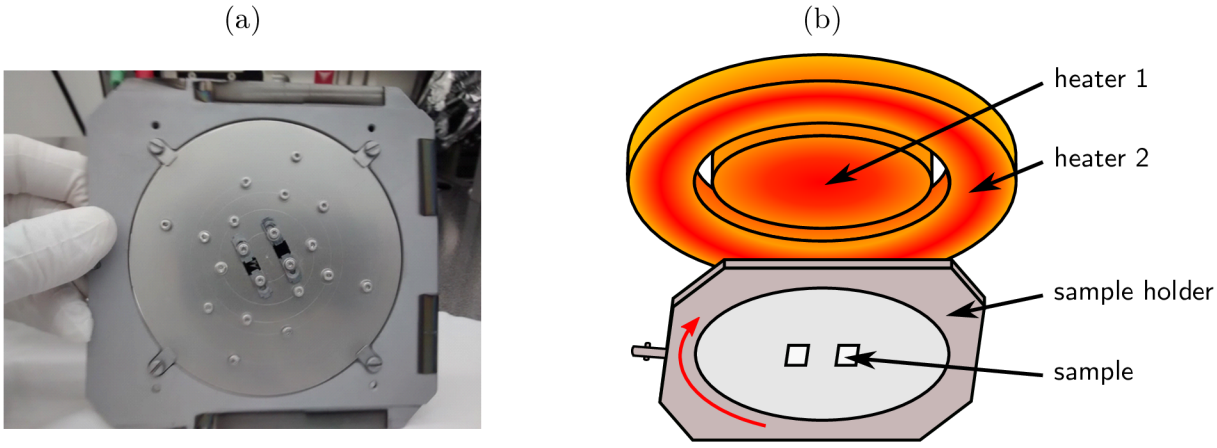

Figure 2.1: Sample positioning during the film growth and posterior annealing: (a) the photo of the sample holder made of stainless steel with two attached samples; (b) the scheme of the two heater elements (the red to yellow gradient demonstrates the inhomogeneous temperature distribution) used to warm the samples on the holder placed below (here the distance between the heaters and the sample holder is exaggerated to show the inhomogenity of the temperature distribution).

[1] A detailed description of the magnetron sputtering technique was given in the Bachelor's thesis of the author [63].

[2] A high Cr-content (> 17 at.%) austenitic stainless steel that can resist temperature cycling up to 900 °C was employed for the sample holder plate.

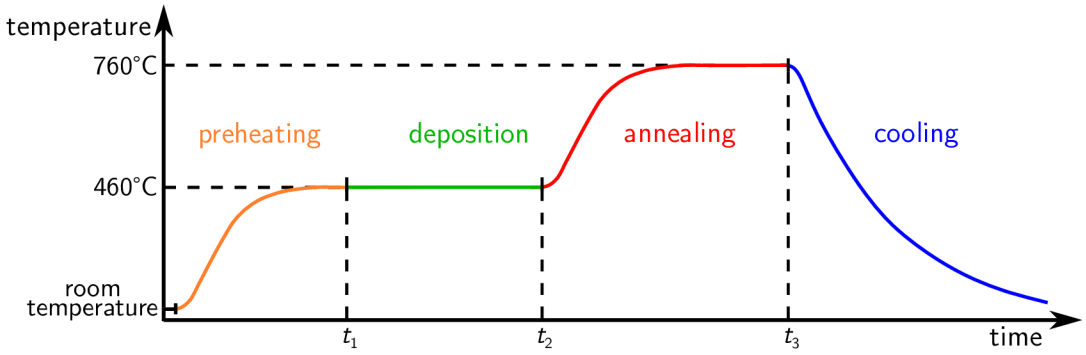

Figure 2.2: Graphical representation of the temperature development in the sample holder during the thin film fabrication process.

desired morphology. FeRh growth was ensued by a temperature increase up to 760 °C and a subsequent 80-min-long annealing process. The samples were taken out from the chamber to air once cooled down below 80 °C.

It turned out that the final FeRh morphology strongly depends even on slight variations during sputtering and posterior annealing which cannot be always sharply controlled. One of the most crucial factors here is the temperature in the sample holder. Despite the holder rotation of 20 rpm through the entire fabrication process aiming for spatial uniformity and thickness of the as-deposited material, the existence of temperature gradients across the sample holder cannot be completely avoided. The non-uniformity may partially arise as a result of the heater design in the sputter system. This consists of two concentric ceramic heater elements located right on top of the rotating sample holder with hotter centers (represented by a more intense red color in Figure 2.1b) compared to their edges. Consequently, substrates placed in different positions of the sample holder may experience slightly different temperatures. In order to minimize this effect, the same input voltage is fed to the two ceramic heaters at all times. Besides, uneven force exerted by the clamps on different substrates may also produce a better or worse thermal contact with the sample holder plate. As a consequence of both factors, the real temperature could be varied within ±40 °C from substrate to substrate. Another factor influencing the final morphology is the employed FeRh target. As each FeRh target can feature slightly different variations from equiatomic composition, the deposition parameters (e.g. Ar pressure) must be adjusted after each target exchange.

Finally, one must consider the history of the sputtering chamber in terms of possible sources of contaminants. Previously deposited materials attached to the walls of the chamber can be released during exposure to high temperatures, which can bring impurities and disorder into the grown samples. This can negatively impact the attainment of the desired B2-ordered structure of FeRh. Due to the aforementioned complications, the reproducibility between individual depositions is to a small extent compromised.

2.2 Morphology of FeRh islands on different substrates

The fabrication process was optimized for the purpose of obtaining nanoislands with different sizes and shapes while conserving the phase transition. As we initially observed that assemblies with a majority fraction of metamagnetic islands are formed through the mechanism of solid-state dewetting [63], our strategy consisted in tuning the dewetting process to fabricate samples with controlled morphology. It is generally known that thin films, featuring an enhanced surface area to volume ratio compared to the bulk, are

susceptible to the crystalline texture imposed by the substrate underneath. Therefore, in order to achieve various shapes of metamagnetic islands, FeRh samples shown in this thesis were grown on different single-crystal substrates, namely MgO(001), MgO(011) and Al_2O_3(0001), in addition to naturally oxidized Si(001). By varying both the FeRh growth direction and the induced strain in the FeRh film, the effect on the island sizes and shapes was investigated. Another parameter that was tuned for studying the effect on island morphology is the deposited film thickness. Besides, we discuss the degree of reproducibility in terms of the final FeRh morphology. Additionally, the homogeneity of morphology across the surface is examined on substrates of different sizes ($5 \times 5\,\mathrm{mm}^2$ and $10 \times 10\,\mathrm{mm}^2$).

The morphology of the samples was primarily characterized using atomic force microscopy (AFM) via a *Dimension Icon* instrument from Bruker corporation. Complementarily, a high resolution scanning electron microscope (SEM) *Verios 460 L* from FEI (currently Thermo Fisher Scientific) company was employed for obtaining wide-field microscope images of the samples (tens of microns). AFM which enables converting changes in the oscillation amplitude and phase of a vibrating cantilever to the height profile of an investigated surface area, was performed in a measurement configuration designated as *PeakForce Tapping* utilizing Co/Cr-coated MESP probes.[3] AFM images were subsequently processed in the program *Gwyddion 2.50* [65]. SEM images were conventionally obtained by collecting secondary or back scattered electrons using a low energy Everhart-Thornley detector.

A brief discussion of the most relevant findings concerning the growth of self-assembled FeRh follows in the next paragraphs of this section.

Effect of epitaxy on dewetting

In order to test the influence of different interface ordering on the dewetting process, single crystalline $5 \times 5\,\mathrm{mm}^2$ MgO(001), MgO(011), Al_2O_3(0001) and Si(001) substrates were selected for the present study. A good understanding of the FeRh crystallographic structure as well as of all the investigated substrates is essential for studying the morphologies that may arise from epitaxial growth. Here, we show the B2-ordered unit cell of the equiatomic FeRh and its principal planes (001), (011) and (111) (see Figure 2.3a). The lattice parameter for bulk FeRh (in the AF phase) is 2.988 Å and the second nearest distance between two Fe/Rh sites is $2.988\,\text{Å} \cdot \sqrt{2} = 4.226\,\text{Å}$ [66].

The epitaxial growth of FeRh films is often performed on MgO(001) substrates for promoting good matching between FeRh(001) and MgO(001) lattice planes, which is achieved through an in-plane 45° rotation (see Figure 2.3c). The lattice parameter of MgO is 4.212 Å and the nearest distance between two O^{2-}/Mg^{2+} sites is $4.212\,\text{Å} \cdot \frac{\sqrt{2}}{2} = = 2.978\,\text{Å}$, the latter providing a low mismatch template (0.3%) for FeRh growth, inducing a slight in-plane compression. As for FeRh on MgO(011), epitaxial film growth has not been reported. In principle, we expect a rectangular matching between FeRh(011) and MgO(011) planes with a misfit of 0.3% (see Figure 2.3d), resulting in a compressive in-plane deformation adopted by the FeRh film. In contrast to MgO(001) and MgO(011), the termination of the Al_2O_3(0001) surface features hexagonal, rather than square or rectangular, symmetry (see Figure 2.3b). The nearest distance between two O^{2-} sites in the Al_2O_3(0001) plane is 4.759 Å. The epitaxial growth of FeRh is achieved through matching with the FeRh(111) plane, developing a large in-plane tensile strain as a result

[3] A detailed description of AFM technique as well as of the configuration *PeakForce Tapping* was given in the Bachelor's thesis of the author [63].

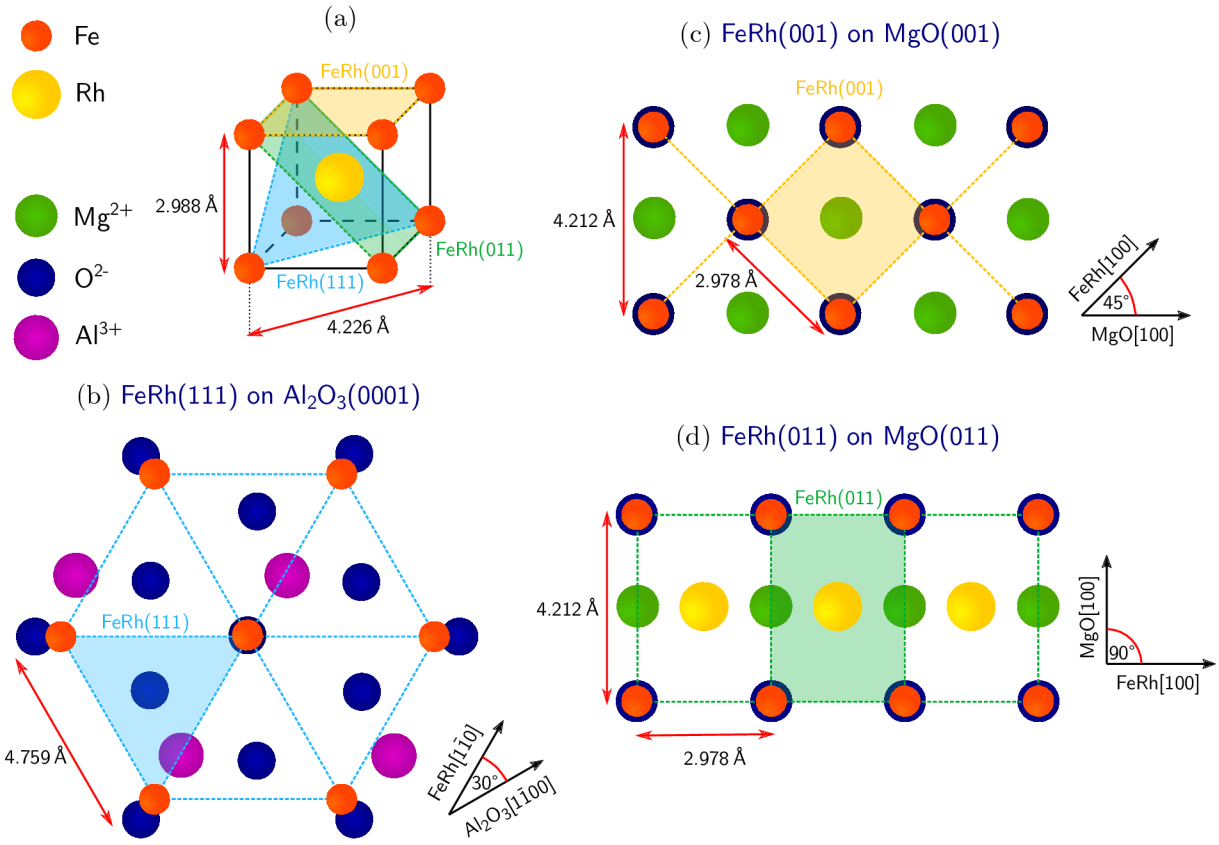

Figure 2.3: Growth of FeRh on different substrates based on estimated best epitaxial match: (a) the unit cell of FeRh and its principal planes (001), (011) and (111); (b) FeRh(111) on Al_2O_3(0001); (c) FeRh(001) on MgO(001); (d) FeRh(011) on MgO(011).

of a lattice mismatch of approximately 11%. Concerning the growth on Si(001) substrates, we have not found any suitable epitaxial matching for FeRh. However, we explore if solid-state dewetting of FeRh can occur on top of the amorphous native oxide (SiO_x) on the Si surface, as it should present lower surface energy in comparison to bare Si. In fact, it was often reported that solid-state dewetting of metallic films occurs on SiO_2, as in the case of Au [67].

Overall, we observe various induced in-plane symmetry configurations of FeRh due to different epitaxial matchings. As a consequence of this, one can expect also a difference in the equilibrium shapes of dewetted FeRh structures. However, the efficiency of the FeRh dewetting process on different surfaces is primarily unknown and needs to be investigated.

We initially show how dewetting is initiated in FeRh films on top of different substrates (see Figure 2.4). The FeRh films were grown following the deposition and annealing procedure described in Figure 2.2. However, the dewetting process did not advance enough to produce separated islands and remained at an early stage, most probably due to the non-ideal thermal contact of the substrates with the holder. In any case, this allowed us observing the initial steps of dewetting in each of the substrates. We see that dewetting on MgO(001), MgO(011) and Al_2O_3(0001) is initiated by the formation of holes with well-defined shapes (see Figure 2.4a–c). The variety of shapes among different substrates can be explained by different epitaxy (see Figure 2.3) and by the preferential crystallographic faceting of the FeRh film during dewetting, arising from the anisotropy of the surface energy in FeRh.

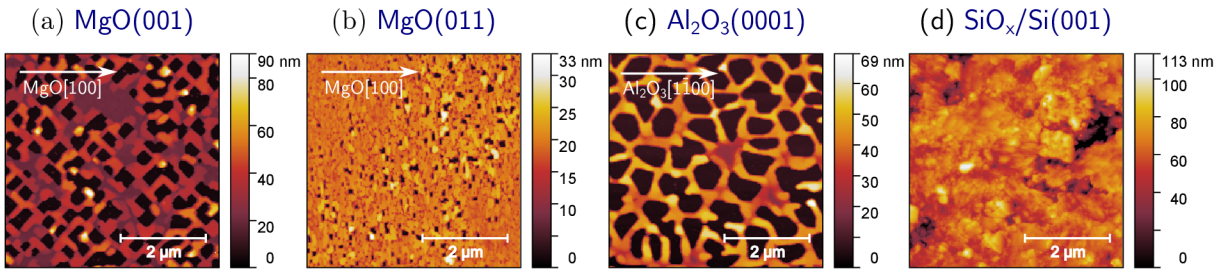

Figure 2.4: Early stage of FeRh film dewetting on different substrates: (a) MgO(001); (b) MgO(011); (c) Al_2O_3(0001). No specific shape was observed on (d) Si(001) substrate.

Dewetting on MgO(001) proceeds in a regular grid of square-shaped holes oriented preferably at ±45° away from MgO⟨100⟩ crystallographic orientations (see Figure 2.4a). This can be understood in terms of the 45° in-plane rotation of the FeRh unit cell with respect to the MgO lattice (see Figure 2.3c). For the case of MgO(011), dewetting seems to proceed by nucleation of rectangular-shaped holes oriented along the horizontal and vertical direction in the AFM scan (see Figure 2.4b). However, as dewetting was not particularly prominent for this sample, the existence of well-defined faceting fronts could not be concluded. As for Al_2O_3, the nucleated holes reveal hexagonal, rather than rectangular, periodicity (see Figure 2.4c) which corresponds to the three-fold azimuthal symmetry of the epitaxial relation between Al_2O_3 and FeRh (see Figure 2.3b). In summary, we observe that the epitaxy between the substrate and the FeRh overlayer promotes anisotropic dewetting which is highly dependent on the crystalline texture in the FeRh film.

Finally, FeRh films were grown on SiO_x/Si substrates following the same procedure as for MgO and Al_2O_3 substrates. We conclude that the SiO_x termination does not lead to any pronounced dewetting for FeRh films grown on top as it was the case for MgO and Al_2O_3, with no specific shape of FeRh being formed (see Figure 2.4d). Therefore, we did not continue in its investigation of potential island formation through dewetting.

Effect of film thickness

The film thickness represents a crucial parameter for the purpose of reaching well-separated islands. Initially, we employed the MgO(001) substrate system for investigating the effect of varying the nominal thickness[4] of the deposited FeRh layer. We firstly deposited a relatively thick layer (40 nm) before preparation of thinner ones to investigate the dewetting limit. AFM scans of the obtained samples over a 5×5 µm^2 area are shown in Figure 2.5. In particular, we obtained:

(i) Sample M(001)-40, with a nominal thickness of 40 nm, consists of a quasi-continuous film which is disrupted by square-shaped holes (see Figure 2.5a). While the smaller grooves generally do not penetrate the film down to the substrate, a few bigger holes are surrounded by a thickened rim suggesting a deeper penetration and thus a more pronounced dewetting stage.

(ii) Sample M(001)-20, with a nominal thickness of 20 nm, features maze-like islands that extend between 500 nm and 2 µm in size (see Figure 2.5b). A considerable part of the MgO substrate is exposed in this sample.

(iii) Sample M(001)-16b possesses a nominal thickness of 16 nm and contains well-separated, round-shaped islands (see Figure 2.5c).

[4]The equivalent thickness of a continuous FeRh film.

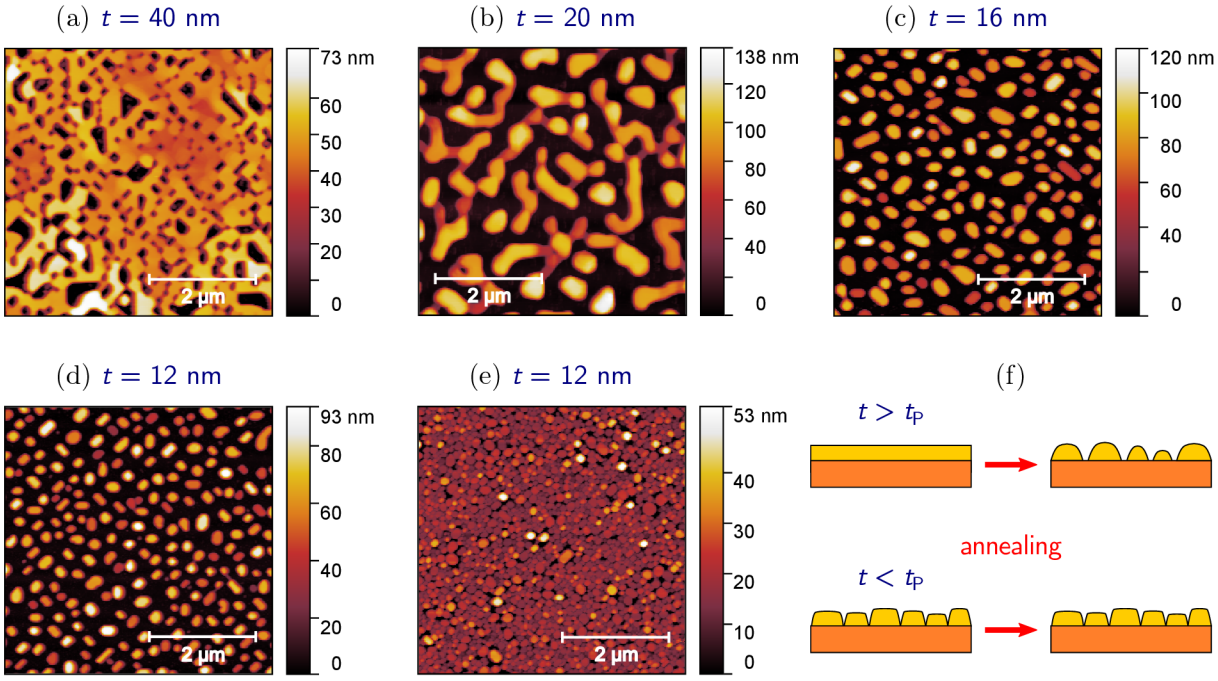

Figure 2.5: AFM images of FeRh films for decreasing deposited nominal thickness t on MgO(001) substrates: (a) sample M(001)-40, 40 nm; (b) sample M(001)-20, 20 nm; (c) sample M(001)-16b, 16 nm; (d) sample M(001)-12a, 12 nm; (e) sample M(001)-12b, 12 nm. (f) Schematics explaining the different morphology in (d) and (e) based on threshold thickness t_P.

(iv) Sample M(001)-12a, with a nominal thickness of 12 nm, shows a morphology with well-separated, sub-300-nm islands (see Figure 2.5d). Sample M(001)-12b consists in a repetition of the same procedure used to grow sample M(001)-12a. However, the resulting morphology differs from the previous sample in that the film displays tiny, densely packed islands often showing sub-100-nm sizes (see Figure 2.5e). While the islands seem to be physically separated, the substrate is only slightly exposed.

The three thickest samples considered here (40 nm, 20 nm and 16 nm) show a characteristic morphology which derives from solid-state dewetting. A continuous film is formed during growth followed by a void nucleation and deepening during the post-growth annealing. The early stage of dewetting in sample M(001)-40 is clearly visible by the presence of holes in the otherwise continuous film. As the thickness of deposited material is reduced from 40 nm to 20 nm, the grooves in the film could grow more prominently during the 80-min-long post-growth annealing, leading to a worm-like island morphology for sample M(001)-20, featuring partially interconnected islands. Further, even thinner deposited layers of 16 nm thickness for sample M(001)-16b shows an evolution into very well-separated islands resulting from the same annealing procedure. Our observation of a more pronounced dewetting for thinner films is in line with previous works. It has been reported that the threshold temperature at which dewetting occurs, as well as the island size and spacing decrease with the film thickness (see Section 1.2 and references [31, 34]).

However, when the thickness was reduced down to 12 nm, two distinctively different island morphologies are observed. Sample M(001)-12a follows in succession to previously explained dewetting phenomenon upon thickness reduction. In contrast, the island spacing of sample M(001)-12b did not increase but rather vanished, as the sample consists of very closely spaced tiny islands. We argue for the existence of a threshold thickness t_P

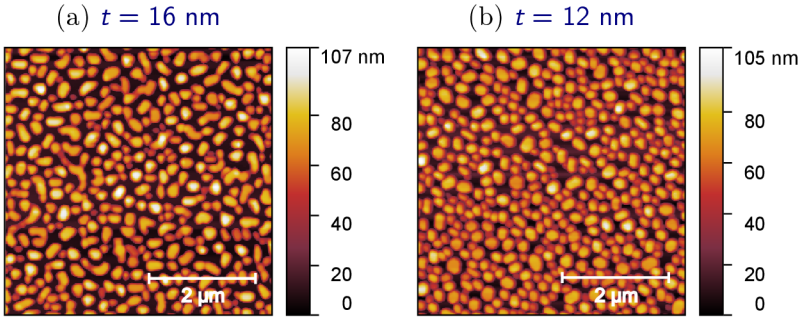

Figure 2.6: AFM images of FeRh films for decreasing deposited nominal thickness on Al_2O_3(0001) substrates: (a) sample A(0001)-16, 16 nm; (b) sample A(0001)-12, 12 nm.

below which percolation into a thin continuous film does not occur at any stage during deposition, and thus solid-state dewetting during annealing cannot happen (see Figure 2.5f). Instead, we conclude that in such a case small-size islands nucleate through Volmer–Weber growth which do not succumb to any significant change during annealing. Therefore, equilibrium growth can dominate even at our deposition temperature of 460 °C, as a consequence of the reduced amount of deposited material and the relatively slow kinetics resulting from the growth rate. Here, we are approaching the percolation threshold with films possessing a nominal thickness of 12 nm. Slight deviations in the growth rate or in the substrate temperature near the percolation limit can alter the self-assembly route in the sample, promoting either continuous layer formation ensued by dewetting or island nucleation through Volmer–Weber growth.

Similarly, we also tested the effect of the nominal thickness on the final FeRh morphology on Al_2O_3(0001):

(i) Sample A(0001)-16 with a nominal thickness of 16 nm shows a morphology with well-separated islands of characteristic sizes well below 500 nm (see Figure 2.6a).

(ii) Sample A(0001)-12 possesses a nominal thickness of 12 nm and contains separated, sub-200-nm-sized nanoislands (see Figure 2.6b).

Both samples show an island-like morphology with solid-state dewetting, in which again the island size reduces upon lowering the nominal thickness. In general, it was observed that self-assembly into islands is more common on Al_2O_3 as compared to Mgo. This may point to role of the more prominent epitaxial strain, and in turn to the associated presence of defects (e.g. dislocations, stacking faults) arising from the very large mismatch for FeRh growth on Al_2O_3.

Impact of temperature and nucleation sites

Despite the trend observed on samples featuring different thickness (as shown in Figure 2.5), we have noticed sample-to-sample variations in morphology even in the case of same nominal thickness and equivalent preset parameters. The slight deviations in reproducibility can be explained by the arguments discussed in the last paragraph of Section 2.1, primarily pointing to temperature gradients across the sample holder. Besides, the substrate surface quality also plays a key role in terms of its regularity and the presence of defects. The latter influence the number of nucleated holes per area in the dewetting process, as groove nucleation precisely starts at defects or triple-points.

To illustrate these effects, four layers with a nominal thickness of 16 nm were fabricated by the same deposition procedure on MgO(001) and subsequently subjected to

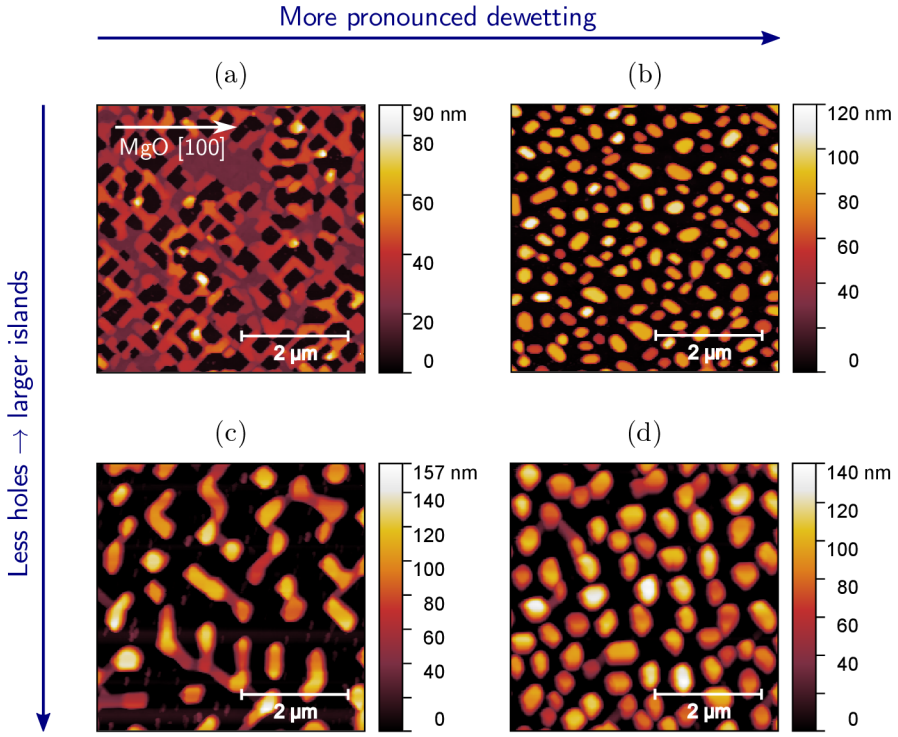

Figure 2.7: AFM images of FeRh samples with nominal thickness of 16 nm fabricated by the same procedure on MgO(001): (a) sample M(001)-16a features sub-micron square-shaped holes, showing a less advanced dewetting compared to the nanoisland morphology of (b) sample M(001)-16b; (c) sample M(001)-16c displays large spacing between elongated, wire-like islands, characteristic of a less advanced stage of dewetting compared to (d) sample M(001)-16d.

the standard annealing process. However, samples M(001)-16a, M(001)-16b, M(001)-16c and M(001)-16d all manifest slightly different morphologies (see Figure 2.7a–d). Sample M(001)-16a shows a regular grid of square-shaped holes revealing the MgO substrate below. We assume that the apparent dewetting process initiated in the sample would continue in island shaping if a longer annealing time or a higher temperature was provided at this stage. A considerably more advanced dewetting stage is evidenced via the nanoisland morphology displayed by sample M(001)-16b, showing well-separated and round-shaped islands with diameters well below 500 nm. On the other hand, sample M(001)-16c contains well-spaced and long wire-shaped islands that frequently display a characteristic mass weakening at the island centers. The material seems to be accumulated in the outer parts of the wires instead, from which we argue that upon prolonging the dewetting process further edge retraction and rim formation would have followed. Upon longer annealing, one could obtain well-separated islands, similar to those seen for sample M(001)-16d but with even larger island-to-island spacing. Compared to samples M(001)-16a and M(001)-16b, samples M(001)-16c and M(001)-16d present lower areal density of groove nucleation. This results in a lower density distribution of wider islands, in contrast to the cases with more closely spaced and smaller islands, despite the same nominal deposition and annealing parameters employed in all cases. Thus, the density of defects on the substrate, together with the higher or lower particular temperature reached at each substrate, seems to strongly impact the island size and the island-to-island distance.

In conclusion, we have found that while we can control the FeRh morphology to a great extent, its precise fine tuning is challenging, mainly due to temperature gradients in the sample holder during heating and due to the substrate irregularities, directly related to the number of nucleation sites in the film.

Morphological homogeneity and large area MgO(001)

All our $5 \times 5\,\mathrm{mm}^2$ samples feature a large regularity across several tens of microns and beyond. To demonstrate this, we show SEM images of samples M(001)-20 (see Figure 2.8a), M(001)-16d (see Figure 2.8b), M(001)-16a (see Figure 2.8c) and M(001)-16b (see Figure 2.8d). All SEM micrographs corroborate the regularity of the observed morphologies over a large spatial extent.

In order to explore the option to produce FeRh nanoislands via dewetting in very large amounts, we employed larger area MgO(001) substrates. Even though self-assembly of islands was achieved on $10 \times 10\,\mathrm{mm}^2$ substrates, the large area morphological homogeneity observed in the $5 \times 5\,\mathrm{mm}^2$ substrates was partially disrupted (see Figure 2.9). While an area with the desired island-like architecture emerges close to one edge of the substrate (see Figure 2.9d), the sample exhibits all stages of dewetting across its surface (see Figure 2.9a–d) and becomes a continuous film with a few square voids towards the other edge (see Figure 2.9a). The wide-area optical microscope images corresponding to the parts of the sample showed in detail in Figure 2.9a–d can be seen in Figure 2.9e–h. We ascribe this non-uniformity to an inhomogeneous temperature distribution in the sample holder during

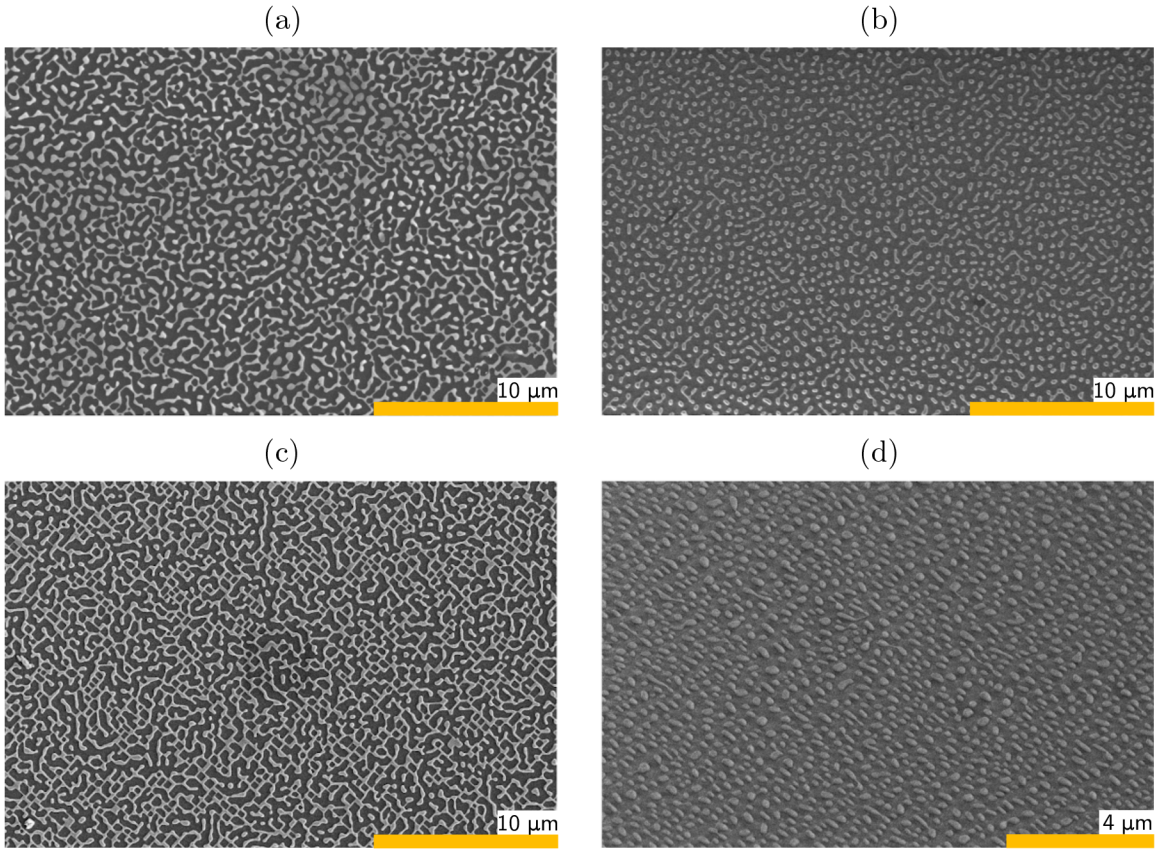

Figure 2.8: Wide-area SEM images of samples: (a) M(001)-20; (b) M(001)-16d; (c) M(001)-16a; (d) M(001)-16b. Micrographs (a)–(c) are acquired at normal incidence, whereas a 50° sample tilt was used in (d). Images were taken by M. Staňo.

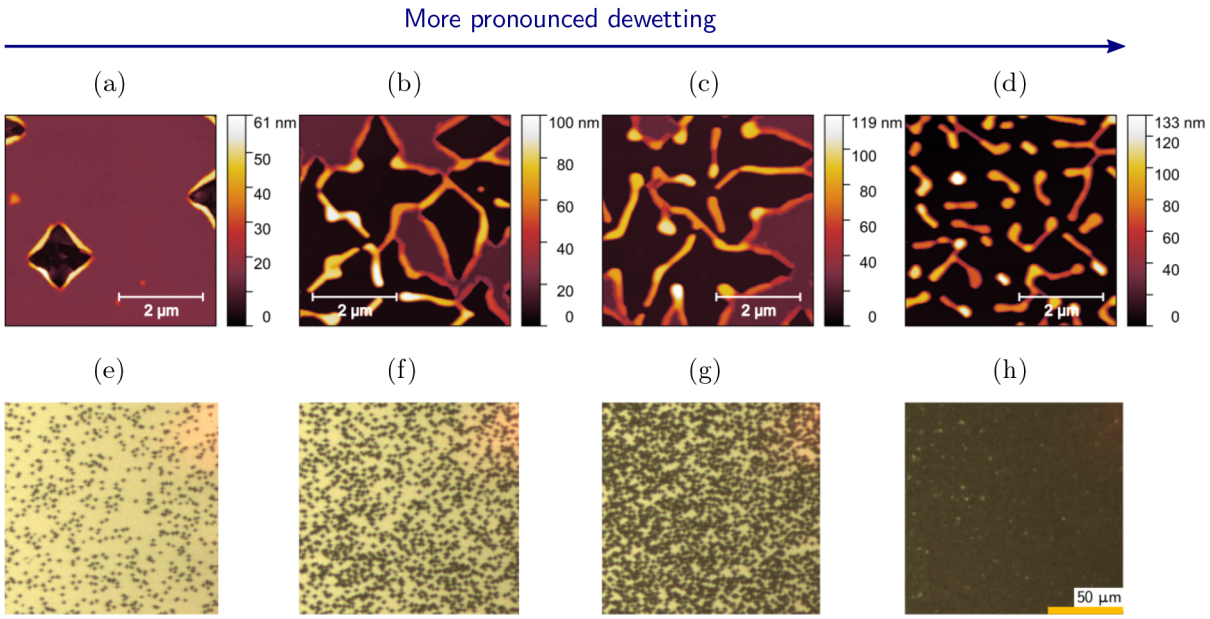

Figure 2.9: AFM (a–d) and optical microscope (e–h) images for an FeRh layer on a $10 \times 10\,\mathrm{mm}^2$ MgO(001) substrate showing different stages of dewetting ranging from (a) and (e) a continuous film with a few square voids on one part of the sample to (d) and (h) well-separated islands on another part.

annealing, which is most probably caused by the enhanced thermal contact provided by the clamps used to fix the substrate to the holder. Despite placing the clamps symmetrically onto the substrate, the slightly unequal compressing pressure exerted on both edges may cause a slight temperature distribution from one edge to the other. This effect is more noticeable in larger substrates, while it did not show to be significant in $5 \times 5\,\mathrm{mm}^2$ substrates.

2.3 Nanoisland shape analysis via Winterbottom construction

In general, we observe well-pronounced crystallographic faceting of our FeRh samples. In this section, we compare their experimentally determined shapes with their equilibrium Winterbottom prediction. For the following analysis, we used the *Python* package *WulffPack* to determine the equilibrium shapes of FeRh islands on different substrates, namely MgO(001), MgO(011) and Al_2O_3(0001). The required values of surface energy for the FeRh(001), (011) and (111) planes were obtained from the theoretical calculations at 0 K performed by Liu *et al.* [59].[5] The value of energy for the FeRh/substrate interface (which is non-trivial to determine) only influences the height at which the crystallite is cut.

MgO(001)

The equilibrium shape of an FeRh crystal consists of a 26 facet non-uniform polyhedron. The Winterbottom construction of FeRh on MgO(001) shows a four-fold in-plane symmetry and features an octagonal projection if viewed from the top (see Figure 2.10d–e). Here, we show the sample M(001)-16c grown on MgO(001), containing facetted islands formed via dewetting with edges oriented preferably at ±45° from the MgO ⟨100⟩ crystallographic

[5] The values of surface energy for the FeRh(001), (011) and (111) planes (in AF phase as used here) are listed in Table 3.1.

orientation (see Figure 2.10a–c), similarly as the edges of grooves in Figure 2.4a. The visual inspection of the islands, revealing octagonal shapes, gives a hint about the possible development towards equilibrium shapes shown in Figure 2.10d–e. To test this hypothesis, we selected an octagonal island marked in green in Figure 2.10b and we drew a red dashed line going under 45° from the vertical direction in the AFM scan across the island (see Figure 2.10c). The orientation and position of the line were equivalently selected in the top view of the Winterbottom construction (see Figure 2.10e). The red dashed line corresponds to the path across the particle which follows the directions marked in colors according to the intersecting facets in Figure 2.10d. These lattice directions were identified via the orientations given by the Miller indices along the facets in the Winterbottom construction, thus allowing to calculate their relative angles. Subsequently, a height profile was acquired from the measured AFM image (along the dashed line in Figure 2.10c) and plotted by the red curve in Figure 2.10f with an equivalent aspect ratio

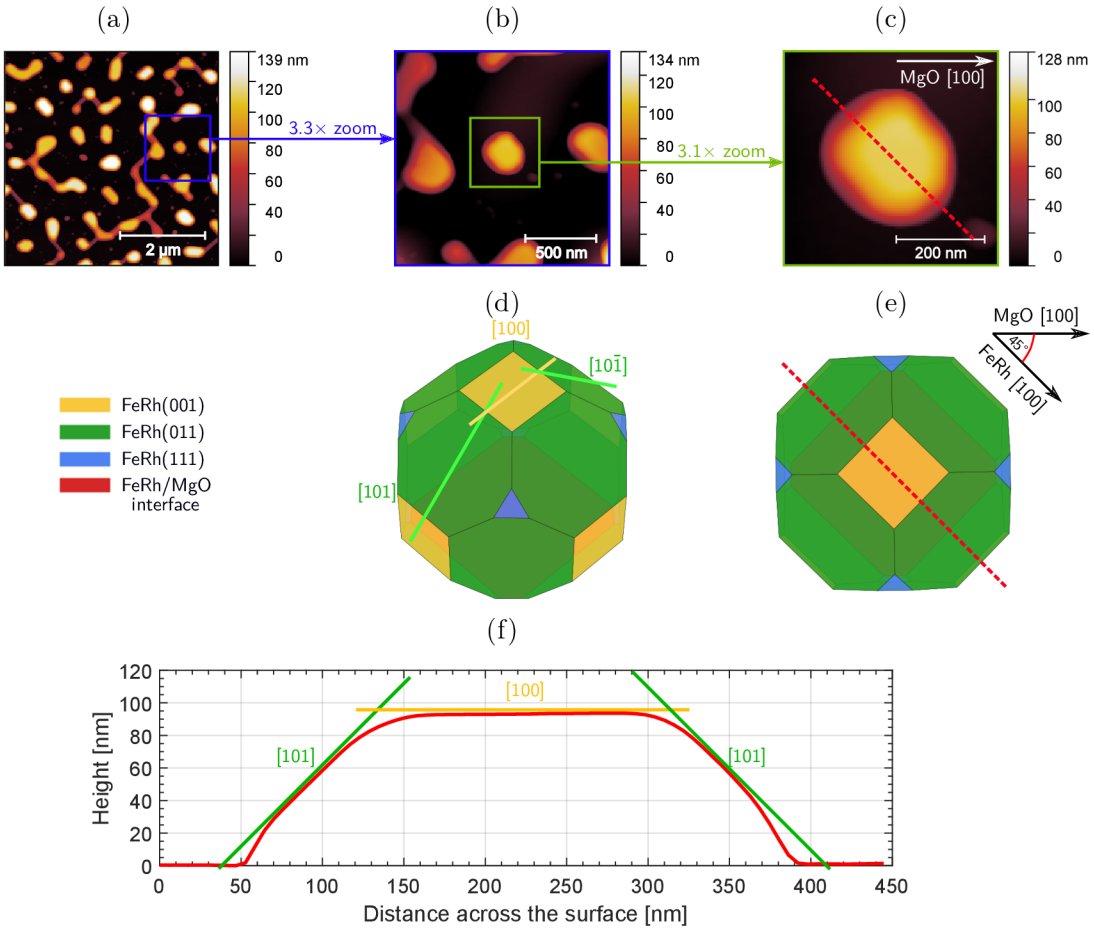

Figure 2.10: Nanoisland shape analysis of FeRh on MgO(001): (a) AFM image of sample M(001)-16c; (b) high-resolution image of a 1.5 × 1.5 µm^2 region from (a); (c) close-up of a 300-nm-wide island from (b). The dashed line indicates the position of the line-scan shown in (f). (d) Oblique view of the FeRh(100)/MgO(001) Winterbottom construction, showing the FeRh lattice directions corresponding to the facet path across the particle as indicated in (e). (e) Top view of the Winterbottom construction, showing a comparable projection of the island shape experimentally observed in (c). (f) Experimental height profile extracted from the line-scan in (c). Superimposed straight lines indicate the facet directions as theoretically extracted from the Winterbottom construction in (d) and (e).

of 1 : 1. The lattice directions from the Winterbottom construction were drawn following their corresponding orientations and matched with the height profile (see Figure 2.10e). The excellent matching of the experimental line profile with the predicted Winterbottom construction is indicative of the thermodynamically driven self-assembly process occurred upon dewetting.

MgO(011)

In comparison to the equilibrium shape of FeRh on MgO(001), which showed a four-fold in-plane symmetry, the Winterbottom construction of FeRh on MgO(011) exhibits a two-fold or uniaxial in-plane symmetry (see Figure 2.11d–e) due to the rectangular in-plane matching of the FeRh unit cell with the underlying MgO(011) (see Figure 2.3d).

In fact, the islands formed via dewetting in sample M(011)-16 indeed possess highly anisotropic shapes, in which elongated islands assemble with their long axis oriented along

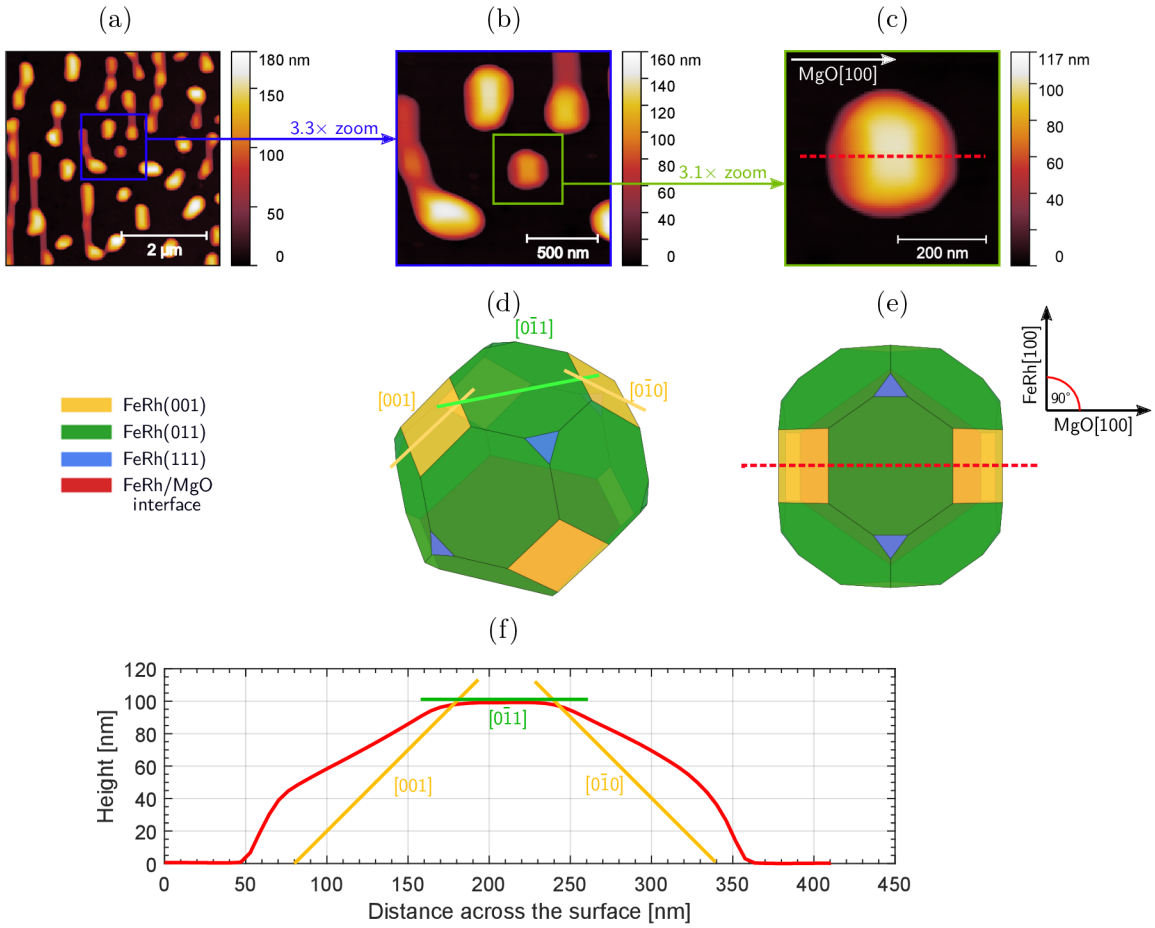

Figure 2.11: Nanoisland shape analysis of FeRh on MgO(011): (a) AFM image of sample M(011)-16; (b) high-resolution image of a 1.5 × 1.5 µm^2 region from (a); (c) close-up of a 300-nm-wide island from (b). The dashed line indicates the position of the line-scan shown in (f). (d) Oblique view of the FeRh(100)/MgO(011) Winterbottom construction, showing the FeRh lattice directions corresponding to the facet path across the particle as indicated in (e). (e) Top view of the Winterbottom construction, showing a comparable projection of the island shape experimentally observed in (c). (f) Experimental height profile extracted from the line-scan in (c). Superimposed straight lines indicate the facet directions as theoretically extracted from the Winterbottom construction in (d) and (e).

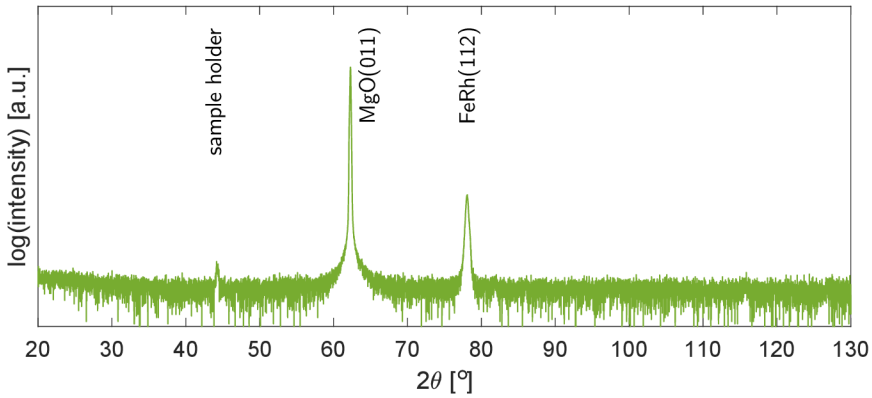

Figure 2.12: Symmetric θ–2θ XRD scans for sample M(011)-16 grown on MgO(011) using an x-ray wavelength of 1.5406 Å. Data acquired by J. A. Arregi.

the vertical direction in the AFM scan (see Figure 2.11a). In order to see if the island morphology matches the Winterbottom construction with the out-of-plane FeRh(011) orientation, we acquired a high-resolution AFM image (see Figure 2.11b) and selected a 300-nm-wide island, detailed in Figure 2.11c. The red dashed line going across the island along the horizontal direction was equivalently drawn in the top view of the Winterbottom construction (see 2.11e) and the path was described using Miller indices (see 2.11d). Thereafter, a height profile was extracted from the high-resolution AFM image (along the dashed line in Figure 2.11c) and plotted by the red curve in Figure 2.11f. The lattice directions determined from the Winterbottom construction are additionally shown. The experimental height profile reveals a path across well-pronounced facets, which however does not match with the predicted crystallographic directions. We found that the unmatched directions in the height profile could be all appropriately fitted with the FeRh$\langle 013 \rangle$ directions, which however does not explain the reason for the suppression of low-energy, low-index FeRh$\{100\}$ facets.

In order to test whether we assigned the right in-plane orientation of the Winterbottom construction to the selected island, we studied the sample via x-ray diffraction (XRD). Initially, we performed symmetric $\theta-2\theta$ scans, which surprisingly did not reveal any peak in the region corresponding to the FeRh(011) reflection (located at $2\theta = 42.7°$). Instead, we have found an FeRh peak corresponding to the reflection from FeRh(112) planes (see Figure 2.12). The wrongly assumed FeRh(011) texture explains the incorrect matching of the selected island facets with the predicted Winterbottom construction in Figure 2.11. In fact, it has been already observed that a number of materials with body-centered cubic structure grow with the high-Miller-index (112) texture on MgO(011). Some examples include metals such as Fe and Cr, despite the large misfit strain developed along one of the in-plane directions [68, 69].

If FeRh grows with (112)-orientation on MgO(011) substrates, we cannot further consider the FeRh(011)/MgO(011) epitaxial matching shown in Figure 2.3d. Instead, we show the FeRh(112) plane indicated with three unit cells (see Figure 2.13a) and the epitaxial matching between the MgO(011) termination and the FeRh(112) plane (see Figure 2.13b). Epitaxy occurs even under a considerable mismatch of 13% along MgO$[0\bar{1}1]$ direction with the mismatch being just 0.3% along the other in-plane direction (along MgO[100] direction).

In order to determine which in-plane direction of the sample M(011)-16 corresponds to the FeRh$[\bar{1}10]$ direction (as shown in Figure 2.13b), we measured the azimuthal φ scans

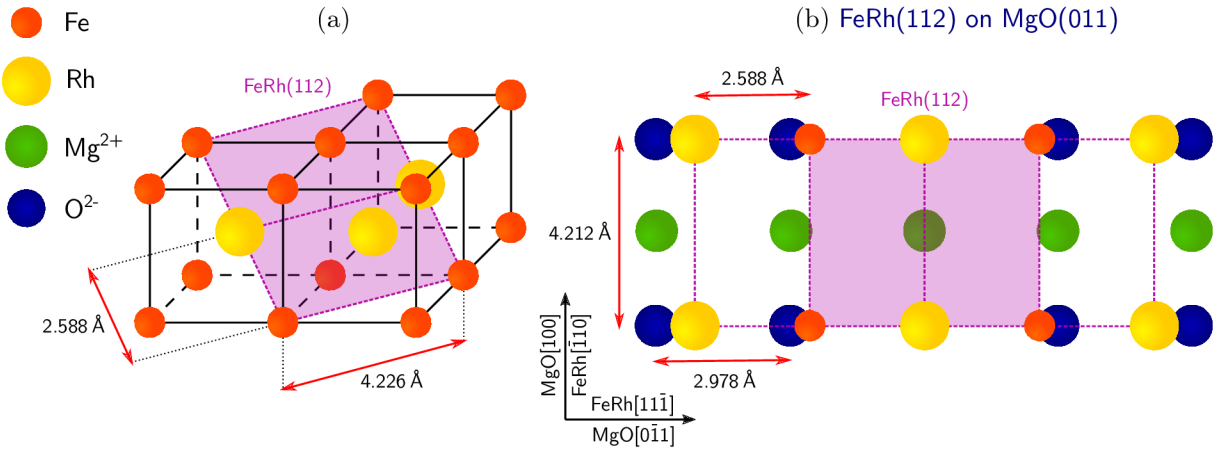

Figure 2.13: Epitaxial growth of FeRh(112): (a) the FeRh(112) plane represented over three primitive unit cells of FeRh; (b) epitaxial matching of FeRh(122) and MgO(011).

obtained in the asymmetric x-ray reflection geometry [66] performed on the FeRh(022) planes (not shown). Additionally, we collected the φ scans in the configuration aiming for the MgO(222) reflection. According to the observed reflections, we oriented the selected island of sample M(011)-16 as marked in Figure 2.14a (only the MgO[100] direction is shown, remaining directions are rotated to match the relations presented in Figure 2.13).

In view of the determined in-plane epitaxial orientations for FeRh(112) on MgO(011), it can be concluded that the long axis of the islands shown in Figure 2.11a corresponds to the high-mismatch in-plane orientation of epitaxy (see Figure 2.13b). While one could expect that the resulting islands would be preferentially narrower along this high mismatch orientation (hence realeasing epitaxial stress), the fine balance of anisotropic surface energies, presence of defects and other parameters determine mass transport during dewetting.

The Winterbottom construction of FeRh on MgO(011) was reconsidered upon revealing the right (112) texture. Here, we had to introduce an additional surface energy value for the FeRh(112) planes, which however could not be found in literature.[6] We chose the FeRh(112) surface energy to be higher than the value for FeRh(001) and FeRh(011), but smaller than for FeRh(111), for the purpose of revealing the otherwise hidden FeRh(112) planes.[7] Besides, we slightly fine-tuned the surface energy values for the FeRh(011) and FeRh(111) planes in order to mimic accurately the experimental profiles.[8] The resulting FeRh(112)/MgO(011) Winterbottom shape is viewed from top in Figure 2.14b.

To compare our structures to the equilibrium FeRh(112)/MgO(011) Winterbottom construction, we drew two perpendicular dashed lines going across the selected island and equivalently across the Winterbottom construction (see the red and dark blue lines in Figure 2.14a–b). The red and dark blue dashed lines correspond to the paths across the particle, following the directions described by the Miller indices in Figure 2.14c and Figure 2.14d, respectively. Height profiles acquired from Figure 2.14a along the red line and the dark blue line are plotted by the red curve in Figure 2.14d and by the dark blue curve

[6] Liu *et al.* [59] did not consider the FeRh(112) planes.

[7] In fact, calculations using density functional theory established that the surface energy is lower for (112) than for (111) in the case of Fe [70].

[8] The precise values of surface energy for FeRh(112) on MgO(011) can be different from those presented by Liu *et al.* [59] due to the large FeRh unit cell distorsion in one in-plane direction. The specific surface energy values used for the FeRh(112)/MgO(011) Winterbottom construction are: FeRh(001) - 2.274 J/m^2 (not changed), FeRh(011) - 2.2 J/m^2 ($\sim$5% larger), FeRh(112) - 2.3 J/m^2, FeRh(111) - 2.4 J/m^2 ($\sim$1.3% smaller). The values influence the length and area ratio of individual facets, not their respective angles.

in Figure 2.14f, respectively. The lattice directions from the Winterbottom construction (see Figure 2.14c and Figure 2.14e) were drawn following their corresponding orientations and matched with the height profiles (see Figure 2.14d and Figure 2.14f).

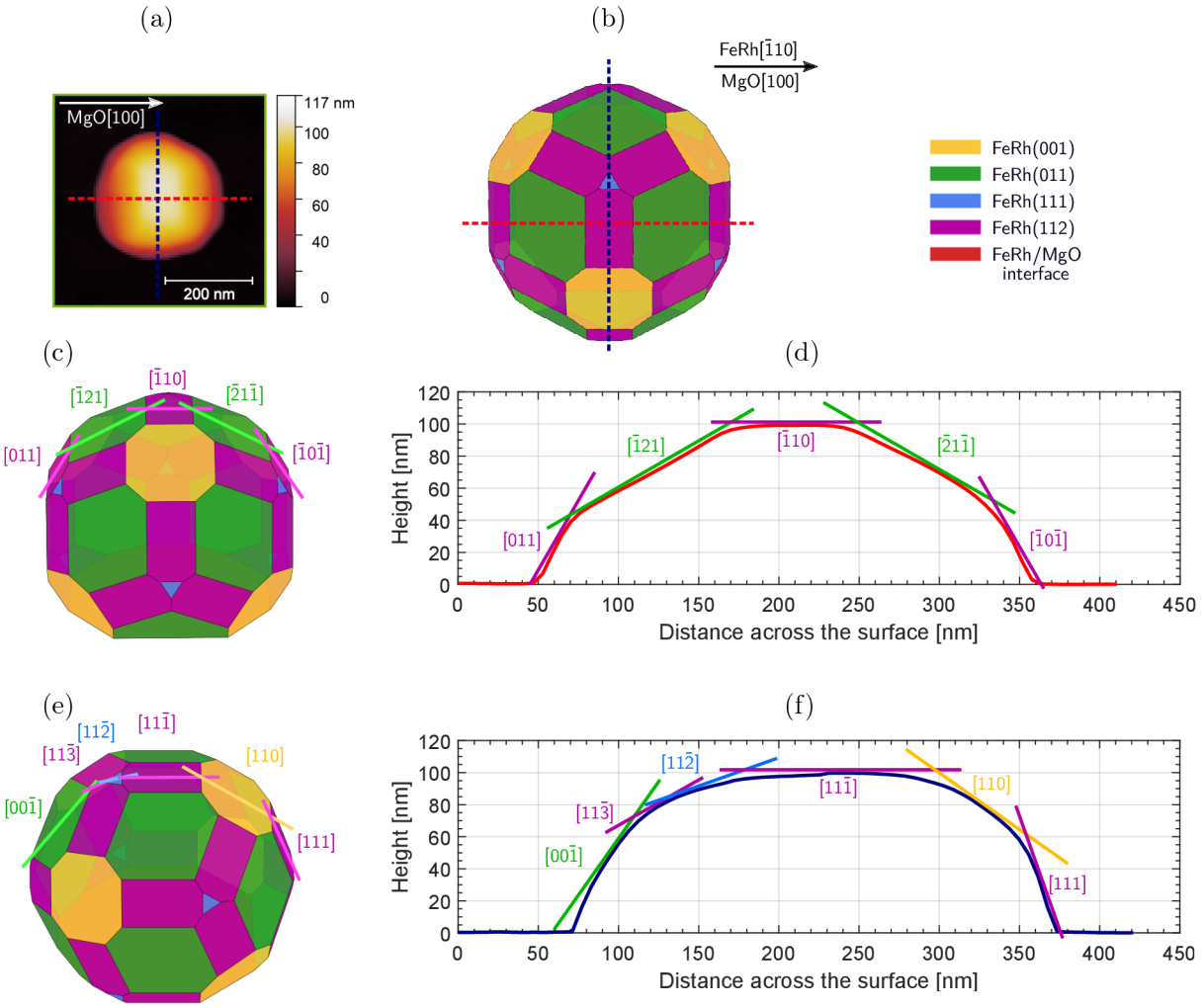

Figure 2.14: Nanoisland shape analysis of FeRh(112) on MgO(011): (a) high-resolution AFM image of a 300-nm-wide island from a region of sample M(011)-16 shown in Figure 2.11a–b. The red and dark blue dashed lines indicate the positions of the line-scans shown in (d) and (f), respectively. (b) Top view of the FeRh(112)/MgO(011) Winterbottom construction, showing a comparable projection of the island shape experimentally observed in (a). The dashed lines indicate the facet paths selected for the analysis. (c) Oblique view of the Winterbottom construction, showing the FeRh lattice directions corresponding to the facet path across the particle as indicated by the red dashed line in (b). (d) The experimental height profile extracted from the linescan along the red dashed line in (a). Superimposed straight lines indicate the facet directions as theoretically extracted from the Winterbottom construction in (b) and (c). (e) Oblique view of the Winterbottom construction, showing the FeRh lattice directions corresponding to the facet path across the particle as indicated by the dark blue dashed line in (b). (f) The experimental height profile extracted from the linescan along the dark blue dashed line in (a). Superimposed straight lines indicate the facet directions as theoretically extracted from the Winterbottom construction in (b) and (e).

$Al_2O_3(0001)$

The equilibrium shape of FeRh on Al_2O_3 predicted through the Winterbottom construction exhibits a characteristic hexagonal projection if viewed from the top (see Figure 2.15d–e). The equilibrium shape, however, reveals a three-fold azimuthal symmetry due to the facet disposition. One may notice that the islands formed via dewetting in sample A(0001)-16 as well as the nucleated holes in the layer shown in Figure 2.4c reveal hexagonal shapes. To verify the evolution of our sample to equilibrium shapes, we selected a hexagonal island marked in green in Figure 2.15b. We drew a red dashed line going from one corner to the other (see Figure 2.15c), which was equivalently selected in the top view of the Winterbottom construction (see Figure 2.15e). The red line corresponds to the path across the particle shown in Figure 2.15d. The lattice directions, intersecting facets or facet edges, were identified with the Miller indices. A height profile was extracted from the measured AFM image (along the dashed line in Figure 2.15c) and

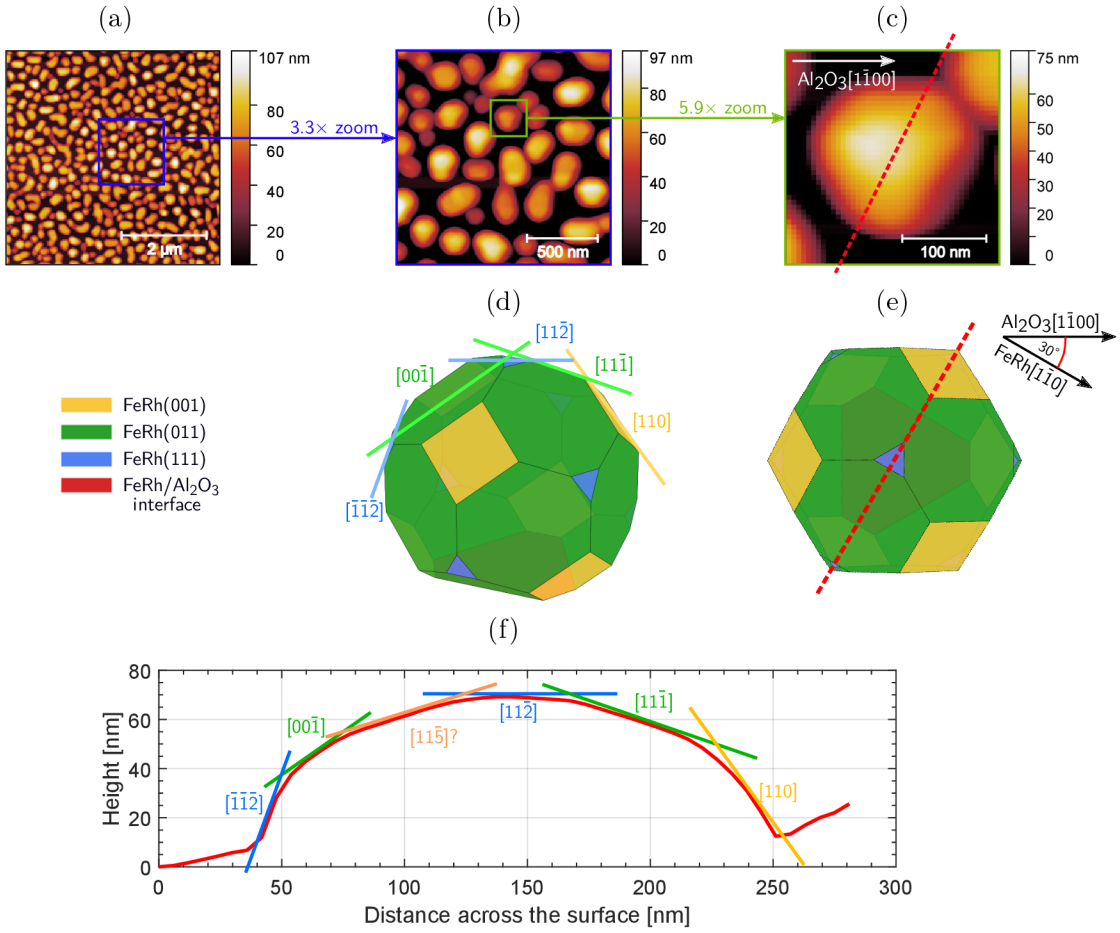

Figure 2.15: Nanoisland shape analysis of FeRh on $Al_2O_3(0001)$: (a) AFM image of sample A(0001)-16; (b) high-resolution image of a 1.5×1.5 µm^2 region from (a); (c) close-up of a 200-nm-wide island from (b). The dashed line indicates the position of the line-scan shown in (f). (d) Oblique view of the FeRh(100)/Al_2O_3(0001) Winterbottom construction, showing the FeRh lattice directions corresponding to the facet path across the particle as indicated in (e). (e) Top view of the Winterbottom construction, showing a comparable projection of the island shape experimentally observed in (c). (f) Experimental height profile extracted from the line-scan in (c). Superimposed straight lines indicate the facet directions as theoretically extracted from the Winterbottom construction in (d) and (e).

plotted by the red curve in Figure 2.15f. The lattice directions from the Winterbottom construction were drawn following their corresponding orientations and matched with the height profile (see Figure 2.15f). It was necessary to add one more direction (marked by the orange line) in order to replicate the entire profile. This slight discrepancy can be explained by the large width (compared to the height) of the selected particle and by the high surface energy of the top (111) plane, which could easily break into facets with a lower area. Despite this very minor difference, the agreement between the predicted equilibrium shape and the experimental topographic features of the nanoisland is excellent, thus confirming the attainment of equilibrium shapes formed via dewetting.

2.4 Overview of FeRh self-assembly

Self-assembly of FeRh was thoroughly investigated on different substrates. The main observations and findings can be summarised as follows:

(i) Solid-state dewetting of FeRh films on MgO(001), MgO(011) and Al_2O_3(0001) substrates proceeds in anisotropic fashion depending on the epitaxial relationships.

(ii) The degree of dewetting depends on parameters such as film thickness, presence of hole nucleation sites on the substrate (e.g. defects) and temperature. In this way, sample fabrication was optimized such that well-separated islands with variable size and spacing could be obtained on the aforementioned substrates. A brief size distribution analysis of well-separated islands can be found in Appendix A.

(iii) Upon reducing nominal thickness of the samples, a percolation limit was found around 10–12 nm. Below this threshold, a continuous film could not be formed during growth, such that nanoislands assembled via Volmer–Weber growth instead of dewetting.

(iv) The morphology of the islands can be satisfactorily described by the Winterbottom construction upon assuming the adequate epitaxial relations.

(v) It was found that FeRh grows on MgO(011) with a high-index (112) texture. Solid-state dewetting leads to elongated islands with their long axis oriented in the high epitaxial mismatch direction. The missing value of the FeRh(112) surface energy can be estimated by matching the experimentally determined island topography to the Winterbottom construction.

3 Magnetic properties of FeRh islands

This chapter discusses the magnetic ordering of selected samples grown on MgO(001), MgO(011) and Al_2O_3(0001). Initially, their collective magnetic behavior in conjuction with their morphological features is studied by a combination of experimental techniques and modeling, ensued by the analysis of the metamagnetic transition in separated islands.

3.1 Phase transition characteristics of nanoisland ensembles

As for experimental techniques, magnetic ordering of specimens featuring island-like morphology was investigated primarily via magnetic force microscopy (MFM) and vibrating sample magnetometry (VSM). In addition, we model the prevailing AF or FM ordering by simulating the equilibrium shapes of FeRh crystallites at different magnetic phases.

MFM was extensively used to investigate the magnetic ordering of FeRh nanoisland systems. This is a two-pass mode derived from AFM, which provides the separate acquisition of topographic structure and magnetic force gradient distribution.[1] Here, in order to ensure a preferential magnetization direction during MFM measurements, a permanent magnet, exhibiting a stray field of 0.25 T in the out-of-plane direction, was located below the measured sample. Subsequently, the recorded MFM images were represented in the program *Gwyddion 2.50*. Spatially resolved magnetic ordering can be understood based on the relative contrast levels in the MFM images, associated with the phase shifts of the cantilever oscillations.

At first, we present AFM and corresponding MFM images acquired at room temperature for samples grown on MgO(001) (see Figure 3.1). A MFM measurement on sample M(001)-16c of a worm-like structure with well-recognizable dewetted features (see Figure 3.1a) reveals only three regions disrupting otherwise prevailing zero contrast background (represented by the green color in Figure 3.1b). The majority fraction of dewetted structures, associated with a zero value of the phase shift, thus manifests no magnetic signal in the MFM image and hence we hypothesize that the vast majority of islands may presumably show AF ordering. The remaining distinguished regions, corresponding to the FM ordering of three particular islands, display significantly negative phase shifts over the entire nanoisland area. In addition, the magnetization of the islands showing a prominent MFM contrast seems to be oriented along the out-of-plane direction, well aligned with the external magnetic field. This observation is in good agreement with preferential out-of-plane magnetocrystalline anisotropy, predicted for FeRh on MgO in its FM state [71].

Next, the MFM measurement perfomed on sample M(001)-16d shows similar features when compared to the previously analyzed sample, but the fraction of those islands showing a noticeable MFM contrast is different (see Figure 3.1d). While half of the well-separated but slightly smaller (300–500 nm) islands (see Figure 3.1c) exhibit AF ordering, the remaining half reveal FM ordering with an out-of-plane magnetization direction. The ratio of FM to AF island population is even larger for sample M(001)-16b, containing distant, sub-400-nm nanoislands (see Figure 3.1e) that are predominantly out-of-plane magnetized (see Figure 3.1f). Considering the MFM images for self-assembled morphologies of samples M(001)-16b–d, one could conclude that while worm-like structures formed

[1] A detailed description of MFM technique was given in the Bachelor's thesis of the author [63].

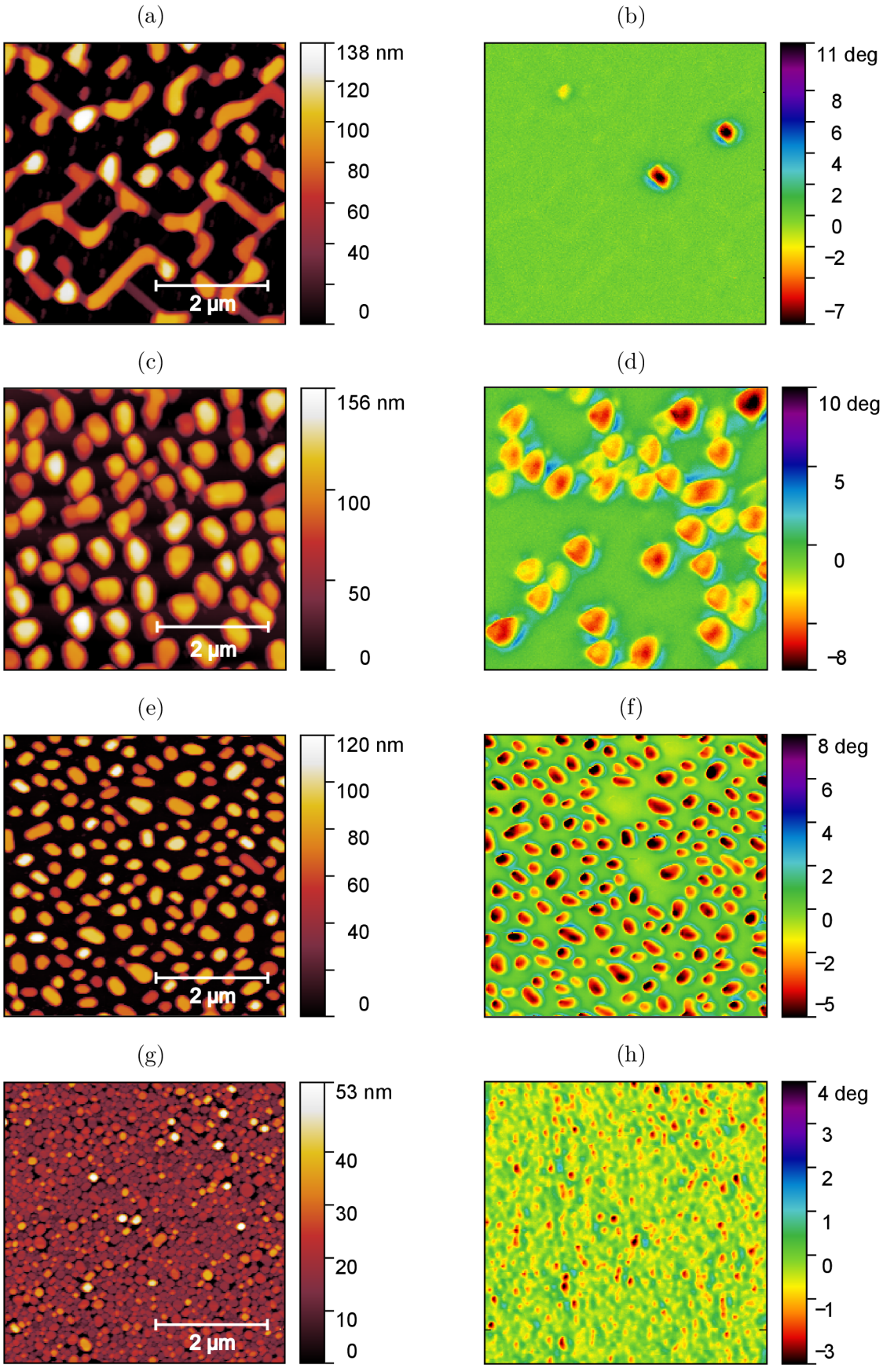

Figure 3.1: AFM (left panel) and MFM (right panel) images for samples grown on MgO(001): (a)–(b) sample M(001)-16c; (c)–(d) sample M(001)-16d; (e)–(f) sample M(001)-16b; (g)–(h) sample M(001)-12b.

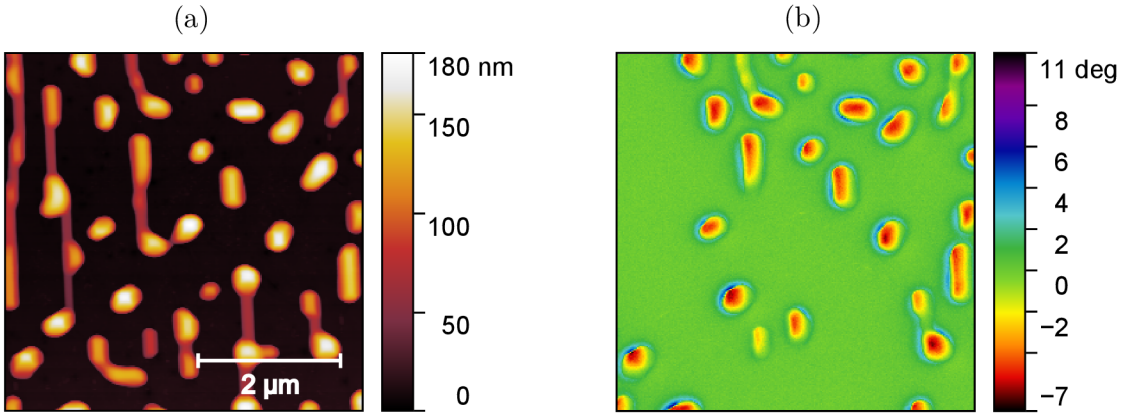

Figure 3.2: (a) AFM and (b) MFM image for sample M(011)-16 grown on MgO(011).

via dewetting are essentially in the AF state at room temperature, the smaller the islands are, the larger population of them display a clear FM ordering.

Additionally, we analysed sample M(001)-12b consisting of sub-200-nm adjoining islands, which were assembled via nucleation (Volmer–Weber growth) instead of via solid-state dewetting (see Figure 3.1g). Here, the vast majority of nanoislands reveal either a positive or negative MFM phase shift over their entire area (see Figure 3.1h), therefore exhibiting a largely stabilized FM ordering at room temperature.

We also present a MFM measurement of sample M(011)-16 grown on MgO(011), revealing an out-of-plane magnetization from about half of the island population, while a negligible MFM magnetic signal is perceived in the remaining part (see Figure 3.2).

Finally, a similar phenomenon as for samples grown on MgO(001) can be observed for samples grown on Al_2O_3(0001) (see Figure 3.3). On one hand, sub-micron sized islands formed via dewetting from a nominally 16-nm-thick FeRh film (see sample A(0001)-16 in Figure 3.3a) show both populations with a MFM signal indicating out-of-plane oriented magnetization or no signal at all (see Figure 3.3b). On the other hand, islands assembled from a nominally 12-nm-thick FeRh film, which display slightly smaller island sizes (< 200 nm) (see sample A(0001)-12 in Figure 3.3c), are FM stabilized at room temperature (see Figure 3.3d).

In order to quantify the fraction of islands in each sample that are FM stabilized at room temperature, as well as to prove that the islands showing no MFM signal are AF (by verifying the presence of the AF-to-FM phase transition), one needs to study their temperature-dependent magnetic properties. This is firstly done via VSM which enables measurements of the volume-averaged magnetic moment of a sample as a function of temperature or magnetic field [72]. The VSM measurements presented in this thesis were performed using a VersaLab magnetometer from Quantum Design which is a cryogen-free system enabling measurements in the temperature range of 50–400 K and under maximum fields of 3 T [73]. The instrument operates at 40 Hz with typical sample oscillation amplitudes of 2 mm between the pick-up coils. By employing an averaging time of 1 second per data point, the magnetometer allows sensitivity down to 1 µemu or 10^{-9} A m^2.

Here, we initially present temperature-dependent VSM measurements of selected samples grown on MgO(001). The overall magnetic moment was measured either continuously during a temperature decrease from 400 K to 55 K followed by a ramp back to 400 K or after temperature stabilization at specific temperature steps defined in the same range. The measurements were done in the presence of a constant in-plane magnetic field (1 T)

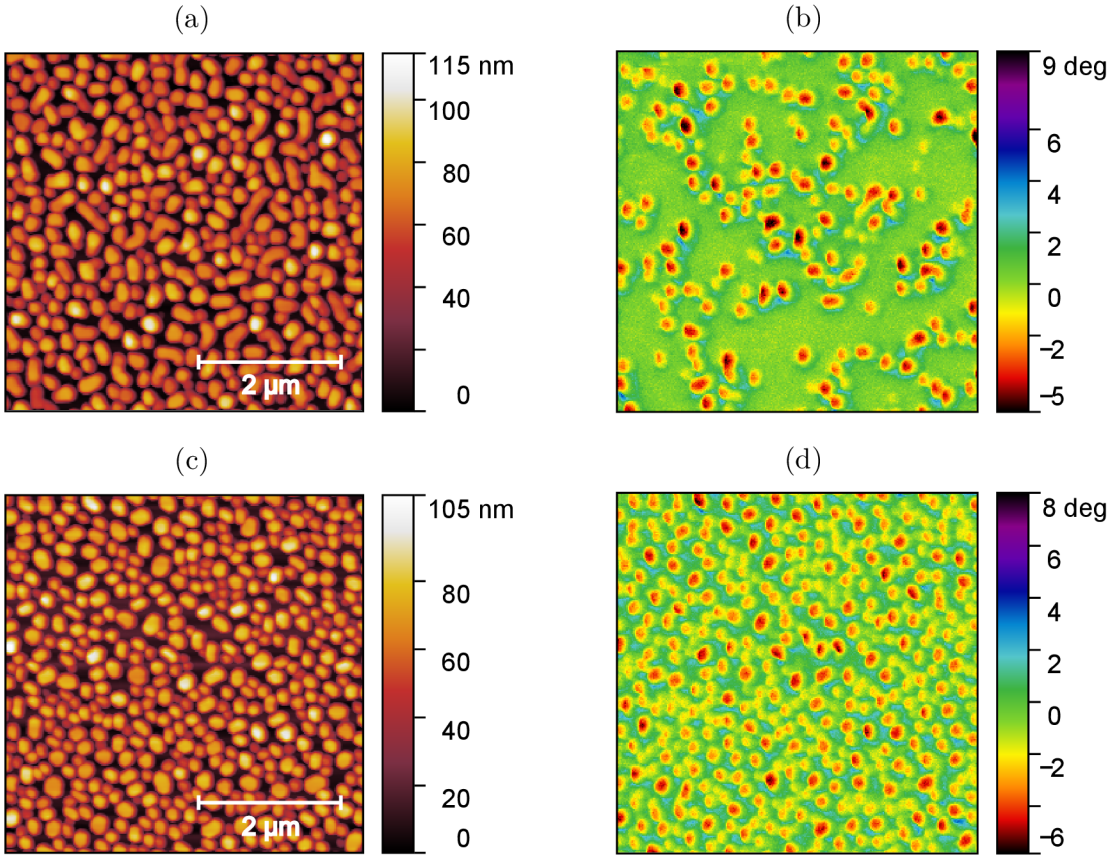

Figure 3.3: AFM (left panel) and MFM (right panel) images for samples grown on Al_2O_3(0001): (a)–(b) sample A(0001)-16; (c)–(d) sample A(0001)-12.

to align the constituent magnetic moments in one direction. The vertical curve shift caused by the applied field was corrected to account for the diamagnetic contribution of the substrate. Based on the corresponding nominal thickness and substrate dimensions, the measured overall magnetic moment of particular samples was thereafter converted to the magnetization and plotted vs temperature in Figure 3.4.

As a first step, we aim to compare the temperature-dependent magnetic behavior of islands obtained via solid-state dewetting with islands nucleated within the Volmer–Weber growth mechanism upon depositions at very high temperature ($\sim 800\,^{\circ}$C). The latter show a very broad thermal hysteresis with only a minor fraction of the islands reaching the AF phase but with a large retained magnetization persisting at temperatures as low as 50 K (see Figure 3.4f and the corresponding AFM picture marked in purple below). This result is in accordance with the reported works [58].

The first VSM measurements of films grown at much lower temperatures ($\sim 460\,^{\circ}$C) prior to high-temperature annealing were performed on maze-like islands of samples M(001)-20 and M(001)-16c. Opposite to the islands formed via Volmer–Weber mechanism, both samples formed via dewetting contain a large portion of islands undergoing the metamagnetic transition (see Figure 3.4a–b).

While these samples exhibit an abrupt AF-to-FM transition upon heating, a behavior comparable to the one of a continuous FeRh film (see Figure 1.10), the cooling branches are substantially broader, reaching a low residual FM fraction at 100 K. The asymmetry between the heating and cooling branches, with a sharp transition during heating and a very broad transition during cooling, is even enlarged for sample M(001)-16d, leading to an

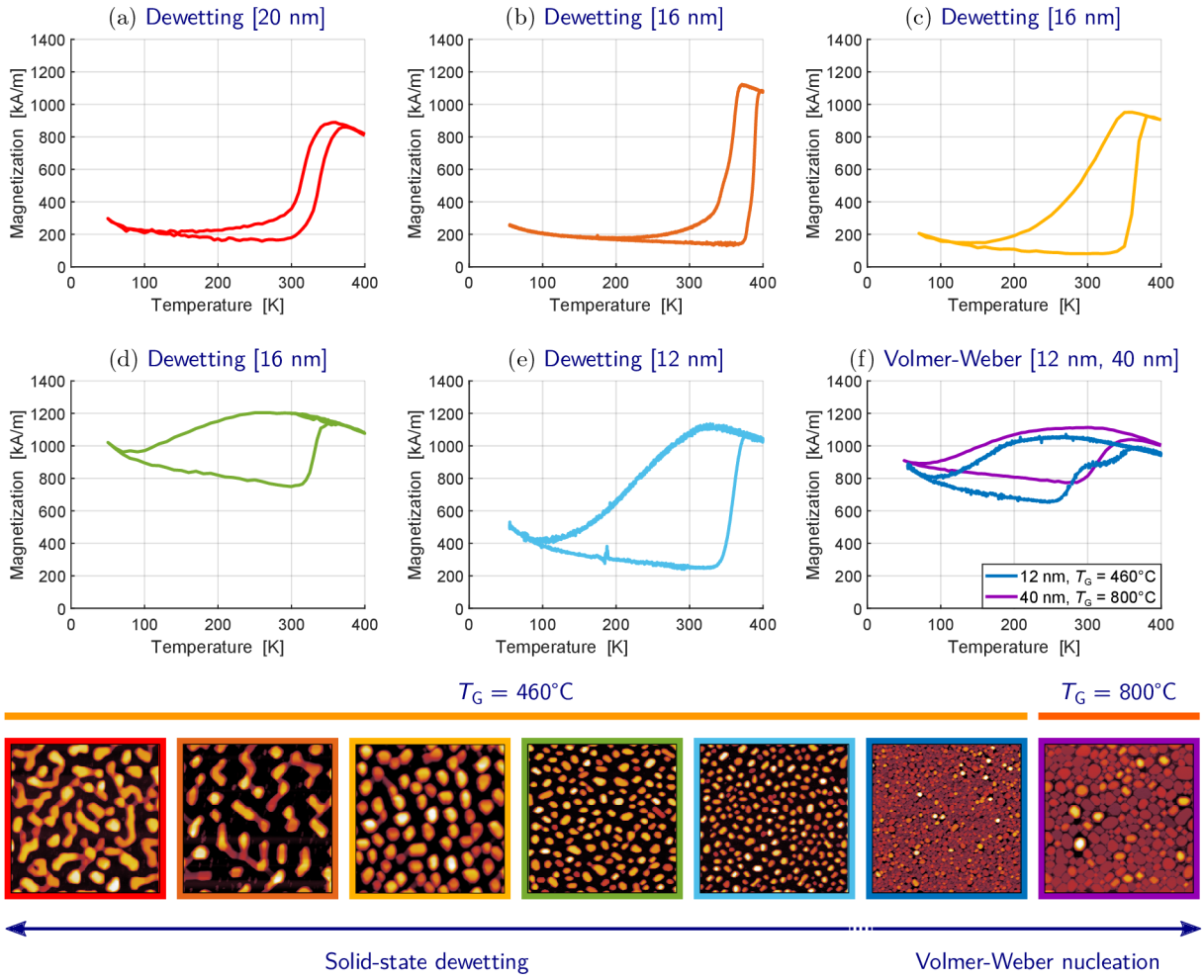

Figure 3.4: Temperature-dependent VSM measurements for samples: (a) M(001)-20; (b) M(001)-16c; (c) M(001)-16d; (d) M(001)-16b; (e) M(001)-12a; (f) M(001)-12b, all grown on MgO(001) at 460 °C; (f) for a sample grown on MgO(001) through Volmer–Weber mechanism during deposition at 800 °C. AFM images of particular samples, marked in colors corresponding to the VSM curves, are shown in the bottom part.

extensive increase in the thermal hysteresis width (see Figure 3.4c). Since all our samples were cooled to room temperature ($\sim 300\,\mathrm{K}$) after the post-growth high-temperature annealing, we assign the state corresponding to the MFM measurements shown in Figure 3.1 to the magnetization reached for room temperature in the cooling branches in Figure 3.4. Accordingly, considering the large difference in magnetization of sample M(001)-16d at room temperature between the cooling ($\sim 600\,\mathrm{kA/M}$) and heating ($\sim 80\,\mathrm{kA/M}$) directions, we expect a much lower portion of islands to exhibit FM ordering compared to Figure 3.1d if cooled down to 100 K. This aspect will be thoroughly discussed in Section 3.4.

Thus, we observe that islands that are obtained via solid-state dewetting largely conserve their metamagnetic properties, which allows us to safely assign AF ordering to those islands that did not display any noticeable MFM signal in the experiments presented earlier in this section. However, when studying the samples with smaller island sizes that are also formed via solid-state dewetting, a slightly different scenario was found. Despite being grown under the same deposition conditions as samples M(001)-16c and M(001)-16d, sample M(001)-16b posseses a large portion of FM stabilized islands even at very low temperatures (see Figure 3.4d). The thermal hysteresis is wide but flat, with a large area

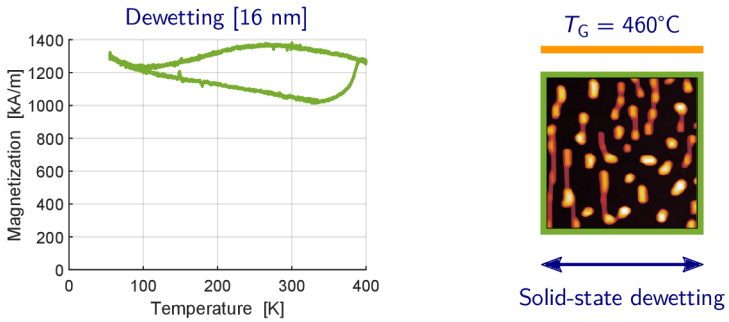

Figure 3.5: Temperature-dependent VSM measurement for sample M(011)-16 grown on MgO(011), measured in the presence of a constant in-plane magnetic field parallel to the direction of island elongation (direction FeRh[11$\bar{1}$]). AFM image of the sample is shown on the right.

enclosed by the loop. The slope of the heating branch is negative up to ∼320 K, then ensued by an abrupt magnetization increase corresponding to a fraction of the islands that preserve metamagnetism and thus undergo the AF-to-FM transition. Here, we see that a reduction of island size down to 100–200 nm may lead to the FM stabilization even at temperatures as low as 55 K.

However, the reduced island size alone cannot explain the FM stabilization observed for sample M(001)-16b. In fact, sample M(001)-12a with a nominal thickness of 12 nm features even smaller islands (around 200 nm) but instead a very large fraction of the sample undergoes the phase transition as evidenced by the data in Figure 3.4e (see also AFM picture marked in light blue). Conversely, the additional 12-nm-thick sample M(001)-12b that was self-assembled via Volmer–Weber nucleation exhibits a shallow thermal hysteresis with a large majority of islands maintaining FM ordering even at low temperatures (see Figure 3.4e). Therefore, we find a striking similarity with the temperature-dependent magnetization loop of the sample considered to have grown via Volmer–Weber mechanism at high temperatures (see Figure 3.4f).

Next, sample M(011)-16 grown on MgO(011) was analyzed via temperature dependent VSM measurements as well (see Figure 3.5). The sample posseses a large value of magnetization down to very low temperatures. This FM stabilization can come from the enormous misfit of the FeRh lattice with the substrate (∼13%) resulting in a large tensile strain along one in-plane direction (see Figure 2.13b) that promotes the FM state with a larger lattice parameter. However, the sample contains also a perceivable fraction (30%) of metamagnetic islands.

Finally, we present temperature-dependent VSM measurements of samples deposited onto Al_2O_3(0001). Sample A(0001)-16, containing well-separated epitaxial islands, shows a broad thermal hysteresis loop with a low residual FM fraction and high saturation magnetization (see Figure 3.6a), comparable to the saturation of continuous FeRh films. Except the higher achieved saturation magnetization value, the asymmetric shape of the loop looks similar to the thermal hysteresis of sample M(001)-16d grown on MgO, featuring a sharp AF-to-FM transition upon heating and broad FM-to-AF transition upon cooling.

The temperature-dependent magnetic behavior for sample A(0001)-12 with a reduced FeRh nominal thickness contrasts with the well-pronounced thermal hysteresis of the effectively thicker sample A(0001)-16. Instead, here we observe a typical FM behavior,

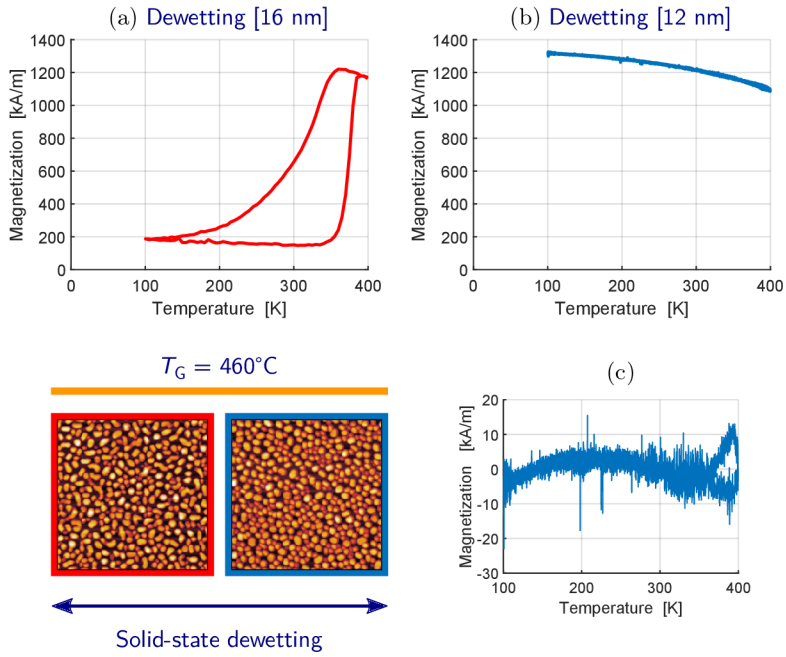

Figure 3.6: Temperature-dependent VSM measurements for samples grown on $Al_2O_3(0001)$: (a) sample A(0001)-16; (b) sample A(0001)-12; (c) a little portion of metamagnetic islands of sample A(0001)-12. AFM images of particular samples, marked in colors corresponding to the VSM curves, are shown in the bottom-left panel.

manifesting itself by a decreasing magnetization upon heating (see Figure 3.6b). This dependence of magnetization M on temperature T was fitted by the power law equation [18]

$$M = M_s \cdot \left(1 - \frac{T}{T_C}\right)^b \tag{3.1}$$

where T_C corresponds to the Curie temperature, M_s corresponds to the saturation magnetization and b is a constant. In our case, $M_s = 1357\,\mathrm{kA/m}$, $T_C = 453\,\mathrm{K}$ and $b = 0.1$. Thereafter, the fitted curve was substracted from the real data, which revealed a very little fraction of particles undergoing the metamagnetic transition (see Figure 3.6c).

Besides MFM and VSM measurements, we show a complementary analysis that could predict the prevailing AF or FM ordering of the supported FeRh islands. This is based on the topographic inspection of crystallographic facets. It has been theoretically predicted that the different magnetic ordering (AF vs FM) leads to different surface energies for the principal facets of FeRh crystallites, primarily for FeRh(001), (011) and (111) planes. The specific values for AF and FM phases of bulk equiatomic FeRh at 0 K, calculated by Liu and coworkers [59], are listed in Table 3.1. Considering these values, we determined the Winterbottom constructions for AF and FM stabilized FeRh islands on MgO(001) and $Al_2O_3(0001)$ (see Figures 3.7 and 3.8).

We initially see that the FeRh(011) facets are favored for the equilibrium AF shape (see Table 3.1), leading to rather globular Winterbottom construction on MgO(001) (see the Winterbottom constructions in Figure 3.7a). In contrast, the equilibrium FM shape possesses large square (001) facets and resembles a truncated cube (see the Winterbottom constructions in Figure 3.7b), since the value of surface energy for FM (001) facets is considerably lower compared to the one for FM (011) facets (see Table 3.1). Remarkably, the different equilibrium shapes predicted for AF or FM ordering are supported by the

FeRh plane	AF phase [J/m^2]	FM phase [J/m^2]
(001)	2.274	1.775
(011)	2.090	1.876
(111)	2.431	2.082

Table 3.1: Surface energies [J/m^2] for (001), (011) and (111) crystallographic planes in equiatomic bulk FeRh at $T = 0\,\mathrm{K}$ calculated by Liu *et al.* [59] and used for the Winterbottom constructions shown in Figures 3.7 and 3.8. Colors used for the particular surface energies in the Winterbottom constructions in Figures 3.7 and 3.8 are shown in the right panel.

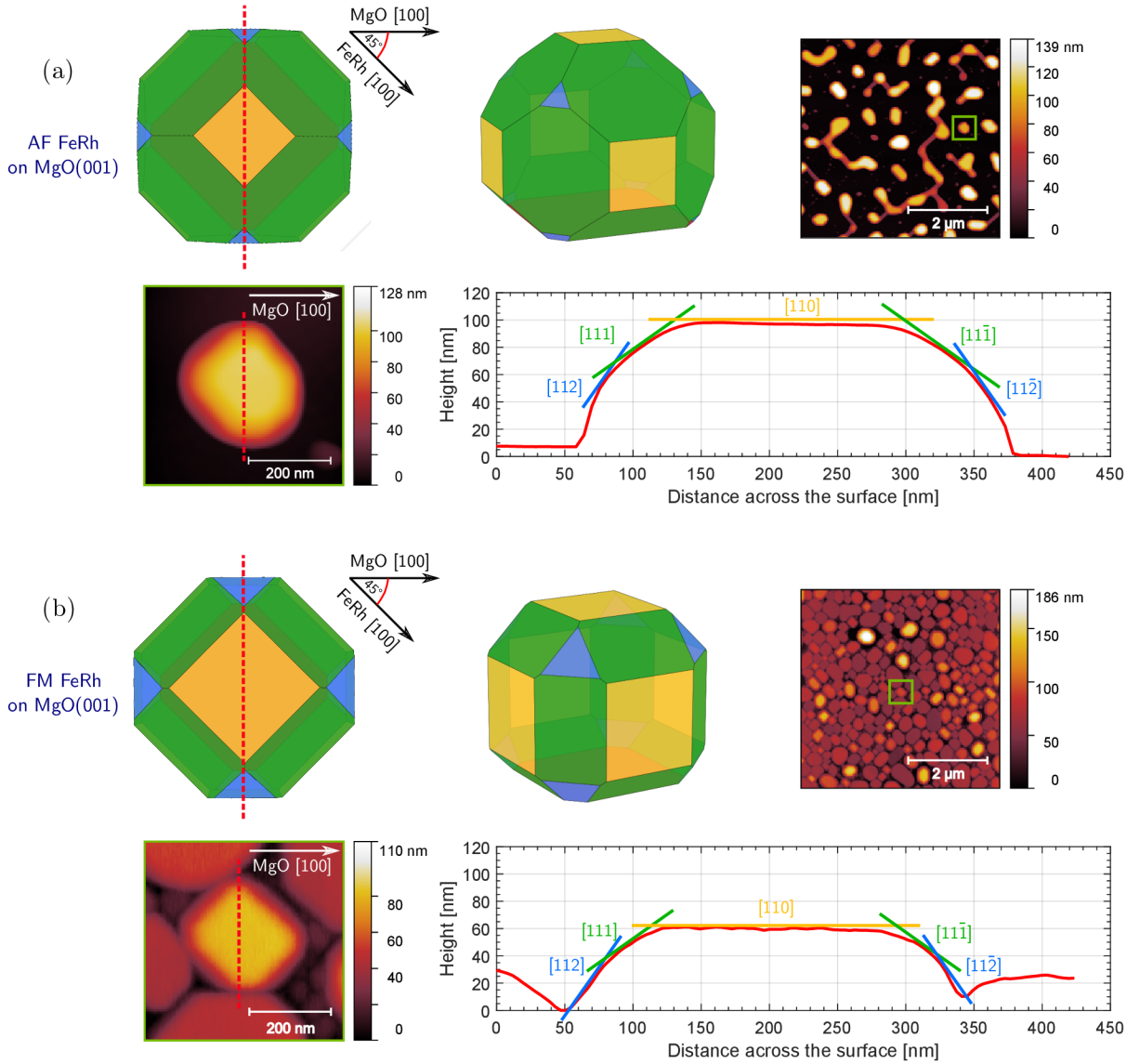

Figure 3.7: Nanoisland shape comparison between (a) AF FeRh on MgO(001) (sample M(001)-16c) and (b) FM FeRh on MgO(001) (sample grown through Volmer–Weber mode). For both, we show the corresponding Winterbottom constructions, 5×5 mm^2 AFM images, the detailed high-resolution acquisitions of a selected island, as well as the height profiles acquired along the red dashed lines in the high-resolution images and matched with the theoretical directions described by the Miller indices.

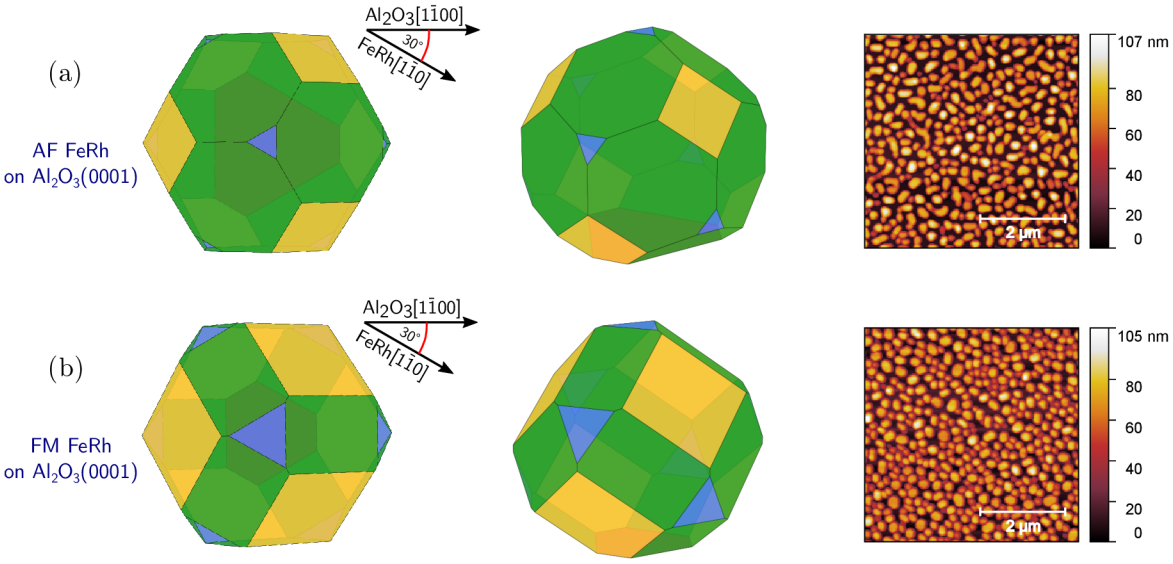

Figure 3.8: Winterbottom constructions (left panel) and AFM images (right panel) for: (a) AF FeRh on $Al_2O_3(0001)$; (b) FM FeRh on $Al_2O_3(0001)$.

topographic features of our samples. We indeed observe distinct shapes of islands formed via dewetting on sample M(001)-16c and islands grown via Volmer–Weber nucleation on MgO(001), the former containing more rounded islands and the latter featuring rather regular square shapes from the top view (compare the AFM images in Figure 3.7a–b). In order to perform a more detailed analysis, we additionally selected one room temperature AF stabilized island (see the island marked in green in the $5 \times 5\,\mu m^2$ AFM image in Figure 3.7a) and one FM stabilized island (see the island marked in green in the $5 \times 5\,\mu m^2$ AFM image in Figure 3.7b). We drew a red dashed line across the AF and FM Winterbottom representation as well as across the high-resolution experimental topography map of the selected AF island and FM island. The height profiles acquired along the red lines were then matched with the theoretical directions obtained from the Winterbottom construction. The height profiles reveal that both islands possess similar in-plane dimensions but different relative facet area ratios. In comparison to the AF island, the FM island features proportionally a larger relative area of the {001} planes (represented by the [110] direction in the height profiles) as well as larger area {111} planes (represented by the [112] and [11$\bar{2}$] directions in the height profiles), whereas it possesses a smaller relative area of the {011} planes (represented by the [111] and [11$\bar{1}$] directions in the height profiles), which is originated from the balance of surface energies in Table 3.1 and predicted via the Winterbottom construction. The comparison between experimental data and predicted Winterbottom construction for AF and FM ordered islands shows an excellent matching when the values in Table 3.1 are employed.

Concerning FeRh on $Al_2O_3(0001)$, the equilibrium shapes exhibit a three-fold in-plane symmetry (see the Winterbottom constructions in Figure 3.8c–d). The analysis of hexagonal shapes of AF FeRh was presented in Section 2.2. Here, we show that FM FeRh on $Al_2O_3(0001)$ should also reveal a hexagonal symmetry, but with more pronounced {001} planes, resulting in a more rounded shape. However, our experimental data did not allow to clearly distinguish the more subtle morphology differences that are predicted by the Winterbottom construction upon having FeRh(111) oriented islands.

3.2 Magnetic anisotropy

Magnetic anisotropy is the coupling of the magnetic properties (such as the magnetization) to particular directions at a local or a macroscopic level of a material. As for thin films, the origin generally consists in magnetocrystalline, shape or magnetoelastic contribution [74]. The magnetocrystalline anisotropy is related to the spin-orbit interactions and strongly depends on the ordering of the crystal lattice. The shape anisotropy reflects the effect of long-range dipolar interaction in a FM material, which are responsible for the generation of stray fields. The magnetoelastic anisotropy originates from strain induced modifications of magnetic anisotropy, which are especially prominent in epitaxial thin films due to the lattice misfit with the underlying substrate.

For the purpose of examining the magnetic anisotropy in islands formed via dewetting, we performed field-dependent VSM measurements at various temperatures. In order to additionally study the substrate influence, we selected sample M(001)-16d grown on MgO(001) and sample A(0001)-16 on Al_2O_3(0001) because of their morphology showing well-separated islands (see Figure 3.9f and Figure 3.10f) and the similar asymmetric shape of a thermal hysteresis. The VSM data were collected during field cycles between 2 T and −2 T for the in-plane and out-of-plane orientation of magnetic field relative to the sample surface (see Figure 3.9f and Figure 3.10f). The measurements were successively performed at 400 K, when the samples were completely in the FM state, at 300 K, when the magnetization dropped approximately to the half of the saturation magnetization achieved at 400 K, and at 60 K, when we found only a little residual FM phase. All presented magnetic loops were corrected for their diamagnetic contribution by subtracting the slope obtained at high fields, when the sample magnetization is already saturated. The field-dependent in-plane and out-of-plane hysteresis loops for sample M(001)-16d are shown in Figure 3.9 and the same VSM measurements for sample A(0001)-16 are displayed in Figure 3.10.

The typical hard-axis out-of-plane loops compared with the more straightened in-plane loops at 400 K and at 300 K indicate a preferential in-plane magnetic anisotropy of both FeRh systems at 400 K and 300 K (see Figure 3.9a,c and Figure 3.10a,c). We interpret this result in terms of the dominating shape anisotropy, which in the case of thin films (or nanoislands with thin film platelet shape) tends to align the magnetization vector into the film plane. However, all in-plane easy-axis loops are characterized by relatively small values of the remanence as revealed in Figure 3.9b,d and in Figure 3.10b,d. It is however worth mentioning that the out-of-plane magnetic field of 0.25 T, used during MFM measurements, is sufficient to ensure a significant out-of-plane magnetization alignment.

At 60 K, the in-plane and out-of-plane field hysteresis loops are less distinguishable (see Figure 3.9e and Figure 3.10e). While sample A(0001)-16 still features a preferential in-plane magnetic anisotropy, sample M(001)-16d reveals a slight preferential out-of-plane magnetization. We assign this phenomenon to the prevailing contribution of the magnetoelastic anisotropy of the remanent FM phase [74, 75]. As for FeRh on Al_2O_3(0001), the in-plane unit cell is expanded due to epitaxial mismatch, thus leading to an out-of-plane compressive strain. This positive in-plane misfit promotes an in-plane magnetoelastic anisotropy for the remanent FM phase at 60 K. In contrast, the FeRh lateral lattice parameter has to be compressively strained to match the MgO(001) substrate which provides the magnetoelastic effect with the magnetic easy axis being out-of-plane. We note that several works [71, 76] explain the anisotropy caused by the lattice mismatch in terms of the magnetocrystalline contribution, which causes a spin reorientation transition upon inverse tetragonal distortions. This is in contrast to the typical cubic anisotropy observed in unstrained bulk crystals.

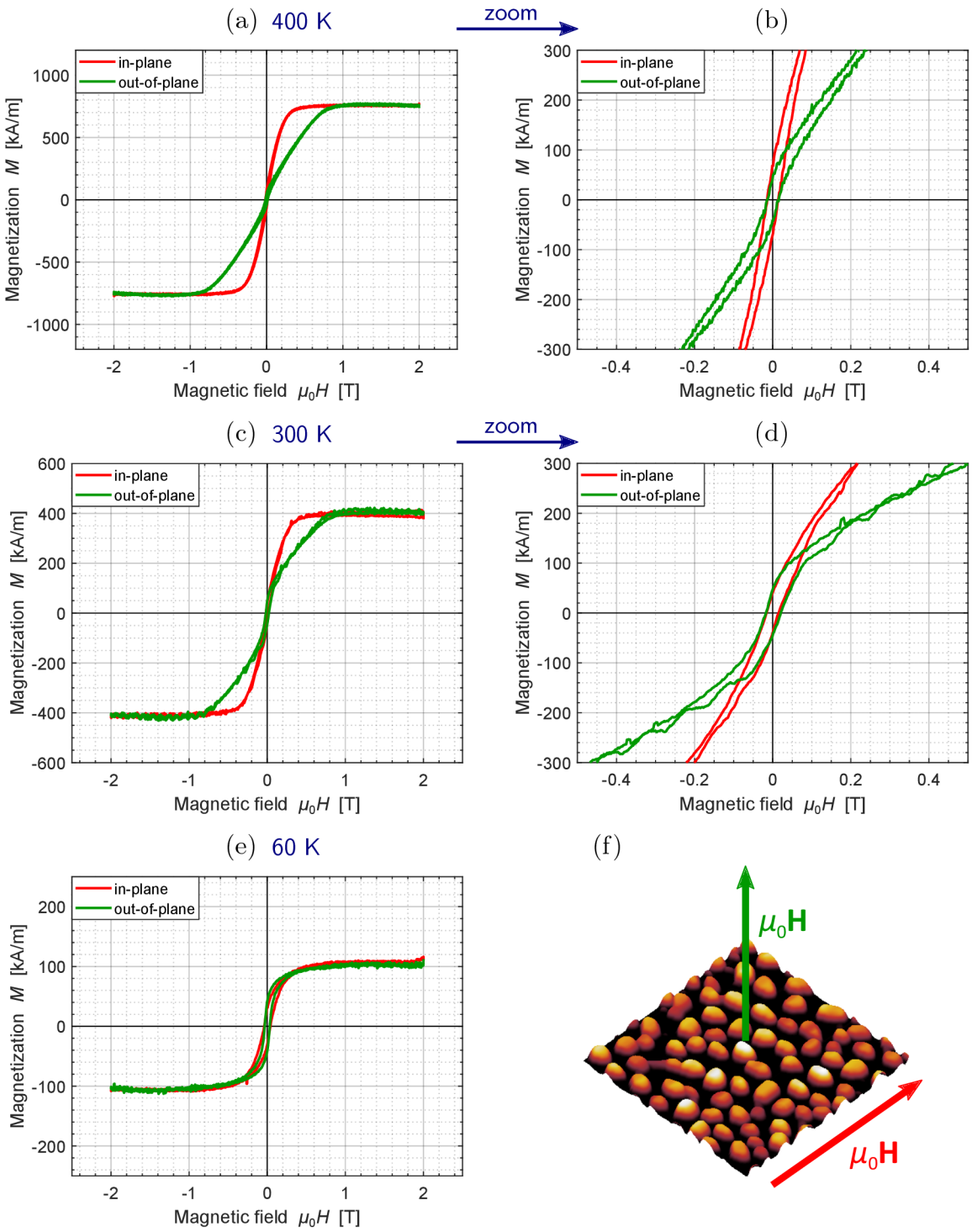

Figure 3.9: Field-dependent in-plane and out-of-plane VSM measurements for sample M(001)-16d: (a)–(b) at 400 K; (c)–(d) at 300 K; (e) at 60 K. The plots in the right panel represent detailed views of magnetic loops at the origin displayed in the left panel. For an easier comparison with the field loops of sample A(0001)-16, the plots in the left panel are displayed at the same scale as in Figure 3.10. 3D AFM micrograph of a $5 \times 5\,\mu m^2$ region in sample M(001)-16d with marked in-plane and out-of-plane magnetic field directions is shown in (f).

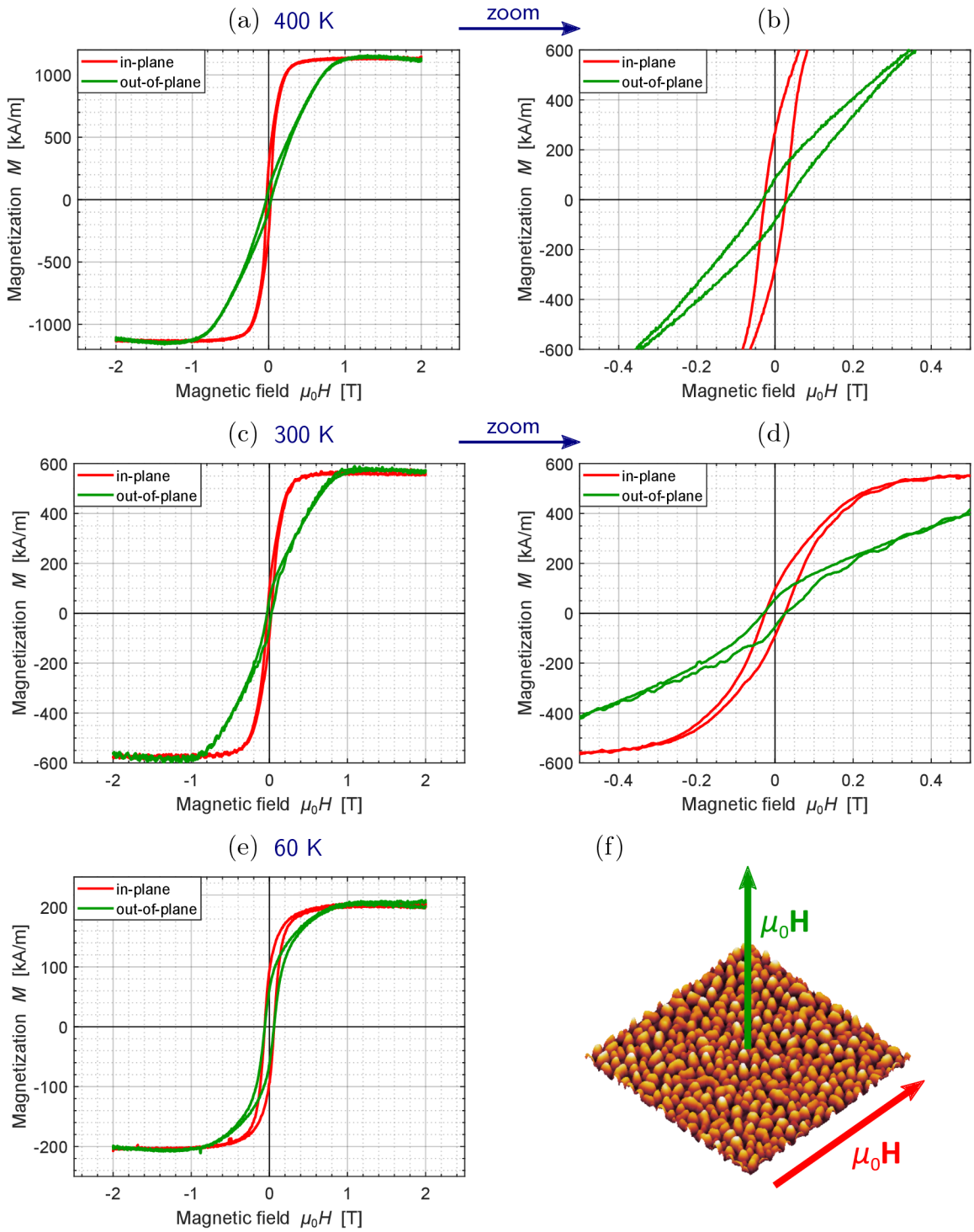

Figure 3.10: Field-dependent in-plane and out-of-plane VSM measurements for sample A(0001)-16 (AFM image shown in the bottom-right corner): (a)–(b) at 400 K; (c)–(d) at 300 K; (e) at 60 K. The plots in the right panel represent detailed views of magnetic loops at the origin displayed in the left panel. 3D AFM micrograph of a $5 \times 5\ \mu m^2$ region in sample A(0001)-16 with marked in-plane and out-of-plane magnetic field directions is shown in (f).

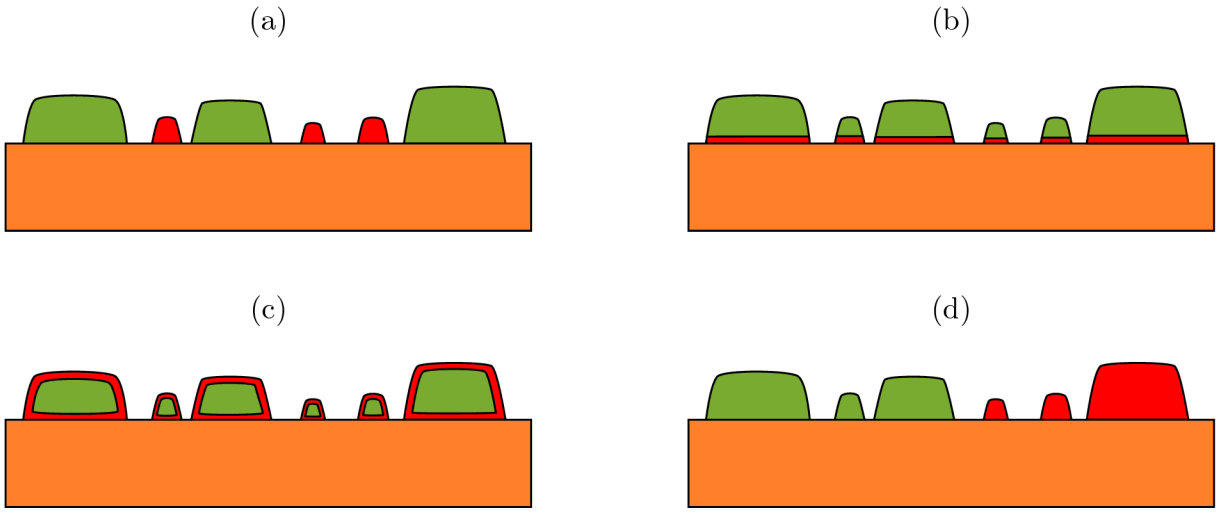

Figure 3.11: Possible scenarios bringing remanent FM phase (red - FM phase, green - AF phase, orange - substrate): (a) FM stabilization upon island size reduction; (b) interfacial FM layer; (c) interfacial and surface FM layer; (d) incorrectly ordered regions of FeRh.

For the occurrence of the remanent FM phase at temperatures as low as 60 K, we offer the following hypotheses:

(i) Island size reduction down to approximately 100 nm could lead to FM stabilization, similarly as it was seen for sample M(001)-16b. Accordingly, bigger islands on samples M(001)-16d and A(0001)-16 could exhibit metamagnetic behavior, while smaller islands could exhibit FM ordering over entire temperature range (see Figure 3.11a).

(ii) The remanent magnetic moment could arise from the existence of a FM stabilized ultrathin layer at the interface with the substrate (see Figure 3.11b). Such a stable interfacial FM layer has been already observed in the case of continuous, lattice-constrained FeRh films [77].

(iii) All islands could posses FM stabilized regions not only at the interface with the underlying substrate, but also over the entire surface area (see Figure 3.11c). In fact, Liu and coworkers [59] have shown that the lowest surface energy for AF FeRh crystallites occurs when considering FM surface termination.

(iv) Uneven FeRh deposition effects across the entire substrate could have resulted in a film containing regions where the well-ordered CsCl-like structure was not obtained. This effect could lead to FM stabilized islands (see Figure 3.11d).

However, the occurrence of the remanent FM phase at temperatures as low as 60 K does not exclude that sub-micron FeRh particles could not be completely AF at room temperature. In fact, Ohtani and Hatakeyama [78] reported about a change in magnetic behavior of an FeRh film once peeled from the substrate. On a quartz substrate, the film was exerted to tensile in-plane strain (see Figure 3.12b) and its thermal hysteresis revealed remanent magnetization of $\sim 200\,\mathrm{kA/m}$ (see the purple curve in Figure 3.12a). The film peeling caused a distinct change in thermal hysteresis, exhibiting a significantly steeper transition with an increased transition temperature of $\sim 50\,\mathrm{K}$ (see the green curve in Figure 3.12a). Most importantly, the peeling lead to the suppression of the remanent FM phase which is understood in terms of a relaxation in the lattice spacing (see Figure 3.12c). Consequently, as for our FeRh islands, it would be interesting to test if the remanent magnetization stays or is suppressed as well when released from the substrate.

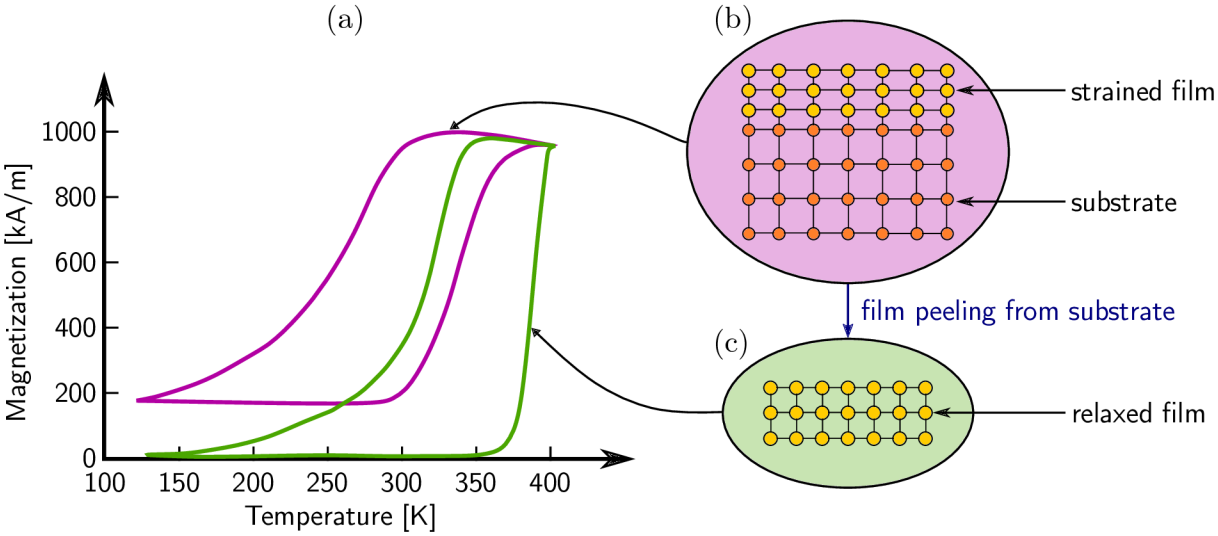

Figure 3.12: Experiment performed by Ohtani and Hatakeyama [78]: (a) schematic representation of thermal hysteresis for a lattice-constrained FeRh film (purple curve) and for a relaxed film after peeling from the substrate (green curve); (b) schematics of the strained film; (c) schematics of the relaxed film.

In addition to VSM measurements, we attempted to employ the magneto-optical Kerr effect (MOKE) combined with a wide-field optical microscope for the purpose of visualizing the phase transition over length scales of several tens of microns. The MOKE microscopy technique is based on the change in the polarization state of incident light after undergoing reflection from a magnetic material and allows resolving differently magnetized objects down to a resolution of about $\sim 500\,\mathrm{nm}$. However, due to insufficient available magnetic field in the system to reverse the magnetization ($0.3\,\mathrm{T}$ vs $\sim 1\,\mathrm{T}$) as well as because of the detrimental depolarization effects arising from light scattering on the edges of the islands, no relevant MOKE signal could be obtained from our FeRh islands.

3.3 Single-island metamagnetic behavior

In order to understand the asymmetric thermal hysteresis behavior shown in Figure 3.4 and in Figure 3.6a, one needs to investigate the behavior of individual islands across the metamagnetic transition. For this purpose, the current MFM system was equipped with a sample stage based on a series of Peltier modules enabling measurements from 280 K up to 370 K.[2] For this temperature-dependent study, we chose sample M(001)-16d with well-separated FeRh islands formed via dewetting. Initially, the AFM and the corresponding MFM image of a larger scan area ($8 \times 8\,\mu\mathrm{m}^2$) were recorded at room temperature, when approximately half of the nanomagnets exhibit FM ordering (see Figure 3.13a–b). Taking into account the thermal history of the sample, we assume that the magnetization state of the sample can be found on the cooling branch of the thermal hysteresis rather than on the heating branch, as the sample was cooled from 400 K to room temperature prior to the presented MFM study. After the measurement at room temperature, AFM and MFM data of the same area were successively collected at temperatures of 303 K, 313 K, 323 K, 333 K, 343 K, 348 K, 353 K, 358 K and 368 K (see Figure 3.13c–k). We observe

[2]The description of the sample stage can be found in the Bachelor's thesis of the author [63].

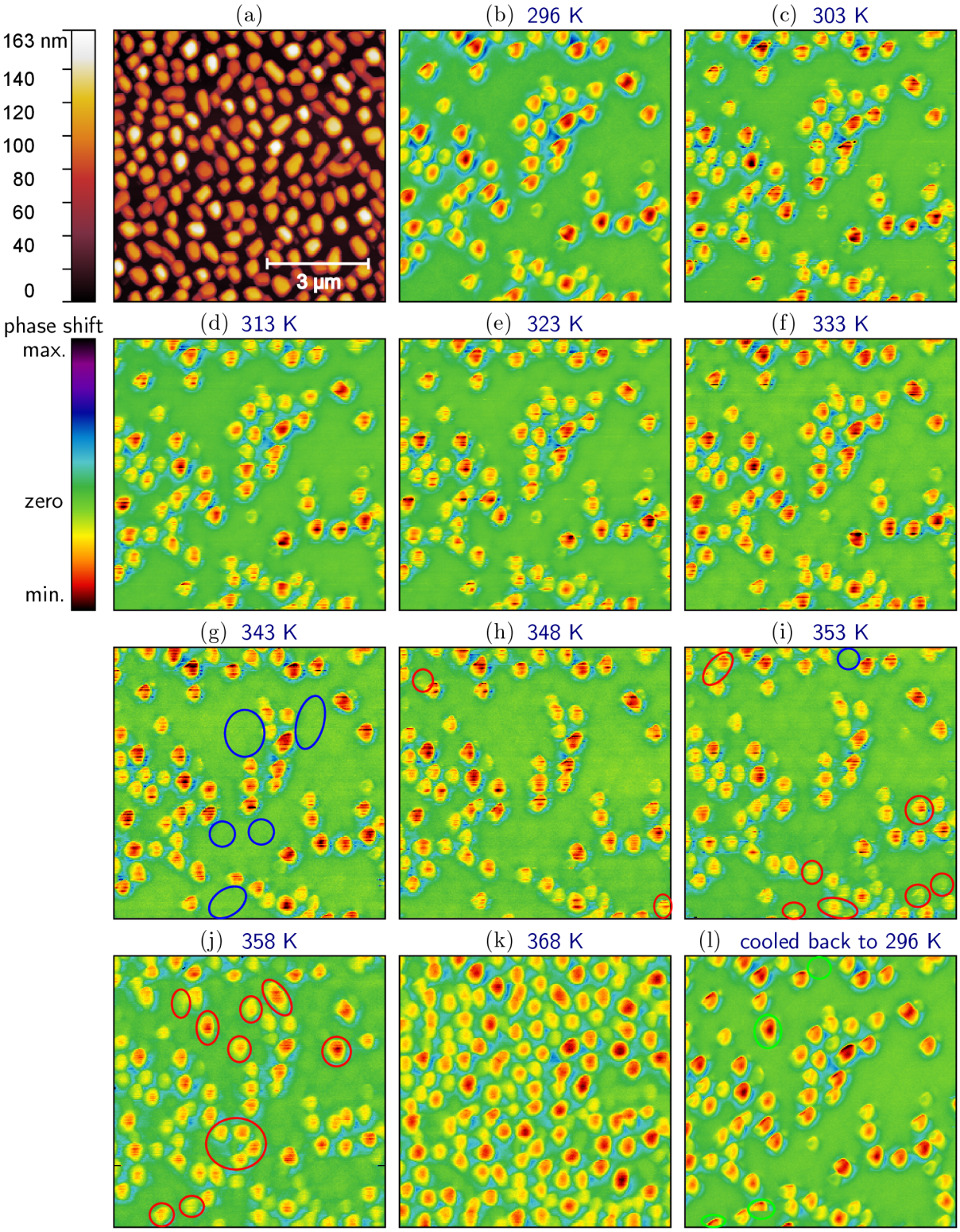

Figure 3.13: MFM measurement of sample M(001)-16d during heating: (a) AFM image at room temperature ($\sim$296 K); (b)–(k) MFM images during the heating cycle (from room temperature up to 368 K); (l) MFM image after cooling the system down back to room temperature. Blue and red circles indicate FeRh nanoislands that undergo the FM-to-AF and FM-to-AF phase transition upon heating, respectively. Green circles in (l) mark differences with (b).

that a large number of FeRh islands undergo the phase transition from AF to FM order upon heating in the narrow temperature range 348–368 K (see the red circles marking the new AF-to-FM transitions at particular temperatures relative to the zero magnetic signal in a preceding MFM image in Figure 3.13h–j and prevailing negative phase shifts in Figure 3.13k). In fact, essentially all islands seem to be FM already at 368 K. After almost all islands switched to FM ordering at the highest temperature, the sample was cooled back down to room temperature and an additional measurement was acquired (see Figure 3.13l), revealing similar magnetic configuration of islands as in Figure 3.13b.

In addition to the AF-to-FM transition, we see islands exhibiting FM order at room temperature that undergo an anomalous FM-to-AF phase transition upon heating (see the blue circles marking the FM-to-AF transitions in Figure 3.13g,i), which is however expected only upon cooling in case of FeRh. We have previously explained this behavior in terms of the supercooled states of the islands showing metastable FM ordering below the transition temperature [63]. Upon sufficient thermal activation, these islands gain energy to overcome the barrier separating the metastable FM state from the stable AF state and transition via an abrupt jump. The probability to overcome this energy barrier and to adopt the stable AF phase configuration substantially increases with temperature. However, upon further heating, AF ordering becomes metastable and the expected AF-to-FM phase transition takes place. In this way, we can observe both FM-to-AF and AF-to-FM transitions of the same island at a single branch of thermal hysteresis.

Comparing the MFM images at room temperatures before and after the performed experiment (see Figure 3.13b,l), we observe slightly different island arrangement in the FM state. We see one island in the AF phase, two islands revealing the FM ordering and one island just undergoing the FM-to-AF transition, all showing opposite behavior to the situation before the experiment (see the green circles indicating the differences in Figure 3.13l). This observation as well as the unexpected FM-to-AF transition upon heating, explained in the previous paragraph, suggest that all the other FM nanomagnets at room temperature possess also well-ordered FeRh lattice but stay in a metastable state. This could explain the futher decrease of the magnetization during cooling under the room temperature as revealed by the VSM measurement of sample M(001)-16d in Figure 3.4.

3.4 Extended supercooling in sub-micron islands

To investigate the degree of supercooling in FeRh nanomagnet arrays, one would need to perform MFM measurements well below the room temperature. As our sample stage incorporating Peltier cells allows cooling only in a limited temperature range (approximately down to 280 K), we instead followed the strategy of studying the thermal history dependence of sample M(001)-16d by applying different cooling/heating sequences upon which we examined the remanent magnetic state obtained at low temperature using MFM at room temperature.

The experiment consisted in performing minor thermal loops of sample M(001)-16d in the VSM chamber, enabling cooling down to temperatures as low as 100 K, in order to prepare the magnetic state for each MFM experiment. Prior to each MFM measurement, the sample was initially heated up to 400 K, to ensure the complete AF-to-FM transition and thus the same condition before each MFM measurement. Subsequently, the sample was cooled down to a specific temperature before each experiment (300 K, 250 K, 200 K, 150 K, 100 K and again 300 K) and heated back to 300 K where the MFM measurement was acquired (see the schematic of the heating and cooling sequences in Figure 3.14d).

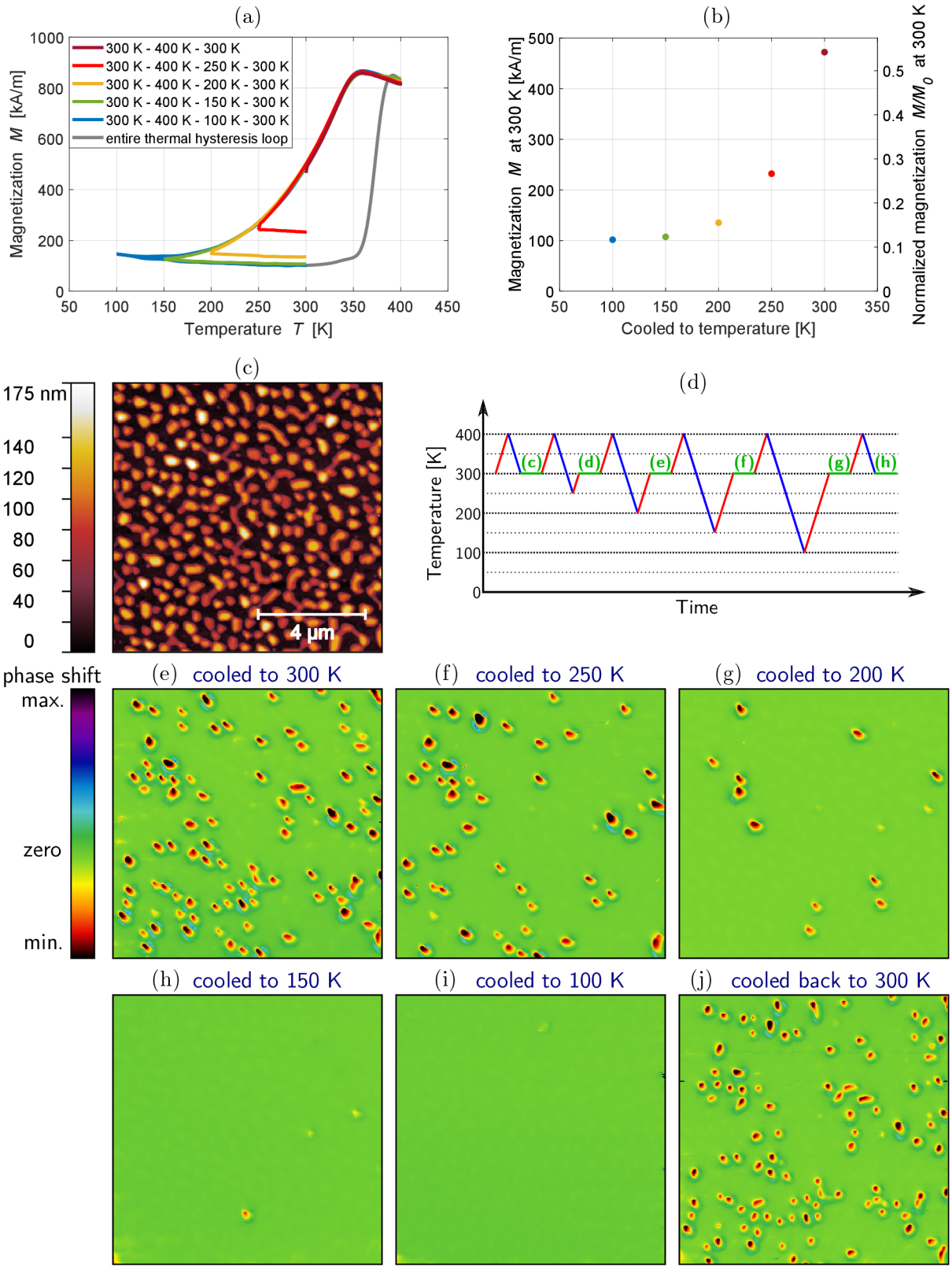

Figure 3.14: Demonstration of supercooling as large as 150 K in FeRh nanoislands of sample M(001)-16d: (a) parts of the performed minor loops comprising a cooling sequence from 400 K to a selected temperature; (b) magnetization values reached at 300 K upon heating for individual minor loops; (c) AFM image of the selected area; (d) schematic representation of the heating and cooling sequences followed to acquire the MFM images at room temperature (the green letters mark the condition of MFM measurements shown in (e)–(j)); (e)–(j) MFM images at room temperatures upon the temperature cycling.

We additionally show parts of the performed minor loops comprising a cooling sequence from 400 K to a selected temperature (300 K, 250 K, 200 K, 150 K or 100 K) followed by a heating sequence to 300 K (see Figure 3.14a). In order to better visualize the sample's magnetization history upon different thermal cycling sequences, the magnetization M vs temperature T curves were slightly smoothed using interpolating splines. The magnetization value reached at 300 K upon heating for each minor loop is plotted vs the minimum temperature of the corresponding curve in Figure 3.14b. Besides, we show the magnetization values at 300 K normalized with respect to the maximum magnetization M_0 (right y-axis in Figure 3.14b).

For this experiment, we selected a large scan area ($10 \times 10\,\mu m^2$), containing different shapes of islands formed via dewetting (see the topography in Figure 3.14c), and kept measuring the same region after different thermal sequences (see Figure 3.14e–j). We observe that the number of islands in the FM state is diminished upon sequentially cooling the sample to 300 K, 250 K, 200 K, 150 K and 100 K. We can thus confirm that all islands in the FM state at room temperature possess well-ordered FeRh lattice but remain in the supercooled metastable state. We additionally see that supercooling can extend over 150 K in nanosized FeRh islands. This is an extraordinary range of supercooling: for example, the lowest measured temperature of supercooled liquid water was $\sim$230 K [79], which is already $\sim$40 K below the freezing point. Here, smaller islands are more likely to remain in the metastable state over higher temperature range, containing less nucleation sites such as non-magnetic inclusions or AF clusters compared to bigger islands and wires, which are almost never found in the FM state at room temperature. The metastable FM state in smaller islands is thus more robust and can be stabilized well below room temperature.

3.5 Overview of FeRh nanoisland magnetic properties

After investigating the magnetic properties of FeRh island arrays as well as of individual islands, it can be concluded that:

(i) Sub-micron FeRh nanoislands formed via solid-state dewetting predominantly preserve the metamagnetic phase transition, while islands formed via Volmer–Weber nucleation show strong FM stabilization.

(ii) The specific morphology of the islands most probably either prohibits the AF phase (for square-shaped islands) or supports both phases as established from the Winterbottom constructions.

(iii) FeRh nanoislands display supercooled metastable FM states in a wide range of temperatures. This result suggests that the observations of a long magnetization tail in the cooling branch of the thermal hysteresis in FeRh continuous films (for example in Ref. [78]) is linked to the presence of supercooled FeRh grains or isolated islands.

(iv) The observation of metamagnetic behavior in the wires as narrow as $\sim$50 nm that regularly appear connecting almost separated islands (for example, in Figure 3.2b) suggests that sub-100-nm nanostructures of FeRh can preserve the phase transition.

4 Nanoisland release from the substrate via chemical etching

In order to obtain NPs that could freely interact with surrounding entities (e.g. cells in their native environment), the islands need to be released from the substrate. The ultimate goal of this chapter is to enable nanoisland detachment from the underlying substrate.

For the purpose of reaching this step, we initially attempted to release the islands by a high-power sonication in acetone, as it has been reported for FePd islands formed via dewetting on SiO_2/Si by Barrera *et al.* [33]. However, in our case, the well-separated FeRh islands remained attached to the oxide substrate despite employing high-power sonification at different ultrasound frequencies, and even enhanced by simultaneous heating. We interpret this result in terms of epitaxy which makes the bonds between FeRh islands and crystalline substrates stronger, compared to those between FePd and amorphous silicon oxide substrates where no epitaxial matching can be established.

Instead, this chapter presents the realized experiments investigating chemical wet etching of the substrate to consequently release the supported structures. Here, samples on MgO(001) substrates were selected for further processing due to the high degree of morphology control described in the previous chapters, as well as due to the availability and range of chemicals that enable to etch the substrate.

4.1 MgO etching

On the basis of the experiment performed by Edler and Mayr [80], who dissolved the MgO substrate under their FePd films, we planned to explore the solubility of the MgO substrates under our FeRh films in a 0.3 M aqueous solution of ethylenediaminetetraacetic acid (EDTA). The EDTA should act to release Mg^{2+} ions into water (due to the small solubility of MgO in water) and subsequently form a stable Mg^{2+}-chelate complex (due to four carboxylic acid groups and two amines) [81, 82], while leaving the FeRh alloy structurally and chemically intact.

However, due to low solubility of EDTA in water, we did not succeed in the preparation of the desired aqueous solution. Instead, we produced a 0.3 M solution of disodium salt of EDTA, which was also utilized by Edler and Mayr [80] (see Figure 4.1). The required amount of EDTA disodium salt for a 0.3 M solution (which constitutes the solubility limit of EDTA disodium salt in water at temperatures around 75 °C) was dissolved with the aid of a magnetic stirrer at higher temperatures (~ 90 °C) to speed up the process.

To determine the rate of MgO etching in the EDTA disodium solution, the solution was initially used to dissolve three bare MgO substrates (without the FeRh layer on the top). The weight of a single MgO substrate ($5 \times 5\,\mathrm{mm}^2$) is approximately $m_{\mathrm{MgO}} = 0.045\,\mathrm{g}$ which corresponds to $n_{\mathrm{MgO}} = m_{\mathrm{MgO}}/M_{\mathrm{MgO}} \cong 0.001\,\mathrm{mol}$, where the molar mass of MgO is $M_{\mathrm{MgO}} = 40.3044\,\mathrm{g/mol}$. In order to create the Mg^{2+}-chelate complex, we would need the molar surplus of the EDTA disodium salt, e.g. 10:1 which corresponds to $n_{\mathrm{Na_2EDTA}} = = 10 \cdot n_{\mathrm{MgO}}$. Since the concentration of the prepared solution is $c_{\mathrm{Na_2EDTA}} = 0.3\,\mathrm{mol}$, the required volume of the solution would be $V_{\mathrm{Na_2EDTA}} = n_{\mathrm{Na_2EDTA}}/c_{\mathrm{Na_2EDTA}} = 33.3\,\mathrm{ml}$. Consequently, we poured this volume of 0.3 M solution of EDTA disodium salt into three plastic weighing bottles, we added one clear weighed MgO substrate into each bottle,

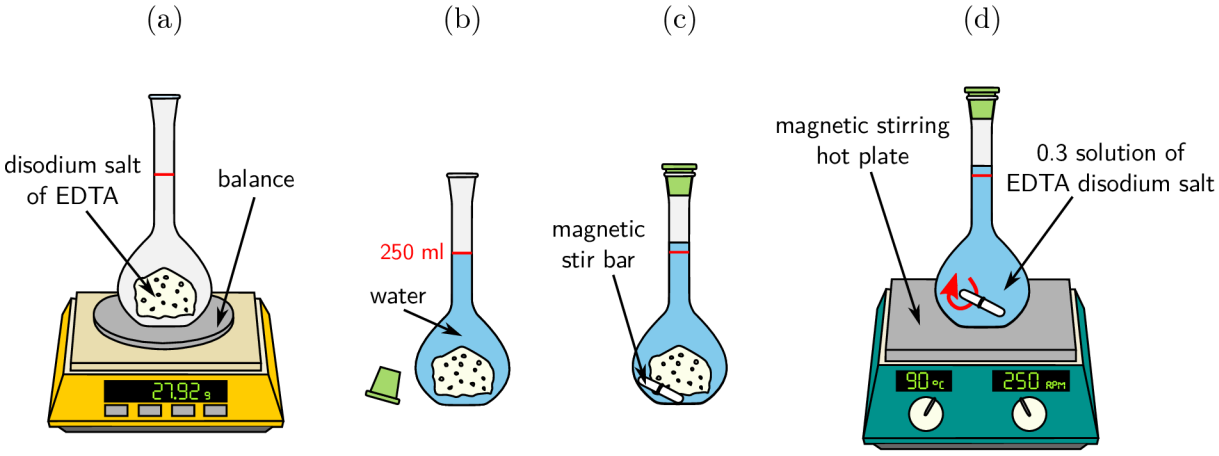

Figure 4.1: Preparation of the 0.3 M solution of EDTA disodium salt: (a) the required amount of EDTA disodium salt for 250 ml was weighed on an analytical balance; (b) water was added up to the mark on the volumetric flask; (c) a magnetic stir bar was put into the flask; (d) disodium salt of EDTA was dissolved using a magnetic stirring hot plate until a clear, transparent solution was obtained.

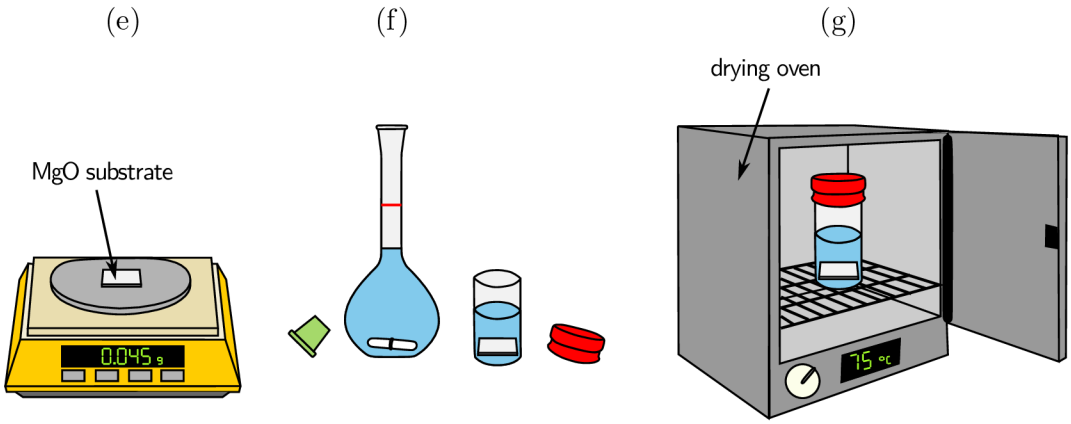

Figure 4.2: Process for determination of the MgO etching rate (several repetitions of the following steps): (a) a bare MgO substrate was weighed on an analytical balance with a weighing chamber enclosed by glass doors for better precision (not shown); (b) 33 ml of 0.3 M solution of EDTA disodium salt was poured into a plastic bottle (only for the first time) and the substrate was added; (c) the etching process was performed in a drying oven at 75 °C.

we carefully closed the bottles to avoid evaporation and inserted them into a drying oven where the etching process was performed at 75 °C (as etching at this temperature was shown to be the fastest in the literature [80]). The substrates were weighed before etching (without the bottle), as well as at different stages during the etching process (the substrates were always taken out from the solution, dried and weighed). The weight of the particular substrates was recorded as a function of the etching time. The experiment is schematized in Figure 4.2. The measured data are plotted in Figure 4.3a and additionally fitted by a straight line in the early stages of the etching, indicating a linear trend. The exposed area of the substrates starts to significantly decrease during more advanced stages of the etching, slowing down the etching rate and thus deflecting it from the linear time dependence.

(a) EDTA disodium salt

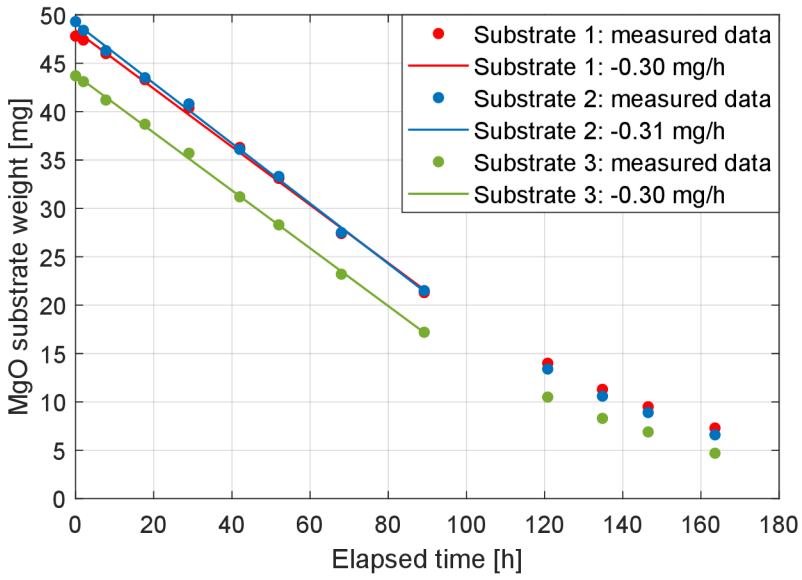

(b) citric acid

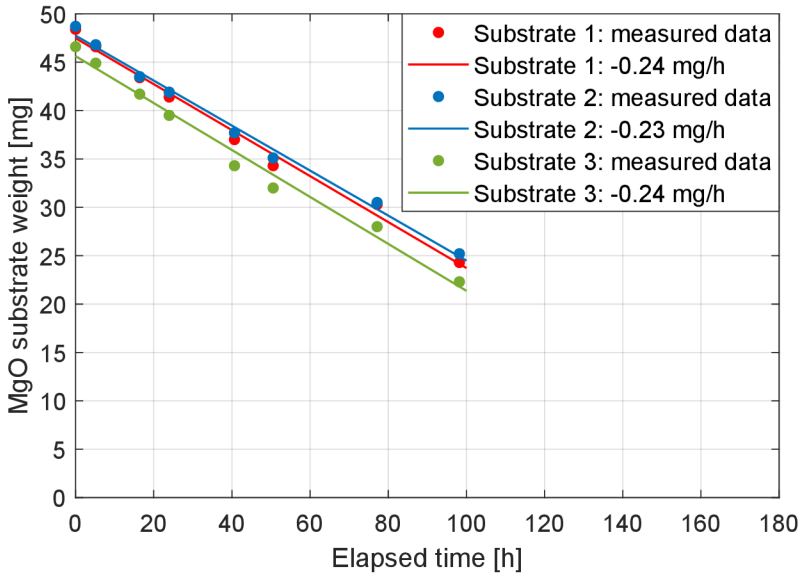

Figure 4.3: The chemical etching of MgO substrates: (a) in a 0.3 M solution of disodium salt of EDTA at 75 °C; (b) in a 1 M solution of citric acid at 42 °C and 80 rpm.

Besides, we investigated the etching of MgO substrates in a solution of citric acid. According to the results presented by Demir [83], we prepared a 1 M solution and the experiments were carried out at temperature 42 °C with simultaneous stirring at a speed of 80 rpm (the highest temperature and speed provided by our temperature-controlled shaker). The measured weights of three MgO substrates during the etching process are plotted in Figure 4.3b and again fitted by a linear trend curve. Since the MgO etching in the solution of disodium salt of EDTA (~ -0.30 mg/h) turned out to be faster than the etching in the citric acid solution (~ -0.24 mg/h), the 0.3 M solution of EDTA disodium salt was chosen for the subsequent experiments.

4.2 Releasing continuous FeRh films from MgO

In order to test that MgO can be etched when placed below FeRh, a 20-nm-thick continuous FeRh film was initially chosen rather than a sample with island-like morphology, as the film consists of a shiny metallic layer which is well discernible on the MgO substrate as well as in the etching solution. In contrast, the samples featuring separate islands often show a transparent character across the MgO substrate, such that one cannot distinguish without a magnified view whether the islands are already detached from the substrate.

The first attempt to dissolve the MgO under the continuous FeRh film was performed using 33.3 ml (which corresponds to a molar ratio of 10:1 between the EDTA disodium salt and MgO) of a 0.3 M solution of EDTA disodium salt at 75 °C. After 6 hours in the solution, the slightly disrupted FeRh film (probably due to the presence of structural defects) was already detached from the MgO substrate and floating on the surface of the solution. The film was then carefully pulled from the solution using a sheet of paper (see Figure 4.4).

Latter experiments showed that it is not necessary to dissolve a significant part of the MgO substrate for the purpose of detaching the FeRh deposited on top. As for the latter separation of islands from the solution, it would be desirable to reduce the volume of the etching solution in order to increase the concentration of released FeRh particles. Consequently, as the next step, we investigated to what extent one could reduce the etching volume while still permitting the film to detach from the substrate. The continuous FeRh film (with a nominal thickness of 20 nm) was successfully detached in the volumes of 16.7 ml (with a molar ratio of 5:1 between EDTA disodium salt and MgO), 6.7 ml (with a molar ratio of 2:1) and 3.3 ml (with a molar ratio of 1:1). However, the lower the volume of the etching solution, the longer time is required to separate the FeRh layer from the substrate. For volumes as low as 1.7 ml (with a molar ratio of 1:2), the film stayed attached to the MgO substrate even after several days.

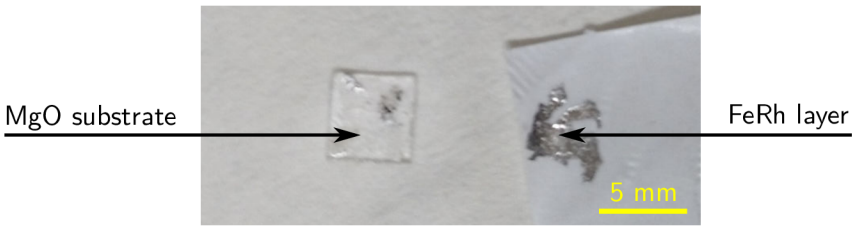

Figure 4.4: Disrupted FeRh layer detached from the MgO substrate on a piece of paper.

4.3 Releasing W, Pt, Fe and FeRh nanostructures from MgO

To check the ability to obtain free-standing FeRh nanoparticles, it is necessary to detach islands from the substrate and additionally confirm their presence in the solution by means of suitable experimental methods. Due to high price of FeRh, the first tests were performed on structures made of different materials, specifically of W, Pt and Fe.

In adition, for the purpose of visualizing the course of etching and the subsequent release of particles in the solution, a special experimental configuration is presented in this section, ensued by an observation of detachment of a partially dewetted FeRh film.

Releasing lithographically patterned W structures from MgO

As a way to estimate the time required for detaching FeRh islands from the substrate, lithographically patterned W structures with different controlled sizes were fabricated. Epitaxial W films were grown on MgO via magnetron sputtering [66], which constitutes a system comparable to FeRh for estimating the time of detachment in the solution. Stripes were patterned by electron beam lithography using a negative resist (hydrogen silsesquioxane - HSQ) and ion etching in Ar plasma (performed by M. Takhsha Ghahfarokhi). The thickness of the W layer was chosen to approximately imitate the median height of the FeRh islands ($\sim$60 nm) and the stripes were designed to include various widths corresponding to different sizes of nanoislands (ranging from 500 nm up to 2 µm).

The W stripes were exposed to a 0.3 M solution of EDTA disodium salt at 75 °C using a reduced volume of 1.7 ml (with a molar ratio of 1:2 between EDTA disodium salt and MgO), as the release occurs easier for the discontinuous layer architecture than for continuous films. The W stripes were examined via optical microscopy after 10 min in the etching solution (see Figure 4.5a). The number of stripes of different widths left on MgO are listed in Table 4.1. While almost one half of the narrowest stripes was washed out from the substrate, the widest stripes remained nearly untouched after 10 min.

The sample was placed back into the etching solution for 10 min. It was observed that after 20 min of total etching time, almost all structures were removed from the MgO substrate. Only a few were still on the MgO, however not at their original positions but mixed all together (see Figure 4.5b). Considering the performed experiment, we anticipate that the detachment of FeRh island arrays should be effectively realized within 30–60 min depending on their particular size and spacing.

Nominal width of stripes [nm]	Number of stripes before etching	Number of stripes after etching	Ratio of remaining stripes [%]
500	480	287	60
800	480	323	67
1200	480	436	91
2000	480	476	99

Table 4.1: Quantities of the lithographically patterned stripes before and after 10 min etching. The width and length (4.5 µm) of stripes were corroborated using AFM.

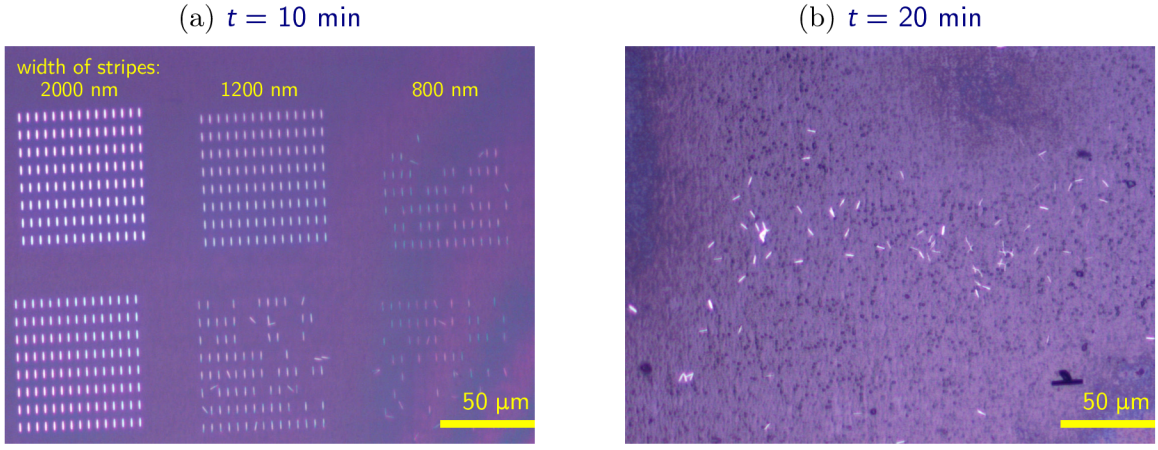

Figure 4.5: Optical microscope images of W structures: (a) after 10 min (stripes with widths of 800 nm, 1200 nm and 2000 nm); (b) after 20 min in the etching solution.

Releasing Pt islands from MgO

For the purpose of testing the ability to transfer islands and thus to obtain dispersed particles in the etching solution, we prepared Pt islands as Pt posseses zero net magnetization, similarly to AF FeRh at room temperature, thus avoiding undesirable agglomeration effects of the particles. The first step consisted in tuning the deposition parameters in order to obtain well-separated Pt islands formed via dewetting. Pt growth was performed at room temperature using a power of 50 W and an Ar pressure of $2.5 \cdot 10^{-3}$ mbar. Well-separated islands were deposited upon nominally 10-nm-thick Pt film that was subjected to a 3-h-long annealing process at 820 °C. The fabricated samples featured well-separated islands with arbitrary shapes and curved boundaries, having characteristic sizes around 1 µm, as well as a smaller population of dot-like islands with sizes around 200 nm (see Figure 4.6a). The Pt islands were then released from the underlying MgO in 1.7 ml of a 0.3 M solution of EDTA disodium salt. The successful detachment was supported by visual inspection of the sample, turning from light gray to fully transparent appearance across the MgO subtrate, upon being removed from the solution after etching.

The solution with dispersed Pt islands was used for particle size and concentration analysis via dynamic light scattering (DLS). The presence of dispersed Pt particles in the liquid environment was confirmed, but the quantitative estimate of size distribution and concentration showed to be challenging to achieve (for more details, see Appendix B).

Releasing Fe islands from MgO

Fe islands, formed via dewetting, were prepared to substitute the FM FeRh islands in the tests aiming for magnetic separation of detached particles from the etching solution. Fe growth was done at 360 °C using a power of 50 W and an Ar pressure of $2.7 \cdot 10^{-3}$ mbar. The well-separated Fe islands were obtained by depositing a film of 12 nm nominal thickness after a 80-min-long annealing process at 820 °C. The obtained islands, regular both in shape and size ($\sim$ 200 nm, see Figure 4.6b), were released from the underlying MgO substrate in 1.7 ml of a 0.3 M solution of EDTA disodium salt. The Fe islands were used for experiments presented in Chapter 5.

Real-time visualization of MgO etching under a partially dewetted FeRh film

In order to observe the nanostructures during the course of MgO etching as well as in the solution, a special experimental configuration was set-up (see Figure 4.7). A *Zeiss Stemi 508* stereo microscope enables magnified vision of the sample inside a beaker during the etching process. The temperature is controlled via a custom-made heating stage based

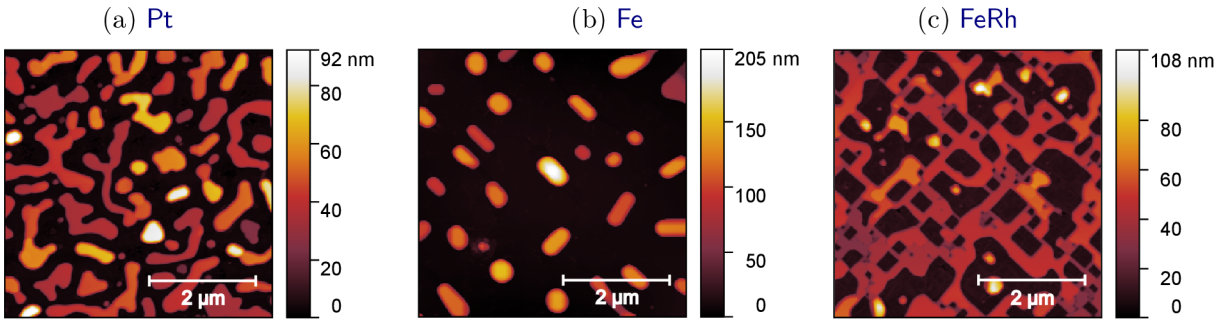

Figure 4.6: AFM images of nanostructures used for MgO etching tests: (a) Pt islands formed via dewetting on MgO(001); (b) Fe islands formed via dewetting on MgO(001); (c) FeRh film at an early stage of dewetting.

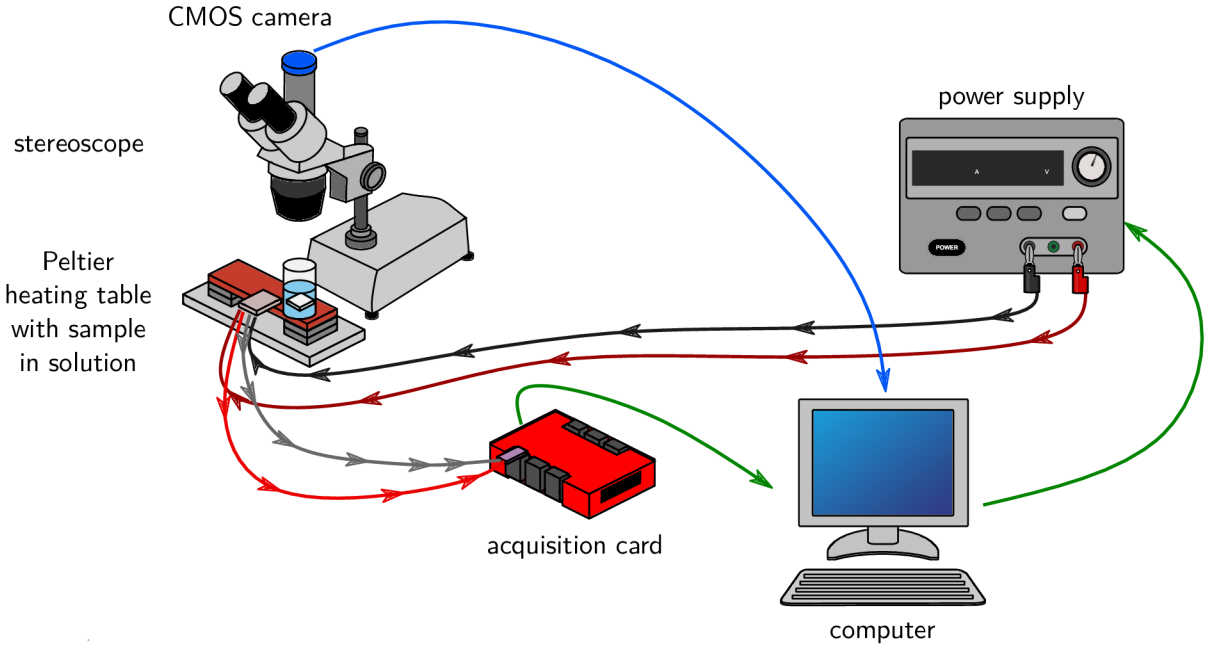

Figure 4.7: Schematics of the experimental setup enabling observation of MgO etching using a stereo miscroscope and a PID-controlled heater stage. The temperature is controlled with a *LabVIEW* program by adjusting the current passing through the Peltier cells via feedback mechanism. The temperature near the beaker is measured with a Pt thermistor and retrieved using an acquisition card.

on Peltier modules (which is an adapted version of the stage utilized for temperature-dependent MFM measurements). By incorporating a CMOS camera (*FLIR Chameleon3*) to the stereoscope, image acquisition of the etching process can be performed in real time instead of at particular intermediate stages.

The efficiency of MgO etching was initially examined on a partially dewetted FeRh film with a nominal thickness of 16 nm (see Figure 4.6c). The sample was inserted into a glass beaker with 1.7 ml of a 0.3 M EDTA disodium salt solution and the beaker was placed without any cover onto the Peltier heating stage (see Figure 4.7). Subsequently, the sample stage was heated to a temperature of 65 °C.

The FeRh sample was monitored in the course of etching. We show the FeRh sample before etching ($t = 0$, see Figure 4.8a) as well as after 35 min, 70 min, 105 min, 270 min since the beginning of etching (see Figure 4.8b–e, respectively). The etching was initiated at several regions on the sample as the film exhibited a large number of nucleated holes where the MgO substrate was exposed (see Figure 4.8b–c). However, once detached, the majority of FeRh film fragments still remained on the substrate, aggregating into larger clusters (see Figure 4.8d–e). We argue for a strong magnetic attraction between the detached parts of the film as a result of the large value of saturation magnetization at a given temperature ($M \approx 1200\,\mathrm{kA/m}$ at 65 °C, data not shown). The film seemed to be attached to the substrate even after 270 min of etching (see Figure 4.8e), but was released after gently shaking the beaker.

Additionally, we show the surface of another sample before etching (see Figure 4.9a) and a few hours after etching when cooled down to room temperature (see Figure 4.9b), the latter containing salt crystals on top. As discussed above, this can be understood in terms of the decreased solubility of the EDTA disodium salt at room temperature.

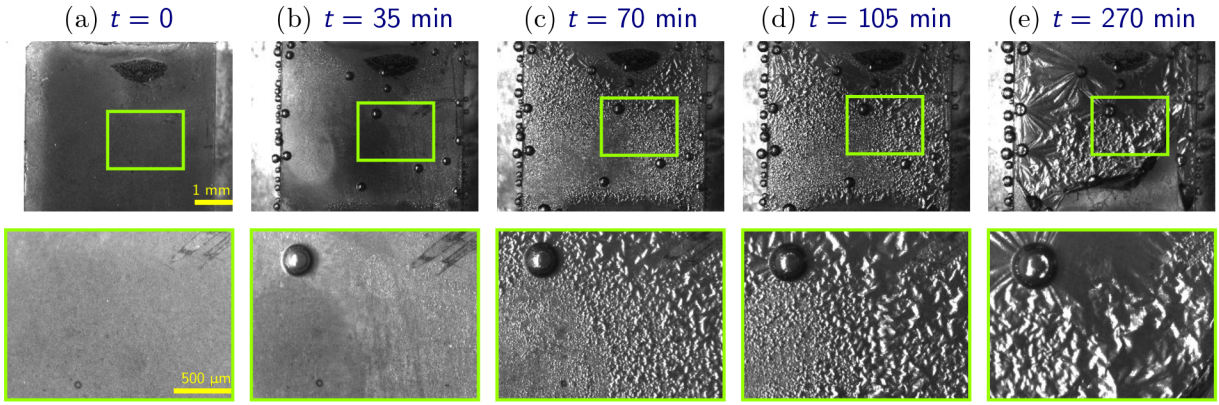

Figure 4.8: Partially dewetted FeRh film: (a) before etching; (b) after 35 min; (c) 70 min; (d) 105 min; (e) 270 min from the beginning of etching. Images in the bottom panel correspond to zoomed-in regions marked in green in the images in the top panel.

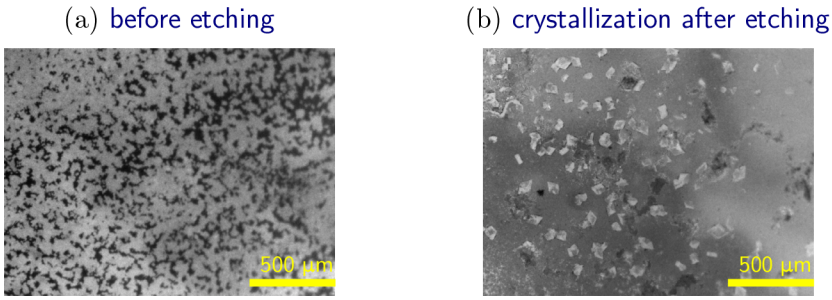

Figure 4.9: Salt crystallization after cooling to room temperature: (a) sample surface before etching; (b) sample surface at room temperature a few hours after etching.

4.4 Overview of etching tests

All etching experiments described so far were performed to examine the character and efficiency of the nanostructure release process, as a preparation for the attempts to be made on samples with well-separated FeRh island arrays. In particular, it is worth noting:

(i) The volume of a 0.3 M solution of EDTA disodium salt needed for detaching a deposit from MgO strongly depends on the sample morphology, especially on the exposed substrate area. While well-separated nanostructures (e.g. W stripes, Pt or Fe islands) can be released in 1.7 ml of the solution, this is not possible for a continuous film.

(ii) The time of nanostructure detachment depends on the volume of the solution, on temperature, as well as on the morphology of the given sample. Lithographically patterned W stripes (with widths < 2 µm) were all released in less than 20 min. However, this was not the case for samples with a smaller relative exposed substrate area.

(iii) The solubility of EDTA disodium salt is reduced with decreasing temperature. For the 0.3 M solution, this leads to salt crystallization over time when cooled from the higher temperature of etching to room temperature. As a general observation, this effect is accelerated when the temperature drop is faster. Besides, compared to the pure solution of EDTA disodium salt, crystallization is more prominent once the solution contains Mg^{2+} ions released from the substrate.

(iv) Detached nanostructures possessing a certain value of saturation magnetization at the temperature of etching tend to agglomerate, as concluded from the observations made on the partially dewetted FeRh film sample under the stereoscope.

5 Nanoparticle separation from the etching solution

Following the etching, FeRh NPs need to be extracted from the acidic environment. This is necessary for two reasons: (i) to remove the salt which crystallizes at room temperature and interferes with NP dispersion or agglomeration; (ii) to put the NPs into a platform enabling further investigation. Consequently, NPs are intended to be transported from the etching solution onto a new substrate (such that NPs would be supported but not clamped to MgO, as before detachment) or into another liquid environment such as pure water.

This chapter presents the routes investigated to reach this objective, as well as the experiments performed to analyze their efficiency. Initially, a number of non-magnetic separation approaches are introduced, which turned out not to be suitable or could not be implemented. Then, the magnetic separation strategy as well as the tests done on Fe and FM-FeRh NPs are explained in detail.

5.1 Nanoparticle separation strategies

In order to separate NPs from the etching solution, several approaches were pursued. Here, we also list a number of separation strategies which could not be successfully implemented. For the first separation tests, Pt or Fe NPs were used instead of FeRh.

Filtration

The first approach consisted in suction filtration, for which a conventional vacuum filtration apparatus was employed. Membrane filters made of polycarbonate with pore sizes of 100 nm were placed into a Büchner funnel with the goal to capture NPs, possessing generally sizes > 100 nm. However, not even pure water could be sucked through the filter despite the connection of an aspirator aiming for a pressure-gradient acceleration towards the inside of the Büchner flask.

Centrifugation

Next, an attempt was made to separate NPs using a centrifuge, based on exerting a high-speed rotation of the liquid solution which in turn generates a centrifugal force upon the particles in the suspension. Accordingly, the etching solution with released Pt NPs was placed into a special vial, which was subsequently put into a centrifugal machine and spun at a high speed. Once the process was finished, the vial was taken out from the centrifuge. In addition to Pt NPs, we observed that the salt crystals were segregated at the bottom of the vial. This strategy was therefore also rejected for the potential separation of FeRh NPs.

Attachment to a polydopamine layer

Another method could be based on coating a substrate by a thin polydopamine (PDA) film and subsequent insertion into the etching solution with released NPs. Dopamine is a hormone and a neurotransmitter found in the human body, which adheres to all types of surfaces even under water [84]. PDA coating is thus used for the functional modification

of surfaces for various types of biomedical applications such as promoting cell adhesion. Accordingly, we expect FeRh NPs to attach to such a functionalized surface as well.

PDA layers are conventionally created through simply dip-coating objects in an aqueous solution of dopamine [85]. Despite not succeeding in a PDA coating of bare Si substrates using a standard procedure, a PDA layer was nevertheless formed when plasma oxidation of Si substrates preceded the PDA deposition. However, attachment of NPs to the PDA surface could not been investigated so far due to lack of time.

Magnetic separation

The last NP separation strategy aims for the use of magnetic fields to attract NPs with a sizeable magnetic moment. The procedure is schematically shown in Figure 5.1. The NPs are initially dispersed in the etching solution within an Eppendorf tube, or alternatively forming clusters due to mutual magnetic interactions (see Figure 5.1a). Next, a strong NdFeB permanent magnet providing a field of $\sim 0.5\,\mathrm{T}$ at about 1 cm from its surface is approached to the bottom part of the tube, thus exerting a magnetic force onto NPs in the solution which tend to agglomerate at the bottom (see Figure 5.1b). In this way, the excess solution from the top part can be removed using a pipette (see Figure 5.1c). Consequently, the volume of the liquid in the tube is considerably reduced (see Figure 5.1d). The content of the tube is subsequently diluted with deionized water (see Figure 5.1e). The whole procedure is repeted several times (see the green arrows in Figure 5.1). As a last step, the magnet is removed and the reduced liquid volume containing slightly dispersed NPs is captured using a pipette (see Figure 5.1f) and transferred into a new platform, such

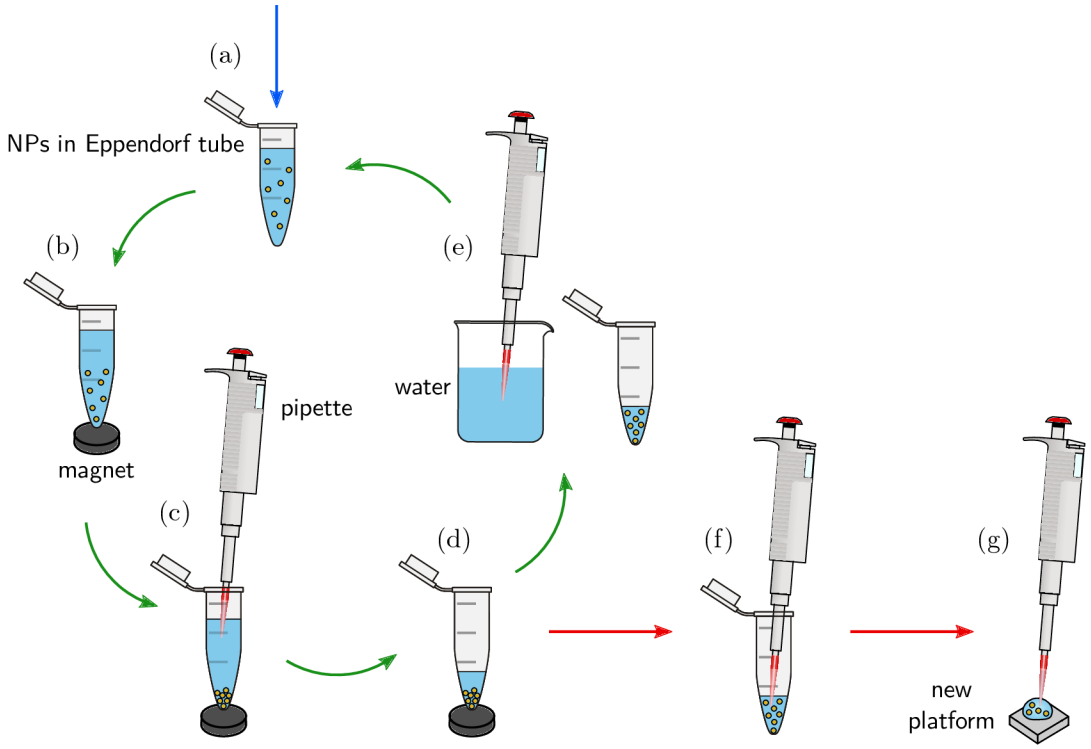

Figure 5.1: Magnetic separation of NPs from the etching solution: (a) Solution with NPs in an Eppendorf tube; (b) placing a magnet at the bottom of the tube; (c) removal of the excess solution; (d) reduced volume of the solution; (e) addition of water for purification of the solution; (f) reduced volume with NPs sucked into a pipette; (g) NPs transferred onto a substrate.

as a clean substrate or a polypropylene capsule for VSM measurements, enabling further investigation (see Figure 5.1g).

5.2 Separation of Fe nanoparticles

Magnetic separation was initially performed to transfer Fe NPs onto a Si substrate. Subsequently, the sample was lyophilized[1] for the purpose of water removal (see Figure 5.2a). To find out whether the Fe NPs were successfully separated, the composition of the as-prepared sample was examined via energy-dispersive x-ray (EDX) spectroscopy, which is performed in a special configuration of the electron microscope, with the assistance of M. Staňo.

Specifically, SEM-EDX analysis was performed on a selected NP cluster found on this sample (see the SEM micrograph in Figure 5.2b). In order to investigate whether the cluster consists of Fe NPs, EDX spectra of two regions were acquired (indicated by the red dot on the cluster and the green dot beyond the cluster in Figure 5.2b). The EDX spectrum of the cluster indeed confirms the presence of Fe (see Figure 5.2c). Besides, the spectrum contains peaks of O, N, C and Na (corresponding to the residues of EDTA disodium salt), as well as peaks of Mg (due to the etched MgO substrate), Si (due to the actual substrate), Cr (possibly due to the use of Cr containing instrumentation) and a small peak of Al (of unknown origin). The significant O peak can also result from Fe oxidation. While investigating a region beyond the cluster, SEM-EDX analysis reveals a

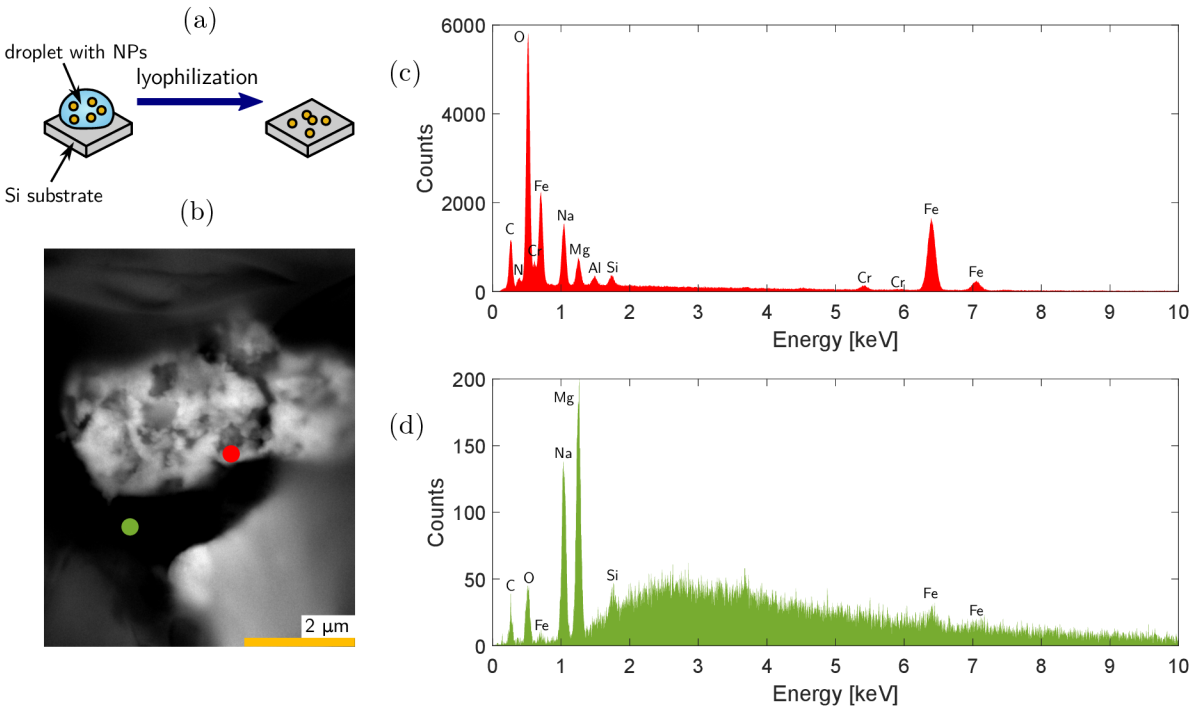

Figure 5.2: SEM-EDX analysis performed on Fe NPs transferred onto a Si substrate: (a) schematics of lyophilization prior to the analysis; (b) SEM image of a cluster; (c) EDX spectra acquired on the region indicated by the red dot in (b); (d) EDX spectra acquired on the region indicated by the green dot in (b).

[1]Lyophilzation, or freeze-drying, is a process of water removal achieved by freezing the material, reducing the pressure and heating back to room temperature, which allows the ice to change from solid to vapor without passing through a liquid phase.

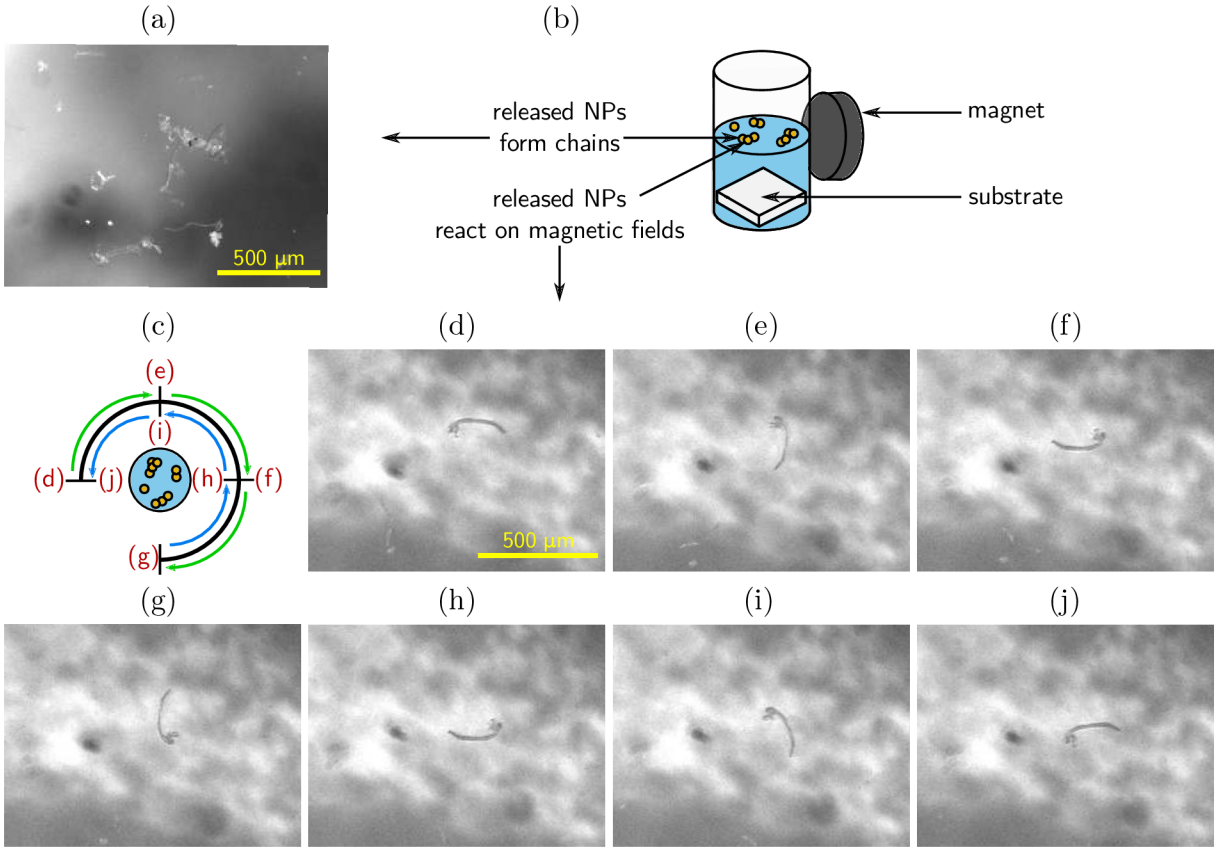

Figure 5.3: Observation of free-standing Fe NPs under the stereoscope: (a) NPs forming chain-like clusters; (b) schematics of magnetically controlled NPs; (c) position of the permanent magnet with respect to the top-view of the beaker and images (d)–(j); (d)–(j) sequence of images of a selected chain-like cluster under rotation of the magnet.

different composition consisting of O, C, Na, Mg, Si and Fe (see the data in Figure 5.2d). Importantly, the Fe peaks here are much lower compared to the spectrum of the cluster.

Consequently, we argue that the cluster contains a large fraction of Fe NPs. However, while the NPs were successfully transferred from the solution to the substrate, the solution was not completely purified from the residues.

Another experiment on Fe NPs was performed using the special setup presented in Section 4.3 (see Figure 4.7). Here, Fe islands that were detached from the substrate were investigated as free-standing NPs under the stereoscope used to visualize the etching process. It was observed that NPs remain on the surface of the solution and form chain-like clusters due to interparticle dipole-dipole interactions (see Figure 5.3a). Besides, these aggregates can be reoriented using a relatively strong NdFeB permanent magnet (see Figure 5.3b). Here, we show a sequence of images for a $\sim$200-µm-long chain acquired while rotating the magnet around the beaker by 270 ° and back (see Figure 5.3b). Accordingly, the chain was reoriented while in the aqueous solution by following the stray field of the magnet (see Figure 5.3d–j).

In addition, Fe NPs were magnetically separated and transferred into a capsule suitable for VSM measurements (see Figure 5.4a). Once the water evaporated, the capsule was closed and the field-dependent magnetic loop was measured (see Figure 5.4b). The saturated magnetic moment of transferred NPs is $m \approx 17\,\mathrm{nA}\cdot\mathrm{m}^2$, while the saturated magnetic moment of samples containing Fe islands (with a nominal thickness of 12 nm) is

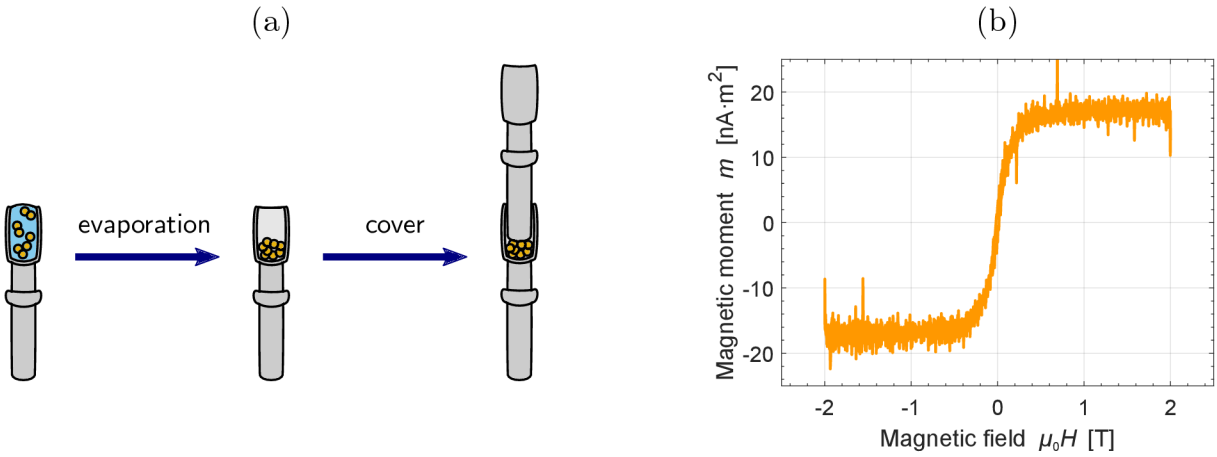

Figure 5.4: VSM measurement of transferred Fe NPs: (a) schematics of Fe NP insertion strategy into a capsule for VSM measurements; (b) magnetic moment vs magnetic field loop of separated Fe NPs.

typically $m \approx 380\,\mathrm{nA} \cdot \mathrm{m}^2$. This means that the fraction of transferred Fe NPs is about 5% of the total number of supported Fe islands.

5.3 Separation of FM stabilized FeRh nanoparticles

Thereafter, closely spaced FeRh nanoislands formed via Volmer–Weber growth were detached from MgO substrates. Due to the FM stabilized state of the islands, these samples constitute a good initial test platform to optimize magnetic separation of FeRh NPs.

At first, a sample with a nominal thickness of 40 nm was etched and observed under the stereoscope. Due to the reduced island spacing, typical for Volmer–Weber growth, clustered FeRh fragments of up to 100 µm in size were observed in the solution upon etching. (see Figure 5.5a). Subsequently, a permanent magnet (0.5 T) was placed towards the beaker from the left side ($t = 0$). As a result of this, FM FeRh clusters oriented their longer axis to be favorably aligned with the stray field of the magnet ($t = 1\,\mathrm{s}$, see Figure 5.5b) and started to approach the magnet right after, until no piece was seen in the central region of the beaker ($t = 50\,\mathrm{s}$, see Figure 5.5c).

Next, islands of a sample with a nominal thickness of 12 nm were also detached from the MgO substrate, observing the formation of clusters that floated on the surface of the

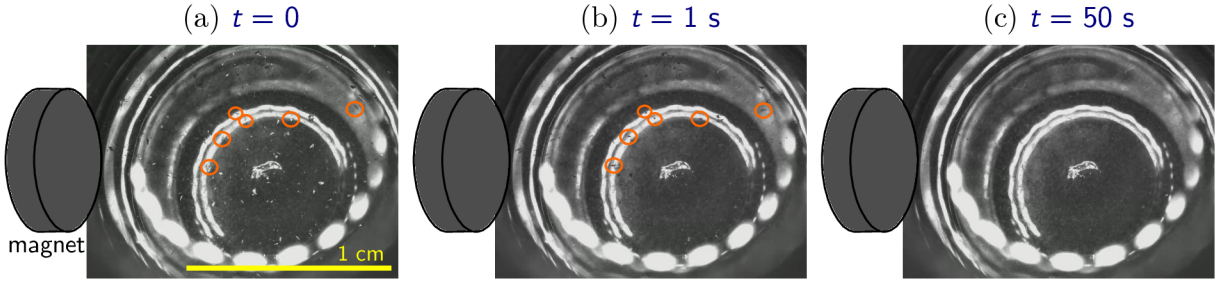

Figure 5.5: Magnetic attraction of sub-milimiter FM stabilized FeRh pieces: (a) clusters on the surface; (b) clusters are rotated into the magnetic field direction; (c) no cluster seen on the central region of the beaker. A few selected clusters are marked in orange in (a)–(b). The static bright feature in the center of the beaker is a reflection feature from the bottom part of the beaker.

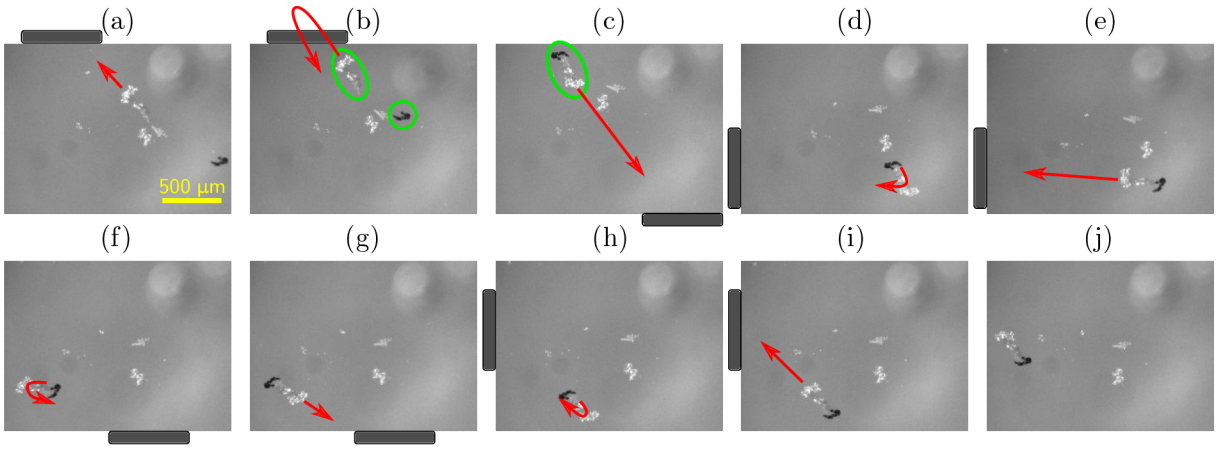

Figure 5.6: Magnetic field-induced motion of a FeRh cluster: (a) the piece is attracted to the magnet; separated pieces in (b) stick together (c). When the position of the magnet is changed, the largest cluster firstly rotates (d,f,h), then moves towards the magnet (e,g,i–j).

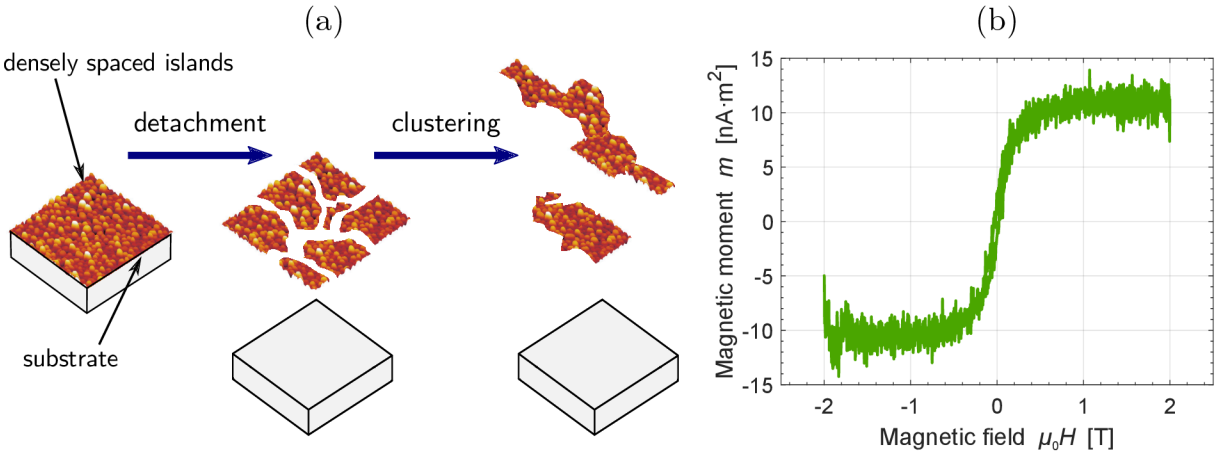

Figure 5.7: (a) Densely packed FM FeRh islands are detached in clusters of aggregated FeRh NPs. (b) Field hysteresis of the transferred material acquired at 300 K.

solution. The motion of a selected cluster was recorded on the camera and is presented in Figure 5.6. The red arrows indicate the travel trajectory of the cluster in between subsequent images. In addition, the approximate actual position of the magnet placed from outside of the beaker is marked by the black rounded rectangle. Besides being pulled towards the magnet (see Figure 5.6a), the clusters were attracted to each other upon bringing the permanent magnet close to the beaker (see the clusters marked in green in Figure 5.6b–c). Every time the position of the magnet was changed, the largest piece firstly rotated around its axis (see Figure 5.6d,f,h), then started to drifts towards the magnet (see Figure 5.6e,g,i–j).

Furthermore, the detached FeRh clusters of the aforementioned sample (see illustration in Figure 5.7a) were magnetically separated and transferred into a VSM capsule. The resulting room temperature hysteresis curve is shown in Figure 5.7b. The saturated magnetic moment of the transferred material is $m \approx 11\,\mathrm{nA \cdot m^2}$. Compared to the $m \approx 270\,\mathrm{nA \cdot m^2}$ moment measured for the sample on the substrate before etching, the transferred fraction is $\sim 4\%$.

5.4 Overview of released ferromagnetic nanoparticle behavior

Main findings for the magnetic behavior of detached FM islands are the following:

(i) Fe or FM-FeRh NP clusters can be transferred from the etching solution in another environment such as a substrate or a VSM capsule.

(ii) The quality of purification from residues remains challenging and further optimization is needed.

(iii) Once released, all nanoparticle systems observed here tend to agglomerate due to magnetic dipole-dipole interactions. Fe NPs form chains, whereas FM-FeRh NPs seem to be arranged in bulkier clusters rather than long chains.

(iv) While bigger aggregates are attracted towards a magnet, smaller clusters only rotate. The magnetic force $\mathbf{F}_\mathrm{m}$ experienced by a magnetic particle within an applied magnetic field $\mu_0\mathbf{H}$ is given by [19]

$$\mathbf{F}_\mathrm{m} = (\mathbf{m} \cdot \nabla)\mu_0\mathbf{H}, \tag{5.1}$$

where $\mathbf{m}$ is the magnetic moment of the particle, and thus it depends on the magnetic field gradient acting on the FM body. The magnetic force $\mathbf{F}_\mathrm{m}$ can be rewritten as [19]

$$\mathbf{F}_\mathrm{m} = V\Delta\chi(\mathbf{H} \cdot \nabla)\mu_0\mathbf{H}, \tag{5.2}$$

where V is the volume of the particle, $\Delta\chi$ is the effective susceptibility of the particle relative to the solution. From Equation (5.2), one can see that the magnetic force depends directly on the particle volume, thus larger clusters are more attracted towards a magnet. In addition, larger aggregates are less susceptible to the random fluctuations in the fluid leading to the Brownian motion.

Consequently, an insufficient magnetic force acting on smaller clusters or individual NPs can hinder the possibility of transferring larger NP fractions ($> 5\%$).

6 Magnetic properties of FeRh nanoparticles

The objective of Chapters 4 and 5 was acquiring all necessary ingredients to prepare and characterize self-standing FeRh NPs. This chapter follows with an observation of metamagnetic NPs in a temperature-controlled liquid environment. Then, collective temperature-dependent magnetic properties of self-standing FeRh NP systems are reported on the basis of magnetometry measurements.

6.1 Behavior of metamagnetic nanoparticles in a liquid environment

After having investigated the NP detachment from the substrate and the NP separation from the etching solution on test samples, well-separated metamagnetic islands were also prepared. In particular, sample M(001)-16c, displaying large spacing between elongated, wire-like islands (see Figure 2.10a), was etched at 65 °C in the experimental setup presented in Figure 4.7. Initially, it was observed that free-standing particles tend to form clusters which assemble into complex structures with a size of $\sim 100\,\mu m$ (see Figure 6.1a). However, at 65 °C, relatively compact clusters are not kept together by strong magnetic interactions, but rather by adhesive forces, as the constituent clusters can change their positions in the aggregate (see the clusters marked in green and blue in Figure 6.1a–b). In general, the aggregates of clusters grow in time (see the additional purple cluster in Figure 6.1c) due to a higher number of detached NPs as well as due to the more prominent thermal agitation above room temperature, which causes a higher probability of collision between clusters.

Next, the solution containg detached NPs was heated up to 80 °C. At this temperature, the observed changes were more dynamical. Here, we show two clusters merging into one system in a short time interval of 12 s (see Figure 6.2a–d). At the beginning ($t = 0$), the clusters were rotating around each other without forming any visible connection (see Figure 6.2a–b). Suddenly, the rotation direction of individual clusters reversed (see Figure 6.2c), as the clusters were strongly attracted to each other, forming a stable, larger aggregate (see Figure 6.2d). This dynamic behavior at 80 °C, in comparison to 65 °C, can be linked to the large magnetization increase of FeRh upon heating in this temperature range (see the magnetometry of the supported islands of sample M(001)-16c

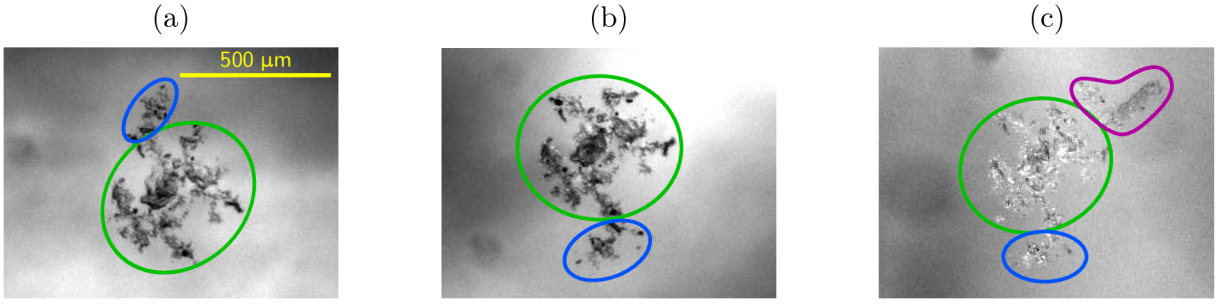

Figure 6.1: FeRh NP aggregate of clusters observed at 65 °C: (a)–(b) constituent clusters can be mutually reoriented; (b–c) the system grows in time. Three different clusters are marked in colors.

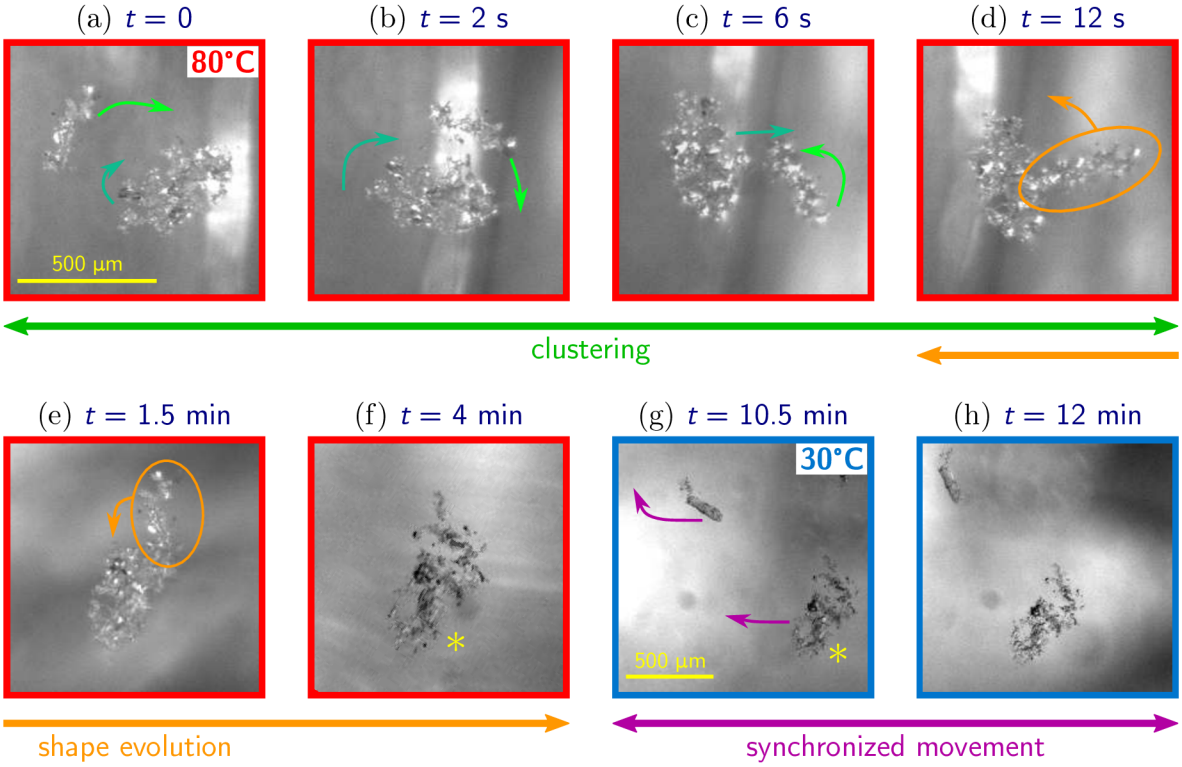

Figure 6.2: An aggregate of sub-200-nm FeRh NPs: (a)–(f) at 80 °C; at 30 °C (g)–(h). (a–d) Dynamical cluster merging (the green arrows indicate the travel trajectory of the clusters in between subsequent images); (d)–(f) shape evolution to a more compact arrangement (the orange arrow indicates the position change of the marked cluster part relative to the remaining cluster body in between subsequent images); (g)–(h) synchronized movement of distant clusters (the purple arrows indicate the travel trajectory of the clusters in between subsequent images). The asterix in panels (f)–(g) indicates the same cluster.

in Figure 3.4b).[1] Besides, we have observed that the position of the clusters fluctuates more due to the increased thermal agitation.

Upon maintaining the temperature of the solution at 80 °C, the shape of the given cluster evolved into a more compact arrangement (see Figure 6.2d–f). We argue for a significant influence of magnetic interactions, attracting the individual components together.

Subsequently, the system was cooled down to 30 °C and its evolution was followed over the course of tens of minutes. No significant change was observed in the cluster arrangement, such as a tendency for segregation upon the magnetization decrease associated with the metamagnetic phase transition during cooling. Instead, we report on another phenomenon consisting in a synchronized movement of clusters, being 1 mm apart from each other without any visible interconnection (see Figure 6.2g–h).

This can be in fact explained by an observation performed on a sample containing well-separated, sub-200-nm metamagnetic islands, similar to those of sample M(001)-12a (see Figure 2.5d). The released NPs formed a system with long chains (see Figure 6.3a–b) and with vast nets of almost invisible aggregates (see Figure 6.3b,c). In this way, one could observe a synchronized movement of bigger clusters, which were in reality interconnected through a complex chain-like arrays. The available optical resolution under

[1] One should consider a possible change in magnetic behavior of NPs when released from the substrate.

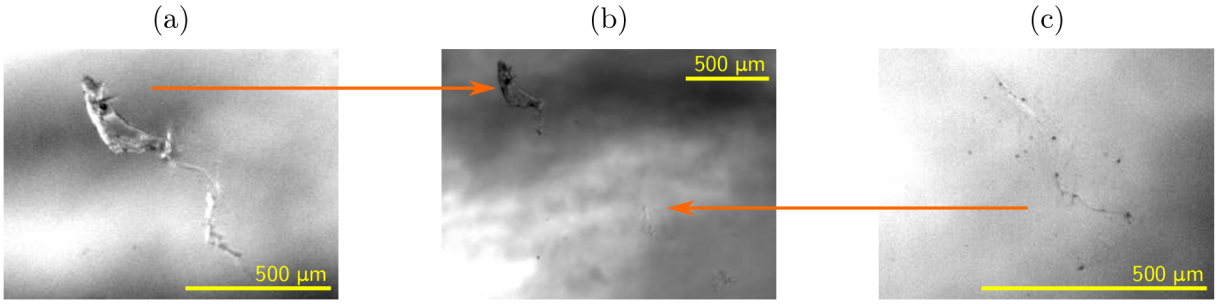

Figure 6.3: Released sub-200-nm NPs: (a) a bigger cluster connected to (c) an almost invisible chain-like net, creating a collective motion of aggregates. The available optical resolution does not allow to visualize their interconnection in (b). The orange arrows indicate the approximate position of the clusters (a) and (c) in (b).

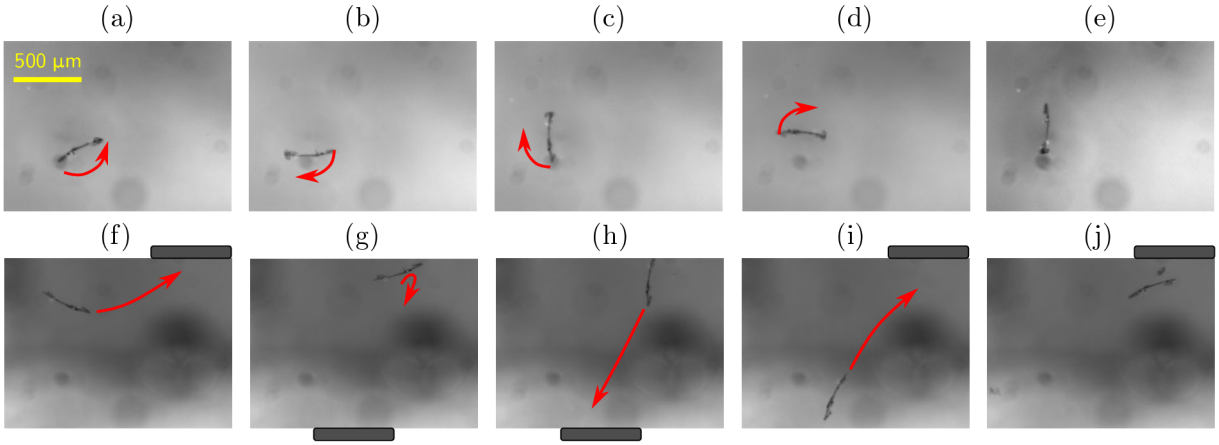

Figure 6.4: Control of an FeRh NP aggregate using a permanent magnet: (a)–(e) rotation; (f)–(j) motion towards a permanent magnet. The red arrows indicate the travel or rotation trajectory of the cluster in between subsequent images. The approximate actual position of the magnet for (f)–(j) placed from outside of the beaker is marked by the black rounded rectangle.

the stereoscope, however, does not allow to clearly visualize the chain formation at the micron scale, such that the motion of clusters appears to be ”invisibly” connected.

Besides, it was seen that free-standing metamagnetic NPs forming larger aggregates can be rotated, as well as attracted using a permanent magnet, similarly as it was seen for the released test structures (see Figure 6.4).

6.2 Magnetometry of self-standing FeRh nanoparticles

In order to quantitatively examine whether the metamagnetic behavior is preserved after detachment from the substrate, or if it is modified, the overall magnetic moment of the separated FeRh NP fraction was measured vs field and temperature using VSM.

Initially, we revisited the sample containing closely spaced FeRh islands with a nominal thickness of 12 nm, reported in Section 5.3.[2] Having considered the sample morphology pointing towards Volmer–Weber growth as well as the MFM scan showing adjacent regions of positive and negative phase shifts (see Figure 6.5a), the sample was regarded as FM stabilized. However, when detached from the substrate, we measured a very broad thermal

[2]Here, another portion of the transferred NPs is measured, compared to Figure 5.7b.

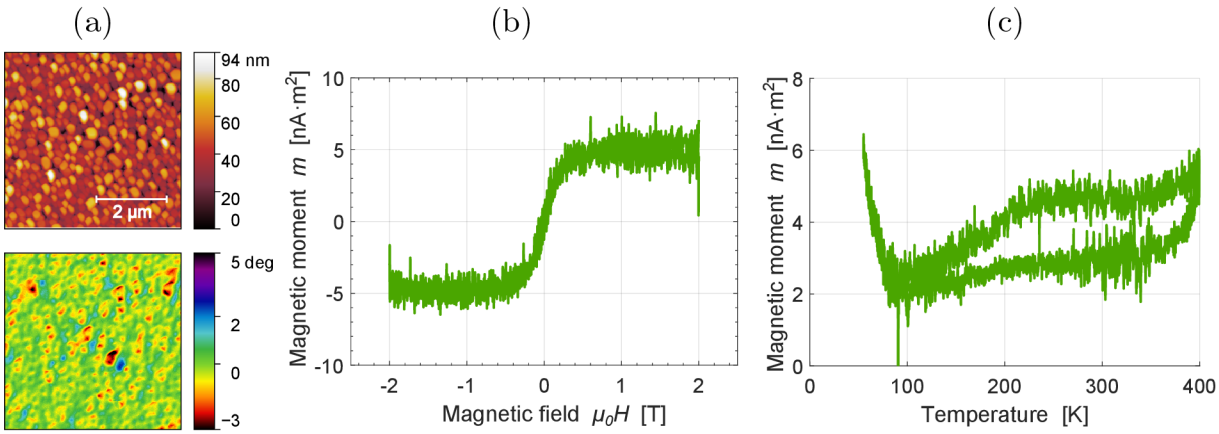

Figure 6.5: Densely packed FeRh islands showing a broad metamagnetic transition: (a) AFM image (top) and corresponding MFM image (bottom) of the sample before etching; (b) field hysteresis for transferred NPs acquired at 400 K; (c) thermal hysteresis for transferred NPs.

hysteresis, as shown in Figure 6.5c. Unfortunately, no VSM data of the sample was acquired before etching, which does not allow for comparison. Here, we offer the following hypotheses:

(i) Before detachment, the sample could possess a little fraction of metamagnetic islands, as it is sometimes seen for samples formed via Volmer–Weber growth (see Figure 3.4f).

(ii) Upon releasing, strongly strained islands could relax and adopt a lattice parameter that allows AF order and thus the phase transition. In fact, a similar observation was made by Ohtani and Hatakeyama [78] for a thick continuous film when peeled from the substrate (see Figure 3.12).

(iii) A defective scanning probe tip may have caused a certain distortion of the AFM and MFM images in Figure 6.5a, such that the islands shown here might be better separated and even show a more rounded shape. In fact a thickness of 12 nm presents a value close to the threshold, where a continuous layer is formed, and thus formation through solid-state dewetting could have been promoted. In such a case, such islands with a reduced size could have remained in a supercooled state at room temperature, resulting in the noticeable amplitude of the MFM signal in Figure 6.5a.

Henceforth, attention will be exclusively focused on samples exhibiting metamagnetism already when supported on a substrate. To transfer such released structures from the etching solution, the magnetic separation needs to be performed at high temperature. This was achieved by heating the solution to temperature of 85 °C prior to the separation.

At first, a partially dewetted FeRh film (see Figure 6.6a), recorded during detachment in real time in Section 4.3, was magnetically separated at high temperature of the solution and both field and thermal hysteresis of the transferred fraction were measured. Here, we compare the magnetometry data for the sample supported on a substrate (see the red curve in Figure 6.6b–d), as well as for the transported fraction of the dewetted film (see the green curve in Figure 6.6b–d).

The magnetic moment of the separated FeRh fraction at 400 K corresponds to around 35% of the magnetic moment at 400 K before the release. This percentage represents the fraction of the transferred material. Notably, the minimum magnetic moment of the transferred material significantly dropped after the film detachment, reaching only $\sim 0.2\, m_0$,

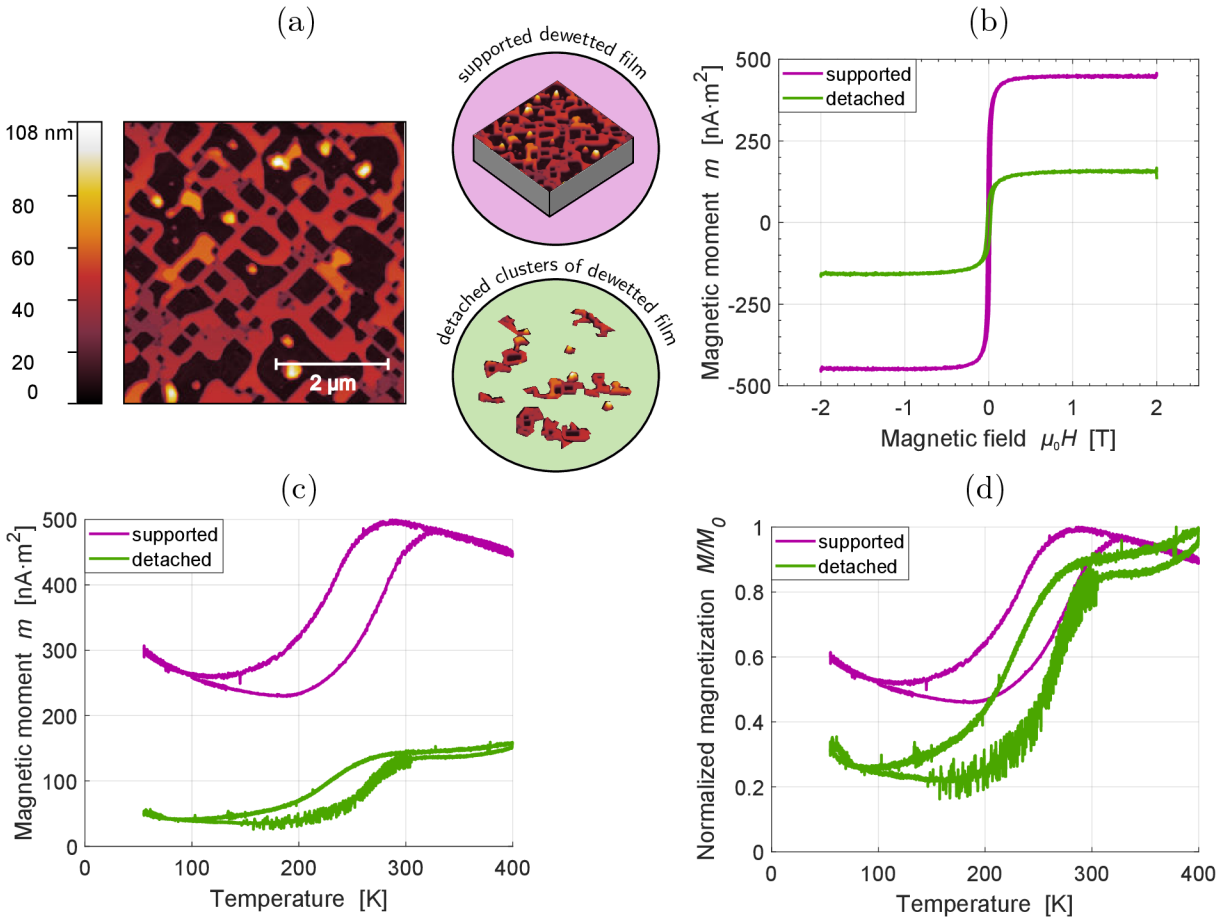

Figure 6.6: A partially dewetted FeRh film showing a large drop in the low-temperature residual magnetization when detached from the substrate: (a) AFM image of the sample before etching; (b) field hysteresis of the dewettted film supported on a substrate and of the transferred fraction acquired at 400 K; (c) thermal hysteresis of the dewettted film supported on a substrate and of the transferred fraction; (d) thermal hysteresis normalized with respect to the maximum magnetization M_0 reached during thermal cycling.

instead of $\sim 0.5\, m_0$, where m_0 is the maximum magnetic moment achieved during cycling in the 55–400 K temperature range (see Figure 6.6d). This is in agreement with the observation made by Ohtani and Hatakeyama [78] in which a relaxed film possesses a lower residual magnetization value in the nominal AF phase.

Finally, well-separated islands (arising from a sample with a nominal thickness of 12 nm, see Figure 6.7a), observed in a liquid environment in Section 6.1, were intended to be magnetically separated. However, only a very little fraction ($\sim 2\%$) was transferred by this means. Instead, a light gray coating remained on the substrate surface even after 5 h in the etching solution at temperature around 65 °C. These remaining NPs had not been clamped anymore to the substrate, but remained only by adhesive forces. These NPs were easily detached by sweeping the substrate surface with a wipe.

The magnetometry data for islands supported on a subtrate before etching as well as for separated NPs are shown in Figure 6.7b–d. The magnetic moment of the transferred NPs at 400 K corresponds to around 73% of the magnetic moment at 400 K before the release, which is related to the transferred fraction of the material. The shape of the thermal hysteresis has not changed significantly after NP detachment (see Figure 6.7c–d). We argue that the NPs were relaxed to a large extent already when supported on the

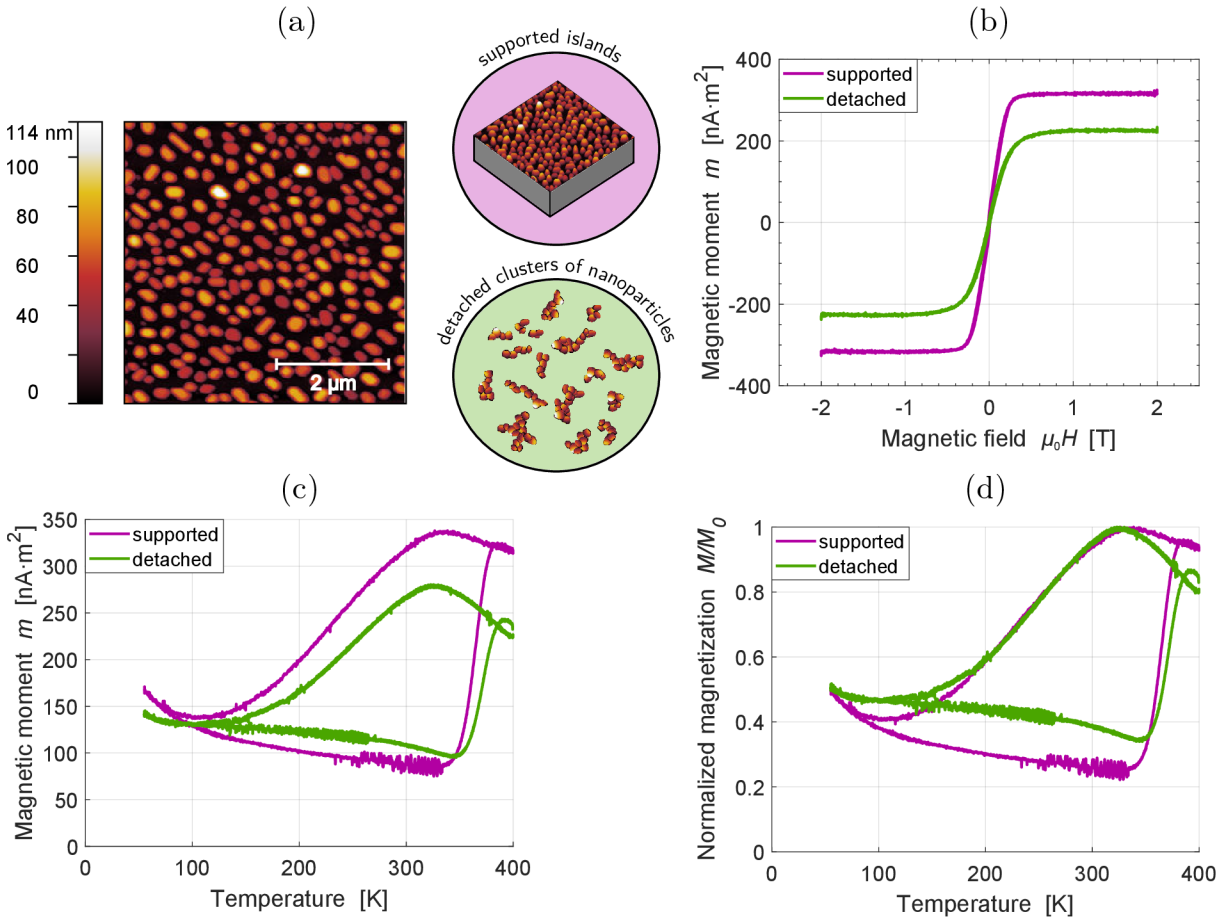

Figure 6.7: Metamagnetic NPs maintaining similar thermal hysteresis shape when removed from the substrate: (a) AFM image of the sample before etching; (b) field hysteresis of the supported islands and of the transferred NP fraction acquired at 400 K; (c) thermal hysteresis of the supported islands and of the transferred NP fraction; (d) thermal hysteresis normalized with respect to the maximum magnetization M_0 reached during thermal cycling.

MgO substrate, as a result of their small size (100–200 nm in diamater) and the associated increased surface-to-volume ratio. Therefore, strain release did not have a significant effect on the residual magnetization of the released islands, at least in comparison with the case of the partially dewetted FeRh film (see Figure 6.6).

6.3 Overview of nanoparticle metamagnetic properties

The magnetic behavior of self-standing FeRh NPs was examined via magnetometry as well as via observation of the clustering dynamics in a liquid environment. It has been reported that:

(i) At the etching temperature of 65 °C, FeRh NPs aggregate into clusters, but the clusters can still detach and change their mutual position and orientation. When warmed up to 80 °C, the observed changes are more dynamical - as a general observation, more clusters appear and tend to agglomerate stronger, evolving to more compact bundles.

(ii) In contrast to FM stabillized FeRh NPs which form bulky clusters, agglomerates in the form of long chains are observed for metamagnetic FeRh samples within the studied temperature range.

(iii) Metamagnetic FeRh NPs form complex systems of clusters on the liquid surface, interconnected through very thin chains. Consequently, the motion of the clusters appears to be synchronized.

(iv) The segregation of metamagnetic FeRh NPs could not be achieved at low temperatures, which would have enabled full control over the aggregation and segregation dynamics of the NPs in solution. A possible explanation might be found in the cohesive forces or in the tendency of sub-micron FeRh objects to be supercooled.

(v) Bigger clusters can be rotated by and moved towards a magnet. This can be done at 80 °C, but also to a certain extent at room temperature.

(vi) Clusters of the partially dewetted film show much lower residual magnetization after detachment from the substrate. On the other hand, the residual magnetization of well-separated nanoislands with a reduced size (> 200 nm) did not evolve dramatically. This can be understood in terms of strain release, which is more significant in the case of the dewetted film, as small sized nanoislands are partially relaxed already when supported on the substrate.

Conclusions

The work presented here shows a route for fabrication of metamagnetic, sub-micron FeRh nanoisland arrays on single-crystal substrates. The morphology and magnetic properties of the FeRh nanomagnets supported on a substrate were thoroughly investigated. In addition, the work examined different strategies for nanoisland release and separation, such that metamagnetic FeRh nanoparticle ensembles were produced and their magnetic behavior as free-standing nano-objects was reported. This new class of metamagnetic nanoparticles presents a promising platform for a vast number of applications, which can potentially profit from the significant changes in magnetization or the extraordinary amount of latent heat released across the phase transition in FeRh. In addition, the phase transition is controllable not only by magnetic fields but via various driving forces (e.g. temperature, hydrostatic pressure, light pulses).

The thesis starts with a brief overview of the relevant applications of nanoparticles and nanostructures, reviewing the current state-of-the-art fabrication strategies. In particular, solid-state dewetting, which constitutes the principal fabrication approach in this work, is presented. This self-assembly route, leading to spontaneous three-dimensional agglomeration of thin films, offers great benefits and consists of a low-cost mass production method. The basic concepts associated with thermodynamic or kinetic growth processes of thin films are also summarized. For example, the Wulff and Winterbottom constructions (which predict the equilibrium shape of self-standing and supported crystallites, respectively) prove to be particularly useful for interpretation of the experimental results in this thesis.

Upon presenting the theoretical background, the feasibility of self-assembly for fabrication of FeRh nano-objects is presented, as well as a number of potential applications are envisioned.

The second part of the thesis reports on the fabrication and characterization of supported FeRh nanoislands on different substrates, ensued by detailed investigation of their morphology and magnetic properties. Initially, it has been shown that the preferential directionality of FeRh solid-state dewetting is strongly predetermined by the specific epitaxial matching with a particular substrate. Having considered various parameters affecting the degree of dewetting, well-separated islands on MgO(001), MgO(011) and Al_2O_3(0001) substrates were successfully fabricated. The morphology of the islands was experimentally investigated in detail and further modelled using thermodynamic surface energy arguments within the Winterbottom construction. We have found an excellent matching between the predicted equilibrium shapes and the experimental topographic features.

Subsequently, the collective magnetic behavior of FeRh nanoisland arrays was examined by means of different experimental techniques and modeling based on predicted surface energy values. We have shown a strong interconnection between morphology and magnetic properties of self-assembled FeRh islands, the latter governed to a large extent by the particular growth mechanism. It was demonstrated that solid state dewetting leads to an advantageous morphology that allows antiferromagnetic ordering and hence the phase transition, opposite to the self-assembly route consisting of the Volmer–Weber growth mode. In addition, the metamagnetic transition of individual FeRh islands was characterized using spatially resolved magnetic imaging. We have observed that FeRh

nanomagnets can display supercooled metastable ferromagnetic ordering even 150 K below the transition temperature, which constitutes an unusually large supercooling in a first-order phase transition material.

The third part of the thesis focuses on releasing FeRh nanomagnets from the substrate in order to investigate them as self-standing nanoparticles. The FeRh nanostructure release was accomplished by etching the underlying MgO substrate in a solution of EDTA disodium salt, which was identified as a suitable etching agent for MgO substrates. The MgO etching and the subsequent separation from the etching solution were principally studied on test structures made of W, Pt, Fe and ferromagnetically stabilized FeRh. Several separation strategies aiming to collect and transfer FeRh nanoparticles to another platform were investigated, with a special emphasis on magnetic separation. It was demonstrated that FeRh nanoparticles can eventually be separated with the use of permanent magnets (providing a field of about 0.5 T at a distance of 1 cm), which accumulate a fraction of the FeRh nanoparticles at the bottom of a vial, such that the excess solution can be removed. However, the transferred nanoparticle fraction could not be fully purified from the EDTA salt residues. The FeRh nanoparticle fraction that could be separated in this way ranged around 5% of the total deposited material on the substrate, but occasionally up to 75% of the material was separated combining etching with mechanical exfoliation.

The behavior of the released nanoparticles in a liquid environment was investigated under variable temperature and applied magnetic field. It was initially observed that ferromagnetically stabilized FeRh nanoparticles form bulky clusters when detached from the substrate. On the other hand, metamagnetic FeRh nanoparticles assembled into complex chain-like systems. When heated up to $\sim 80\,^{\circ}\mathrm{C}$, FeRh clusters tended to acquire more compact arrangements, which could result from the stable ferromagnetic ordering of FeRh at high temperatures.

Furthermore, magnetometry data of separated metamagnetic nanostructures were acquired. We have shown that the residual magnetic moment at low temperatures in the case of a partially dewetted film was considerably lowered when released from the substrate, which could be a consequence of stress relaxation. On the other hand, the magnetometry data acquired for assemblies of FeRh nanoparticles with a characteristic size of 200 nm did not show a significant variation in comparison to the case in which they were supported on the substrate. This may point to the fact that strain relaxation is already realized for islands with such a reduced size, such that releasing them from the substrate does not have a noticeable impact on their residual magnetization.

In order to enable investigation of the FeRh nanoparticle behavior in more detail, one needs to optimize the nanoparticle release and separation. The first limiting factor is the salt crystallization, which occurs when the solution is cooled below the etching temperature. For this purpose, an alternative etchant could be employed. For instance, citric acid, investigated along with EDTA disodium salt in Section 4.1, could be used instead despite a slightly slower etching rate. Additionally, to transfer a large nanoparticle fraction, the separation strategy must be improved. For this purpose, a solution of citric acid could be favorably used as well, as no salt crystals would sediment during centrifugation. Alternatively, we have seen that the majority of nanoparticles can adhere to the substrate even after a long etching process. Instead of transferring the adhering nanoparticles by sweeping the substrate surface with a wipe, one could try to use ultrasound in order to release the nanoparticles directly to the water after pre-etching of the substrate in the acid.

Another issue that needs to be addressed is the nanoparticle agglomeration which occurs even at room temperature due to adhesive forces between nanoparticles, as well as due to the residual magnetization of a certain nanoparticle fraction. This impedes controlling the agglomeration and segregation of FeRh nanoparticles as desired, thus hindering an important mechanism of remote control. This could be resolved by encapsulating the FeRh nanoparticles into a suitable coating. Similarly, the protective coating could prevent undesired effects due to the poor biocompatibility of rhodium compounds in the case of use in biomedical applications.

In summary, this thesis shows a viable way to fabricate both FeRh nanoislands and nanoparticles with characteristic sub-micron sizes, while preserving their metamagnetic properties. We envision that the fabrication of metamagnetic nanoisland systems, as well as the nanoparticle detachment and separation, presented in this thesis, can be developed and adapted to applications from various fields.

References

[1] M. Naito, T. Yokoyama, K. Hosokawa, and K. Nogi, *Nanoparticle Technology Handbook (3rd edition)*, Elsevier Science (2018).

[2] S. Wilhelm *et al.*, "Analysis of nanoparticle delivery to tumours", *Nature Reviews Materials* **1**, 16014 (2016).

[3] O. Bitton, D. B. Gutman, R. Berkovits, and A. Frydman, "Multiple periodicity in a nanoparticle-based single-electron transistor", *Nature Communications* **8**, 402 (2017).

[4] M. Bajus, *Petrochemistry: Petrochemical Processing, Hydrocarbon Technology and Green Engineering*, John Wiley & Sons (2020).

[5] M. Snousy, and M. Zawrah, "Nanoparticles Restrictions in Environmental Cleanup", *Nano Research & Applications* **3**, 1 (2017).

[6] I. Khan, K. Saeed, and I. Khan, "Nanoparticles: Properties, applications and toxicities", *Arabian Journal of Chemistry* **12**, 908 (2017).

[7] E. Petryayeva, and U. J. Krull, "Localized surface plasmon resonance: Nanostructures, bioassays and biosensing—A review", *Analytica Chimica Acta* **706**, 8 (2011).

[8] S. Unser, I. Bruzas, J. He, and L. Sagle, "Localized surface plasmon resonance biosensing: current challenges and approaches", *Sensors* **15**, 15684 (2015).

[9] H. Yu, Y. Peng, Y. Yang, and Z.-Y. Li, "Plasmon-enhanced light–matter interactions and applications", *npj Computational Materials* **5**, 45 (2019).

[10] P. Christian, F. Von der Kammer, M. Baalousha, and T. Hofmann, "Nanoparticles: structure, properties, preparation and behaviour in environmental media", *Ecotoxicology* **17**, 326 (2008).

[11] V. G. Reshma, and P. V. Mohanan, "Quantum dots: Applications and safety consequences", *Journal of Luminescence* **205**, 287 (2019).

[12] V. Sridhara, and L. Satapathy, "Effect of Nanoparticles on Thermal Properties Enhancement in Different Oils – A Review", *Critical Reviews in Solid State and Material Sciences* **40**, 399 (2015).

[13] P. Sivashanmugam, *Application of Nanofluids in Heat Transfer*, In: S. N. Kazi (Eds.), *An Overview of Heat Transfer Phenomena* (pp. 411-440). InTech (2012).

[14] F. Gao, and Z. Gu, *Melting Temperature of Metallic Nanoparticles*, In: M. Aliofkhazraei (Eds.), *Handbook of Nanoparticles* (pp. 661–690). Springer (2016).

[15] K. Lu, "Sintering of nanoceramics", *International Materials Reviews* **53**, 21 (2008).

[16] D. Guo, G. Xie, and J. Luo, "Mechanical properties of nanoparticles: basics and applications", *Journal of Physics D: Applied Physics* **47**, 013001 (2014).

[17] K. Lee *et al.*, "Understanding the Role of Nanoparticles in Nano-oil Lubrication", *Tribology Letters* **35**, 127 (2009).

[18] S. Blundell, *Magnetism in condensed matter*, Oxford University Press (2001).

[19] Q. A. Pankhurst, J. Connolly, S. K. Jones, and J. Dobson, "Applications of magnetic nanoparticles in biomedicine", *Journal of Physics D: Applied Physics* **36**, 167 (2003).

[20] B. Jiang *et al.*, "Advances of magnetic nanoparticles in environmental application: environmental remediation and (bio)sensors as case studies", *Environmental Science and Pollution Research* **25**, 30863 (2018).

[21] U. Wiedwald, and P. Ziemann, "Preparation, properties and applications of magnetic nanoparticles", *Beilstein Journal of Nanotechnology* **1**, 21 (2010).

[22] Y. Kubota *et al.*,"Heat-Assisted Magnetic Recording's Extensibility to High Linear and Areal Density", *IEEE Transactions on Magnetics* **54**, 1 (2018).

[23] D. Weller *et al.*,"Review Article: FePt heat assisted magnetic recording media", *Journal of Vacuum Science & Technology B* **34**, 060801 (2016).

[24] P. Iqbal, J. A. Preece, and P. M. Mendes, *Nanotechnology: The "Top-Down" and "Bottom-Up" Approaches*, In: P. A. Gale, and J. W. Steed (Eds.), *Supramolecular Chemistry: From Molecules to Nanomaterials* (pp. 3589-3602). John Wiley & Sons Ltd (2012).

[25] L. Critchley, *Nanoparticle Manufacture - What Methods Are There?* AZoNano (2019). Available online at: `https://www.azonano.com/article.aspx?ArticleID=5122`.

[26] S. T. Picraux, *Nanotechnology*, Encyclopædia Britannica (2018). Available online at: `https://www.britannica.com/technology/nanotechnology`.

[27] B. Bahreyni, *Microfabrication*, In: *Fabrication and Design of Resonant Microdevices* (pp. 9-46). John Wiley & William Andrew (2008).

[28] Y. Hayashi, M. Inoue, H. Takizawa, and K. Suganuma, *Nanoparticle Fabrication*, In: J. Morris (Eds.), *Nanopackaging: Nanotechnologies and Electronics Packaging (2nd edition)* (pp. 219-242). Springer (2018).

[29] Z. Cai, Q. Yao, X. Chen, and X. Wang, *Nanomaterials With Different Dimensions for Electrocatalysis*, In: X. Wang, and X. Chen (Eds.), *Novel Nanomaterials for Biomedical, Environmental and Energy Applications* (pp. 435–464). Elsevier (2019).

[30] B. P. Isaacoff, and K. A. Brown, "Progress in Top-Down Control of Bottom-Up Assembly", *Nano Letters* **17**, 6508 (2017).

[31] C. V. Thompson, "Solid-State Dewetting of Thin Films", *Annual Review of Materials Research* **42**, 399 (2012).

[32] E. Jiran, and C. V. Thomson, "Capillary Instabilities in Thin Films", *Journal of Electronic Materials* **19**, 1153 (1990).

[33] G. Barrera *et al.*, "Formation of free-standing magnetic particles by solid-state dewetting of $Fe_{80}Pd_{20}$ thin films", *Journal of Alloys and Compounds* **742**, 751 (2018).

[34] F. Leroy *et al.*, "How to control solid state dewetting: A short review", *Surface Science Reports* **71**, 391 (2016).

[35] F. Cheynis, F. Leroy, and P. Müller, "Dynamics and instability of solid-state dewetting", *Comptes Rendus Physique* **14**, 578 (2013).

[36] D. Kim, A. L. Giermann, and C. V. Thompson, "Solid-state dewetting of patterned thin films", *Applied Physics Letters* **95**, 251903 (2009).

[37] T. Das Gupta *et al.*, "Self-assembly of nanostructured glass metasurfaces via templated fluid instabilities", *Nature Nanotechnology* **14**, 320 (2019).

[38] A. L. Giermann, and C. V. Thompson, "Solid-state dewetting for ordered arrays of crystallographically oriented metal particles", *Applied Physics Letters* **86**, 121903 (2005).

[39] A. Le Bris, F. Maloum, J. Teisseire, and F. Sorin, "Self-organized ordered silver nanoparticle arrays obtained by solid state dewetting", *Applied Physics Letters* **105**, 203102 (2014).

[40] J. Ye, and C. V. Thompson, "Templated Solid-State Dewetting to Controllably Produce Complex Patterns", *Advanced Materials* **23**, 1567 (2011).

[41] M. Naffouti *et al.*, "Templated Solid-State Dewetting of Thin Silicon Films", *Small* **12**, 6115 (2016).

[42] M. Naffouti *et al.*, "Complex dewetting scenarios of ultrathin silicon films for large-scale nanoarchitectures", *Science Advances* **3**, 1472 (2017).

[43] M. Abbarchi *et al.*, "Wafer Scale Formation of Monocrystalline Silicon-Based Mie Resonators via Silicon-on-Insulator Dewetting", *ACS Nano* **8**, 11181 (2014).

[44] A. Herz *et al.*, "Solid-state dewetting of Au–Ni bi-layer films mediated through individual layer thickness and stacking sequence", *Applied Surface Science* **444**, 505 (2018).

[45] R. Esterina, X. M. Liu, A. O. Adeyeye, C. A. Ross, and W. K. Choi, "Solid-state dewetting of magnetic binary multilayer thin films", *Journal of Applied Physics* **118**, 144902 (2015).

[46] O. Fruchart, M. Klaua, J. Barthel, and J. Kirschner,"Self-organized growth of nano-sized vertical magnetic Co pillars on Au(111)", *Physical Review Letters* **83**, 2769 (1999).

[47] O. Fruchart *et al.*,"Growth modes of Fe(110) revisited: a contribution of self-assembly to magnetic materials", *Journal of Physics: Condensed Matter* **19**, 053001 (2007).

[48] K. Oura , V. G. Lifshits, A. Saranin, A. V. Zotov, and M. Katayama, *Surface Science: An Introduction*, Springer (2003).

[49] WulffPack, *WulffPack – a package for Wulff constructions*. Available online at: `https://wulffpack.materialsmodeling.org`.

[50] J. M. Rahm, and P. Erhart,"WulffPack: A Python package for Wulff constructions", *Journal of Open Source Software* **5**, 1944 (2020). See also link to the software: `https://wulffpack.materialsmodeling.org`.

[51] S. Maat, J.-U. Thiele, and E. E. Fullerton, "Temperature and field hysteresis of the antiferromagnetic-to-ferromagnetic phase transition in epitaxial FeRh films", *Physical Review B* **72**, 214432 (2005).

[52] L. H. Lewis, C. H. Marrows, and S. Langridge, "Coupled magnetic, structural, and electronic phase transitions in FeRh", *Journal of Physics D: Applied Physics* **49**, 323002 (2016).

[53] J. A. Arregi *et al.*, "Magnetization reversal and confinement effects across the metamagnetic phase transition in mesoscale FeRh structures", *Journal of Physics D: Applied Physics* **51**, 105001 (2018).

[54] X. Marti *et al.*, "Room-temperature antiferromagnetic memory resistor", *Nature Materials* **13**, 367 (2014).

[55] J.-U. Thiele, S. Maat, and E. E. Fullerton, "FeRh/FePt exchange spring films for thermally assisted magnetic recording media", *Applied Physics Letters* **82**, 2859 (2003).

[56] M. P. Annaorazov *et al.*, "Alloys of the Fe–Rh system as a new class of working material for magnetic refrigerators", *Cryogenics* **32**, 867 (1992).

[57] V. Uhlíř, J. A. Arregi, and E. E. Fullerton, "Colossal magnetic phase transition asymmetry in mesoscale FeRh stripes", *Nature Communications* **7**, 13113 (2016).

[58] M. Loving *et al.*, "Structural evidence for stabilized ferromagnetism in epitaxial FeRh nanoislands", *Journal of Physics D: Applied Physics* **46**, 162002 (2013).

[59] M. Liu *et al.*, "Magnetism and morphology in faceted B2-ordered FeRh nanoparticles", *EPL* **116**, 27006 (2016).

[60] G. C. Han *et al.*, "Magnetic stability of ultrathin FeRh films", *Journal of Applied Physics* **113**, 17C107 (2013).

[61] J. P. Ayoub, C. Gatel, C. Roucau, and M.-J. Casanove, "Structure and chemical order in FeRh nanolayers epitaxially grown on MgO(001)", *Journal of Crystal Growth* **314**, 336 (2011).

[62] C. W. Barton *et al.*, "Substrate Induced Strain Field in FeRh Epilayers Grown on Single Crystal MgO (001) Substrates", *Scientific Reports* **7**, 44397 (2017).

[63] L. Motyčková, *Epitaxial growth and characterization of metamagnetic nanoparticles for biomedical applications*, Bachelor's thesis, Brno University of Technology (2018). Supervised by J. A. Arregi. Available at: `https://www.vutbr.cz/studenti/zav-prace?zp_id=109718`.

[64] I. V. Markov, *Crystal Growth For Beginners: Fundamentals of Nucleation, Crystal Growth and Epitaxy (2nd edition)*, Word Scientific (2003).

[65] D. Nečas, and P. Klapetek,"Gwyddion: an open-source software for SPM data analysis", *Central European Journal of Physics* **10**, 181 (2012).

[66] J. A. Arregi, O. Caha, and V. Uhlíř,"Evolution of strain across the magnetostructural phase transition in epitaxial FeRh films on different substrates", *Physical Review B* **101**, 174413 (2020).

[67] G. Seguini *et al.*, "Solid-state dewetting of ultra-thin Au films on SiO_2 and HfO_2", *Nanotechnology* **25**, 495603 (2014).

[68] E. E. Fullerton, M. J. Conover, J. E. Mattson, C. H. Sowers, and S. D. Bader, "Oscillatory interlayer coupling and giant magnetoresistance in epitaxial Fe/Cr(211) and (100) superlattices", *Physical Review B* **48**, 15755 (1993).

[69] M. Ohtake, F. Kirino, and M. Futamoto, "Structure and magnetic Properties of Fe/X (X=Au, Ag, Cu) epitaxial multilayer films grown on MgO(011) substrates", *Japanese Journal of Applied Physics* **46**, L895 (2007).

[70] L. Vitos, A. V. Ruban, H. L. Skriver, and J. Kollár, "The surface energy of metals", *Surface Science* **411**, 186 (1998).

[71] C. Bordel *et al.*, "Fe Spin Reorientation across the Metamagnetic Transition in Strained FeRh Thin Films", *Physical Review Letters* **109**, 117201 (2012).

[72] S. Foner, "Versatile and Sensitive Vibrating-Sample Magnetometer", *Review of Scientific Instruments* **30**, 548 (1959).

[73] Quantum Design, *VersaLab*. Available online at: `https://www.qdusa.com/products/versalab.html`.

[74] H. Kumar *et al.*, "Strain effects on the magnetic order of epitaxial FeRh thin films", *Journal of Applied Physics* **124**, 085306 (2018).

[75] P. Dróżdż *et al.*, "Perpendicular magnetic anisotropy and residual magnetic phases in gold-capped FeRh film on MgO(0 0 1)", *Journal of Magnetism and Magnetic Materials* **495**, 165804 (2020).

[76] G. Zheng *et al.*, "Epitaxial strain controlled magnetocrystalline anisotropy in ultrathin FeRh/MgO bilayers", *AIP Advances* **7**, 055914 (2017).

[77] R. Fan *et al.*,"Ferromagnetism at the interfaces of antiferromagnetic FeRh epilayers", *Physical Review B* **82**, 184418 (2010).

[78] Y. Ohtani, and I. Hatakeyama,"Features of broad magnetic transition in FeRh thin film", *Journal of Magnetism and Magnetic Materials* **131**, 339 (1994).

[79] C. Goy *et al.*,"Shrinking of rapidly evaporating water microdroplets reveals their extreme supercooling", *Physical Review Letters* **120**, 015501 (2018).

[80] T. Edler, and S. G. Mayr, "Film Lift–Off from MgO: Freestanding Single Crystalline Fe–Pd Films Suitable for Magnetic Shape Memory Actuation – and Beyond", *Advanced Materials* **22**, 4969 (2010).

[81] S. J. S. Flora, and V. Pachauri, "Chelation in metal intoxication", *International journal of environmental research and public health* **7**, 2745 (2010).

[82] A. Lopata *et al.*, "Chelation: EDTA Tightly Binds Taq DNA Polymerase, MutT and dUTPase and Directly Inhibits dNTPase Activity", *Biomolecules* **9**, 621 (2019).

[83] F. Demir, O. Laçin, and B. Dönmez, "Leaching Kinetics of Calcined Magnesite in Citric Acid Solutions", *Journal of Industrial and Engineering Chemistry* **15**, 865 (2009).

[84] J. Liebscher,"Chemistry of polydopamine – scope, variation, and limitation", *European Journal of Organic Chemistry* **2019**, 4976 (2019).

[85] H. Lee, S. M. Dellatore, W. M. Miller, and P. B. Messersmith,"Mussel-inspired surface chemistry for multifunctional coatings", *Science* **318**, 426 (2007).

[86] Malvern Panalytical, *Particle concentration measurements on the Zetasizer Ultra – How it works*. Available online at: `https://www.malvernpanalytical.com/en/learn/knowledge-center/technical-notes/TN180720ParticleConcZetasizerHowTo`.

[87] J. Stetefeld, S. A. McKenna, and T. R. Patel, "Dynamic light scattering: a practical guide and applications in biomedical sciences", *Biophysical reviews* **8**, 409 (2016).

List of abbreviations

2D	two dimensions or two-dimensional
3D	three dimensions or three-dimensional
AF	antiferromagnetic
AFM	atomic force microscopy
CMOS	complementary metal–oxide–semiconductor
DLS	dynamic light scattering
DRIE	deep reactive ion etching
EBL	electron beam lithography
EDTA	ethylenediaminetetraacetic acid
EDX	energy-dispersive x-ray spectroscopy
EPR	enhanced permeability and retention
FM	ferromagnetic
LED	light-emitting device
LSPR	localized surface plasma resonance
MFM	magnetic force microscopy
MNPs	magnetic nanoparticles
MOKE	magneto-optical Kerr effect
MRI	magnetic resonance imaging
NIL	nanoimprint lithography
NPs	nanoparticles
PDA	polydopamine
PID	proportional–integral–derivative
PVD	physical vapor deposition
QDs	quantum dots
RIE	reactive ion etching
SEM	scanning electron microscopy

SOI	silicon on insulator
SPM	superparamagnetic
VSM	vibrating sample magnetometry
XRD	x-ray diffraction

A Nanoisland size analysis

To examine the size uniformity of island arrays, island size distribution histograms were computed from the AFM images acquired for samples with well-separated islands. In particular, samples M(001)-16b and M(001)-12a show regular-sized, round-shaped and well-spaced islands (see Figure A.1a,c). Samples with interconnected or closely spaced islands were discarded for this analysis.

The size distributions were obtained using the grain analysis tools provided by the program *Gwyddion 2.50*. The islands were separated from the background based on a topographic height threshold value, chosen as 15% of the maximum height in the corresponding AFM image. It was found that this value is a good compromise to discriminate the actual islands from roughness of defect-like features. The equivalent disc diameters of individual islands were determined from the effective island area and plotted in the form of histograms in Figure A.1b,d. Additionaly, the size distribution was fitted by a Gaussian function to determine the mean island size of the particular sample.

It is clearly seen that for well-separated islands formed via solid-state dewetting, a reduction of the nominal FeRh thickness leads to smaller average island diameter.

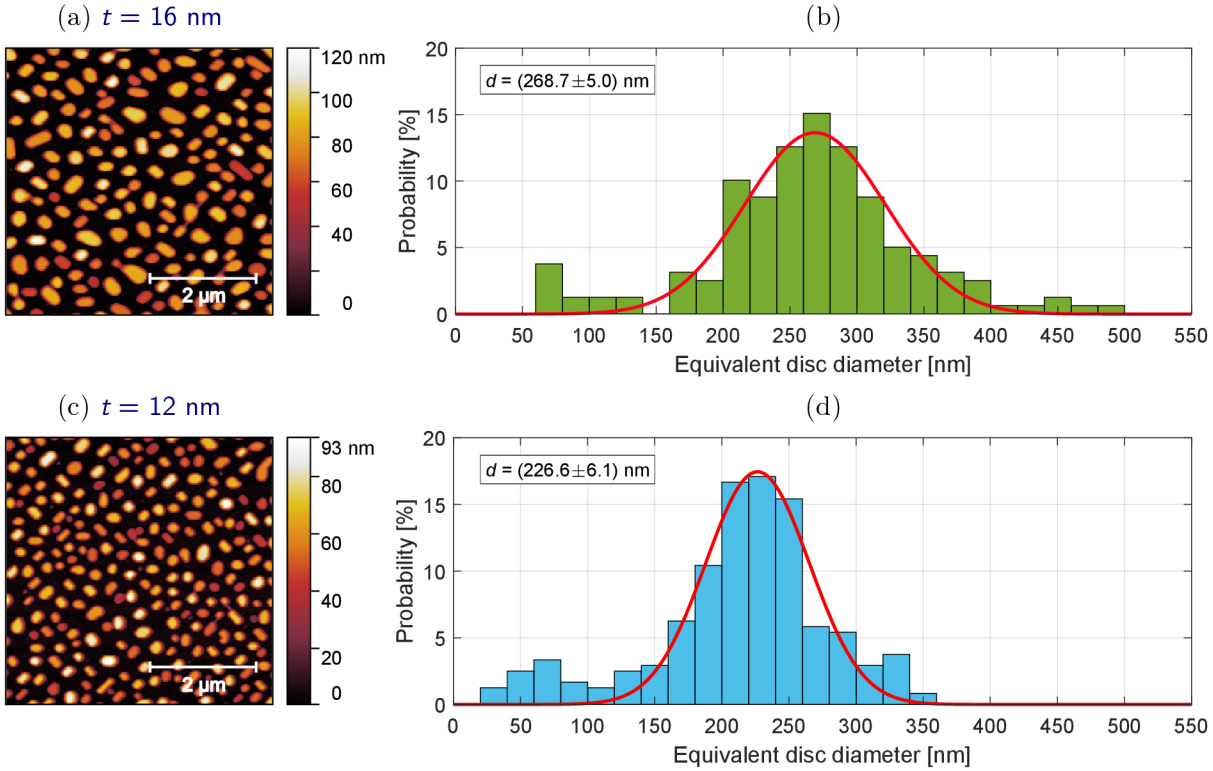

Figure A.1: Size distribution analysis for FeRh islands on MgO(001) substrates. AFM image (left panel) and an island size distribution histogram (right panel) for (a)–(b) sample M(001)-16b with a nominal thickness of 16 nm; (c)–(d) sample M(001)-12a with a nominal thickness of 12 nm. The red solid lines in (b) and (d) indicate the Gaussian fit of the size distribution. The fitted average island diameter d (Gaussian center) is indicated in the top left inset.

B Size distribution and concentration of dispersed Pt nanoparticles

In order to confirm the presence of dispersed Pt NPs in solution (which would resemble the behavior of AF FeRh NPs) by a quantitative approach„ we employed the dynamic light scattering (DLS) technique [87]. This method is based on the Brownian motion of dispersed particles and enables estimating the particle size and concentration. As the impact of random collisions on the movement differ for small and large particles, the hydrodynamic diameter of dispersed particles can be determined from the particle speed. During the measurement, a single frequency laser is directed to the solution with particles contained in a cuvette (see Figure B.1). The laser light is scattered in all directions and detected at a fixed angle over time. The recorded scattered intensity is used to generate a correlation function, describing how long particles remain at the same spot within the sample. The time-dependent exponential decay of the correlation function can be fitted in order to estimate the translational diffusion coefficient D associated with the particle speed. Finally, the size of a particle is calculated as the hydrodynamic diameter d_{H} from the diffusion coefficient D via the Stokes-Einstein equation

$$d_{\mathrm{H}} = \frac{k_{\mathrm{B}}T}{3\pi\eta D}, \tag{B.1}$$

where k_{B} is the Boltzmann constant, T is the temperature and η is the viscosity of the dispersing medium. Provided that the absorptive part of the refractive index is known for the sample under consideration, the intensity-based size distribution can be recalculated to a volume- or number-based size distribution.

DLS experiments on the Pt NPs dispersed in the EDTA disodium salt solution was done using a *Zetasizer Ultra* instrument from Malvern corporation, with the help of T. Sojková. Prior to the measurements, the NP suspension was sonicated to break up poten-

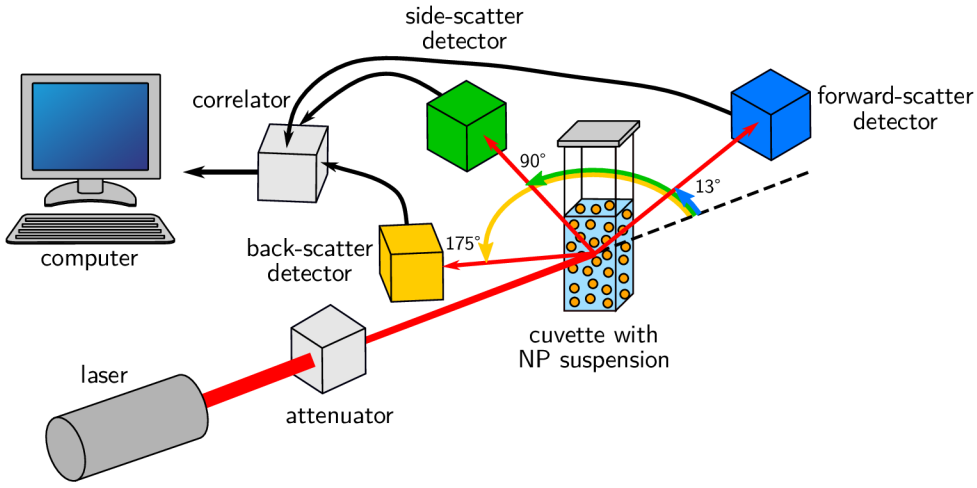

Figure B.1: Schematic of a DLS experiment. The intensity of the laser source is optimized in the attenuator and the laser beam is directed towards the cuvette with NP suspension. The scattering intensity signal retrieved at three different detectors is processed by a correlator and acquired in the computer.

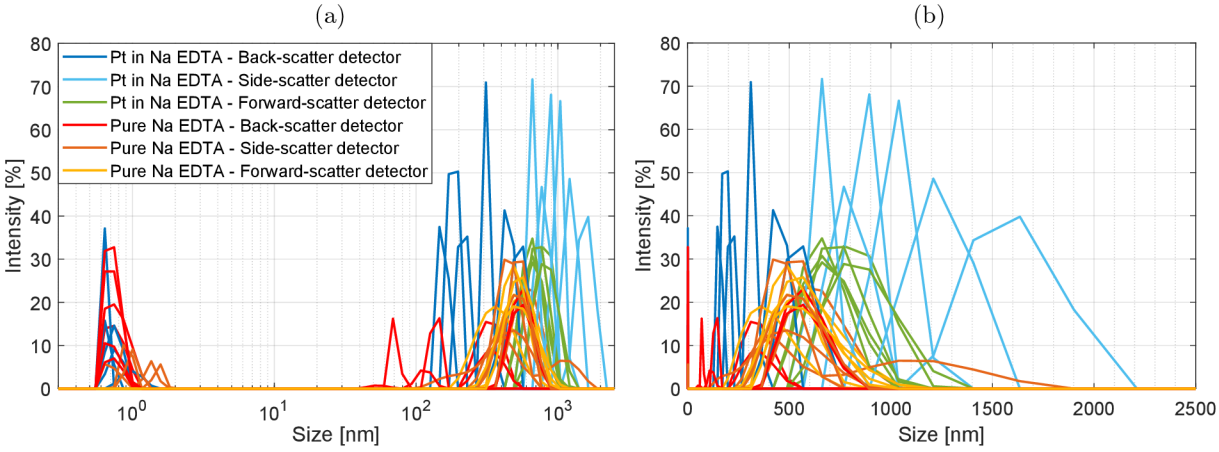

Figure B.2: Intensity-weighted particle size distribution for the Pt NP suspension and the bare EDTA disodium salt reference: (a) on a logarithmic scale; (b) on a linear scale.

tial agglomerates. For the analysis, the tabulated refractive index of Pt was used, while the liquid solution was treated as water.

The scattered intensity at room temperature was detected at 13 °, 90 ° and 175 ° relative to the incident laser beam, using a forward-scatter, side-scatter and back-scatter detector, respectively (see Figure B.1). An additional measurement for a cuvette containing a pure solution of ultrasonicated EDTA disodium salt was acquired as a reference.

The measurement results in the form of intensity-based size distribution provided by the DLS analysis system are shown in Figure B.2. We observe two groups of peaks, appearing around particle sizes of 10^0 nm and 10^2–10^3 nm (see Figure B.2a). We ascribe the peaks around 10^0 nm, which are more pronounced for the pure EDTA disodium salt, to the salt molecules. The peaks around 10^2–10^3 nm are better distinguishable on a linear scale (see Figure B.2b). For the reference sample of pure EDTA disodium salt, we see more unified size distributions from all three detectors showing intensity peaks around 500 nm. On the contrary, the Pt NPs suspension reveals peaks over wider range, grouped according to the used detector. Based on the appearance of peaks around 10^2–10^3 nm also for the reference sample, we conclude that both samples contain salt clusters with sizes in this range.

However, the higher scattered intensity as well as the wider size range of the intensity peaks for the Pt NP suspension in comparison to the reference sample evidence that salt clusters cannot be the only objects of 10^2–10^3 nm in size responsible for the scattered light signals seen for the Pt NP specimen. Instead, we argue that the additional signal arises from scattering by the Pt NPs. Considering the AFM image of well-separated Pt islands before etching (see Figure 4.6a), the detached NPs should posses arbitrary shapes of various sizes, which could explain the broad size range of peaks in Figure B.2b. Besides, our Pt NPs are not spherical, but can be regarded as ellipsoidal shaped bodies with a shorter axis or around ~ 100 nm and perpendicular axes ranging between 500 nm and 2 µm. Hence the perceived particle size in the experiment depends on the relative orientation of Pt NPs with respect to light scattering, as evidenced by the slightly different results obtained by different detectors (see Figure B.2b).

In addition, we aimed to determine the concentration of Pt NPs which can be achieved by recording the time averaged photon count rate scattered by the sample [86]. Specifically, the intensity-weighted particle size distribution is converted using the Mie theory

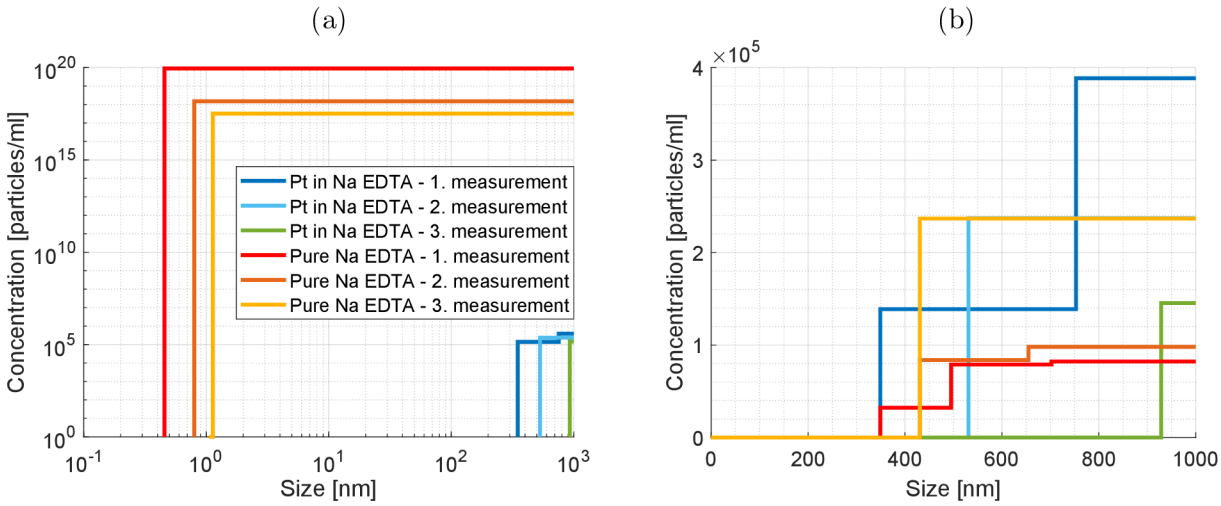

Figure B.3: Cumulative concentration-based size distribution of the Pt NP suspension and the reference solution: (a) using logarithmic scales on both axes; (b) removing the concentration data around 10^0 nm in size and using linear scales on both axes.

into an absolute concentration distribution based on the derived count rate and the input complex refractive index. Accordingly, the absolute concentration-based size distribution was measured for the Pt NP suspension and the reference sample. Three measurements for each sample are shown in the form of cumulative distributions in Figure B.3. Using logarithmic scales on both axis reveals a very high concentration (up to 10^{20} particles/ml) of salt molecules with 10^0 nm size for the reference sample (see Figure B.3a). This is not observed for the Pt NP suspension as the Pt particles scatter the light intensity considerably more. Instead, we measure only the concentration corresponding to particles of 10^2–10^3 nm in size. In order to better visualize the concentration results corresponding to sizes 10^2–10^3 nm, we removed contribution of small particles from the dataset of the reference sample. The cumulative concentration-based size distribution upon this correction is plotted in linear scale in Figure B.3b. We see that the reference sample posseses generally lower concentration of objects of 10^2–10^3 nm in size, assumed to salt clusters, when compared to the PT NPs suspension, containing both salt and Pt NPs. Despite these observations suggesting the existence of a finite concentration of Pt NPs, an accurate concentration value could not be determined due to a number of reasons. For example, DLS measurements assume that NPs are spherical and scatter light isotropically, which is not valid for our Pt NPs. Additionally, our samples succumb to salt crystallization over time due to the lower solubility of EDTA disodium salt at room temperature.

In summary, the DLS technique gives evidence for the presence of Pt NPs in the etching solution. However, the absolute concentration value could not be precisely determined via this method.